MECHANISMS FOR STABILITY, DEGRADATION, AND REGENERATION OF NI (OXY)HYDROXIDE FOR OXYGEN EVOLUTION ELECTROCATALYSIS AND PHOTOCATALYSIS

by

JESSICA L. FEHRS

A DISSERTATION

Presented to the Department of Chemistry and Biochemistry
and the Division of Graduate Studies of the University of Oregon
in partial fulfillment of the requirements
for the degree of
Doctor of Philosophy

June 2021

DISSERTATION APPROVAL PAGE

Student: Jessica L. Fehrs

Title: Mechanisms for Stability, Degradation, and Regeneration of Ni(Oxy)Hydroxide for Oxygen Evolution Electrocatalysis and Photocatalysis

This dissertation has been accepted and approved in partial fulfillment of the requirements for the Doctor of Philosophy degree in the Department of Chemistry and Biochemistry by:

Ramesh Jasti	Chairperson
Shannon Boettcher	Advisor
Cathy Wong	Core Member
Benjamín Aleman	Institutional Representative

and

Andrew Karduna	Interim Vice Provost for Graduate Studies

Original approval signatures are on file with the University of Oregon Division of Graduate Studies.

Degree awarded June 2021

© 2021 Jessica L. Fehrs

DISSERTATION ABSTRACT

Jessica L. Fehrs

Doctor of Philosophy

Department of Chemistry and Biochemistry

June 2021

Title: Mechanisms for Stability, Degradation, and Regeneration of Ni(Oxy)Hydroxide for Oxygen Evolution Electrocatalysis and Photocatalysis

There is a global annual increase in energy consumption and a corresponding global increase in harmful carbon emissions and greenhouse gases into Earth's atmosphere. Anthropogenic greenhouse gases in our atmosphere are the major contributor to global warming, where CO_2 emissions from the use of fossil fuels is the primary factor. Chapter I of this dissertation reviews these statistics in the context of energy consumption by the U.S. and globally, with an emphasis on commercial sectors with the greatest impact on these statistics. Chapter I introduces photoelectrochemical cells (PEC) for water splitting as a promising possibility for alternative renewable energy. Chapter II introduces the material Ni (oxy)hydroxide (NiO_xH_y), a widely used and studied electrocatalysts for water electrolysis, namely the oxygen evolution reaction (OER) half-reaction. The physical, structural, and electrochemical properties of the material are reviewed.

Chapter III presents a new analysis on the structure-stability relationship of Ni (oxy)hydroxide during and after prolonged OER catalysis. Chapter IV evaluates the NiO_xH_y material with Fe-incorporation; $Ni(Fe)O_xH_y$ is one of the most active known catalyst for OER. The role of dynamic Fe incorporation/exclusion during operation and the potential role it plays in the high activity and stability of $Ni(Fe)O_xH_y$ is investigated.

Chapter V of this work presents an electrode-level-approach to using $Ni(Fe)O_xH_y$ for PEC applications. In this chapter a full fabrication scheme is presented for photoanodes utilizing Ni(Fe) (oxy)hydroxide as a catalyst. This work builds on the fundamental studies of the catalyst stability and broadens the scope to full photoanode stability for OER catalysis.

This dissertation contains entirely unpublished work at the time of authorship. Manuscripts for publication based on the material herein are in preparation.

CURRICULUM VITAE

NAME OF AUTHOR: Jessica L. Fehrs

GRADUATE AND UNDERGRADUATE SCHOOLS ATTENDED:

University of Oregon, Eugene
California State Polytechnic University, Pomona
Santa Monica Community College, Santa Monica

DEGREES AWARDED:

Doctor of Philosophy, Physical Chemistry, 2021, University of Oregon
Bachelor of Science, Chemistry, 2016, California State Polytechnic University

AREAS OF SPECIAL INTEREST:

Materials Chemistry
Electrochemistry
Catalysis
Interfacial Semiconductor Physics

PROFESSIONAL EXPERIENCE:

Research Assistant, Boettcher Laboratory, University of Oregon, 2018-2021

Teaching Assistant, University of Oregon, 2016-2021
Introductory Chemistry Lecture, General Chemistry Lecture, General Chemistry Lab, Physical Chemistry Lab, Organic Chemistry Lecture

Year-Round Academic Researcher, Student Independent Research Intern,

NASA's Jet Propulsion Laboratory, Planetary Chemistry/Astrobiology Group, 2014-2016

Research and Discovery Paralegal, Various California Law Firms, 2006-2011

LEADERSHIP EXPERIENCE:

Program Director, Mad Duck Science Friday, University of Oregon, 2019-2019

Director of Curriculum, Coding for Treasure, San Marino, California, 2016

GRANTS, AWARDS, AND HONORS:

Outstanding Research Presentation Award, SUNCAT Stanford, 2019

Excellence in Teaching of Chemistry Award, University of Oregon, 2017

Boeing Chemistry Scholarship Award, California State Polytechnic University, 2015

Valspar Chemistry Student Development Award, California State Polytechnic University, 2015

Cal Poly President's Special Research Travel Grant, California State Polytechnic University, 2014

PUBLICATIONS:

Forrest A. L. Laskowski, Sebastian Z. Oener, Michael R. Nellist, Adrian M. Gordon, David C. Bain, Jessica L. Fehrs & Shannon W. Boettcher. Nanoscale semiconductor/catalyst interfaces in photoelectrochemistry *Nature Materials*, 19, 69-76.

ACKNOWLEDGMENTS

This work was funded in part by the Department of Energy Basic Energy Sciences (DE-SC0014279) and by the National Science Foundation through the GOALI Grant (CHE-1566348). This work was also funded in part by the University of Oregon in providing me teaching positions throughout the years.

I would like to thank my advisor Prof. Shannon Boettcher for your scientific guidance throughout my research journey. Your high standards and thoughtful manner in which you assess scientific work has helped train me to be a better scientist. Also, I want to extend my deepest thanks to my committee members, Dr. Ramesh Jasti, Dr. Cathy Wong, and Dr. Benjamín Aleman. Your participation in our numerous reviews and update meetings were invaluable to my progress towards completing this work. I thank you for helping me have the perspective and focus to document all I have learned and accomplished in these years.

I want to thank all the Boettcher lab members, both current and graduated members I had the opportunity to learn with and learn from. You were my support system, my social relief, my sounding board, and a wonderful source of learning. In particular, I want to thank Raina Krivina. There are no words to describe how much I feel I could not have made this journey without you. When I was at a breaking point, you were the one who helped me know I belong here. I also want to thank Dr. Forrest Laskowski for many deep talks about interfacial physics, and for your perpetual state of optimism, calm energy, and encouragement. A special thank you to Dr. Sebastian Oener who provided me extensive hands-on training on nearly all of the techniques I used in this dissertation. Sebastian was patient and always available. I want to also thank my group mates Tawney Knecht and

Grace Lindquist for years of friendship, support, and enduring positivity. Your kindness and understanding has been invaluable to me.

I would like to thank my partner Chase. Words can't express how much his love and support have helped me. Not only has he support me emotionally when life felt overwhelming, he has supported me physically through the roller coaster that was my health. I could not have wished for a better partner to help me through such a challenging time in my life. I also want to appreciate the support and friendship from my dearest sisters, Vanessa and Alicia Moon. You have been my cheerleaders and my biggest fans for years, always making me feel like I can do anything. I want to include my newest sisters in this appreciation, my Oregon pepperoni gals, Erin, Chelsee, and Stephani. Thank you so much for the laughs, the cries, the endless support, and karaoke.

My family also deserves my deepest appreciation. Thank you to my wonderful parents who always made me feel special and smart. And thank you for always being in my corner. I've never been good at asking for help, but I always knew I could, and when I did you were always there to love and support me. To my sister and brother, Lisa and John, thanks for always making me feel like you care, and that I'm a smarty pants, even if I didn't feel like it. And of course, to my brother Jason, who I owe so much of my personality and love of all things science and computers.

For my brother, Jason.

I know you would be so proud of what I have achieved. My love of technology and science I owe to you. I miss you every day.

And, for the beauty and wonder of the scientific mind.

"At times when the wind has been rather strong, I have frequently watched the gulls who were flying over the waves looking for food, and have often seen them move slowly against the wind or remained stationary facing it, balancing themselves on their wings but without flapping them, this has lasted for 1, 2, 3 or more minutes, and I think could not be due to any previously acquired momentum because they would suddenly sweep round, going down with the wind, and then again return against it, all without flapping the wings; I have also remarked hawks over land advance in a similar manner in similar circumstances, without having been able to detect any motion of the wing calculated to support them. They seem to remain suspended in the air, by an apparent balancing of the body on the wings against the wind. How do these birds fly? And why may not a man or a machine fly in the same way in the same circumstances?"
-Michael Faraday [1]

TABLE OF CONTENTS

Chapter Page

Chapter Page

LIST OF FIGURES

Figure Page

LIST OF TABLES

CHAPTER I

INTRODUCTION

The continual progression of global human lifestyle standards has led to a consistent growth in global energy consumption; in 2019 the annual global primary energy consumption rose 1.3%.[2] In the past ten years the average growth rate for total energy consumption is 1.8% (Figure 1.1a). While it is important to recognize that this increase is less than the average for this past decade, it does still mark the continual increase in demand (Figure 1.1b). Correspondingly, harmful carbon emissions and greenhouse gases in our atmosphere have been on a continual increase.

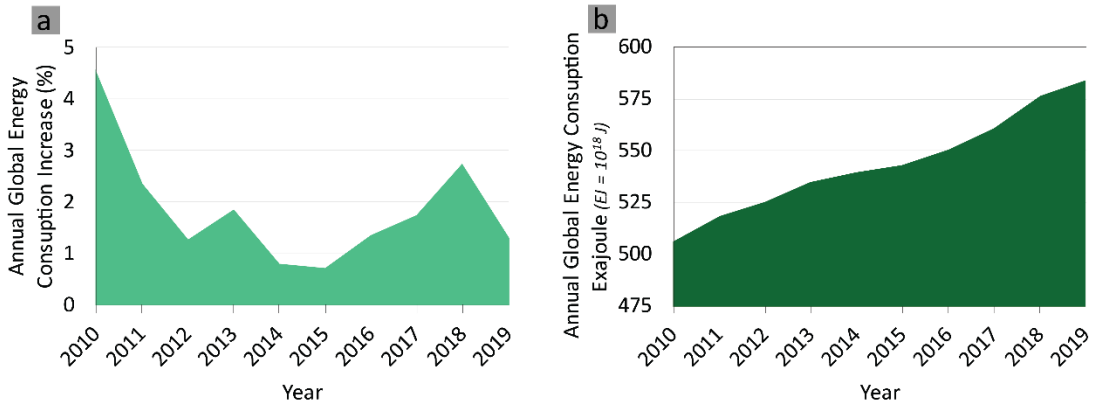

Figure 1.1. (a) Global primary energy consumption per year in exajoules (exajoule, EJ = 10^{18} J). Primary energy is comprised of commercially traded fuels, including renewables for electricity. (b) Annual rate of change (increase) in global primary energy consumption per year (% increase from previous year).[2]

Studies have shown that greenhouse gases are responsible for a significant portion of global warming. Investigations of global warming between 1980 and 1990 indicated that 43% was the direct result of greenhouse gases causing radiative warming[3]. Carbon dioxide is the most important anthropogenic greenhouse gas impacting the global atmosphere; it accounts for 80% of the greenhouse gas contribution to global warming.[3]

Atmospheric carbon dioxide concentrations are due primarily to the use of fossil fuels. Other significant gases such as methane and nitrous oxide are primarily due to agriculture and farming practices.[4] The United States and China are the leading nations for CO_2 emissions, contributing 14.5% and 28.8% of the global share in 2019 (4964.7 and 9825.8 million tons respectively).[2]

The US energy consumption in 2019 was 94.65 exajoules (EJ). This was predominately oil (36.99 EJ or 39%), natural gas (30.48 EJ or 32%), and coal (11.34 EJ or 12%). Only a mere 6% was renewable sources (5.83 EJ).[2] The commercial energy sectors that could most readily utilize higher percentages of renewables if they were available would be transportation and electric power production.[5] The advantageous impacts of cutting back on the use of fossil fuels in these sectors has been more evident than ever in the context of the 2019(-21) global COVID-19 infectious disease pandemic.

In January 2020 the United States reported its first cases of the infectious disease COVID-19 that had already shown alarming levels of transmission in other nations. The spread of this infectious disease in the US was rapid; the U.S. government declared COVID-19 as a public health emergency as of January 31, 2020 and the World Health Organization officially declared COVID-19 a global pandemic in March 2020. Individual states in the US began imposing "stay-at-home" quarantine orders as of March 2020.[6] The impacts of the national response to quarantine at-home have a direct and measurable effect on fossil fuel carbon dioxide ($FFCO_2$) emissions due to drastic changes in human activity. The fossil fuel consumption in the U.S. had a total relative decline of 18.7% between April and May 2020 (a decline of 41,868,500 million tons). Of this, 39% (16,462859 million tons) was from a decrease in gasoline transportation and 30% was

from electricity generation (12,676,128 million tons). The CO_2 emission levels associated with electricity generation measured from March through June show statistically significant declines of up to 30% decreases in emissions.[6] As seen from the dramatic impact of the sudden decrease gasoline transportation and electricity generation, replacing fossil fuels with renewables in these energy sectors would similarly result in a substantial decrease in the national CO_2 emissions.

Photoelectrochemical (PEC) cells have the potential to be a promising solution for alternative renewable energy. PEC water splitting in particular offers a pathway to renewable energy via sunlight by splitting water into hydrogen and oxygen gas, where the only by-product is water. The PEC cell uses a light absorbing semiconductor in connection with a chemical catalyst to drive the water splitting reaction (Eq. 1.1).[7]

$$2\,H_2O(l) \rightarrow 2\,H_2(g) + O_2(g) \qquad \Delta E = -1.23\ V \qquad \text{(Eq. 1.1)}$$

$$2\,H^+(aq) + 2e^- \rightarrow H_2(g) \qquad \Delta E^o_{H^+/H_2} = 0.00\ V \text{ vs NHE} \qquad \text{(Eq. 1.2)}$$

$$2\,H_2O(l) + 4h^+ \rightarrow 4\,H^+(aq) + O_2(g) \qquad \Delta E^o_{O_2/H_2O} = 1.23\ V \text{ vs NHE} \qquad \text{(Eq. 1.3)}$$

The overall reaction (Eq. 1.1) occurs in two half reactions: hydrogen gas is produced at the cathode, consuming two electrons (Eq. 1.2), and oxygen gas is produced at the anode, consuming four holes (Eq. 1.3).[8] A thermodynamic minimum potential of 1.23 V is required to drive the water splitting reaction.[9] In real systems, a potential in excess of this standard potential is required (an overpotential). The overpotential required is due to kinetic barriers associated with the processes. The hydrogen evolution reaction (HER, Eq. 1.2) proceeds with satisfactory currents with very little overpotential; however, the oxygen evolution reaction (OER, Eq. 1.3) has considerable kinetic barriers and requires

substantial overpotentials.[10] Thus, OER, which occurs at the anode, is the limiting component of photoelectrochemical water splitting.

Bridge

This dissertation primarily investigates catalysis for OER, with special focus on structure-stability-activity relationships of a widely used and studied electrocatalysts for OER, Ni (oxy)hydroxide. Chapter II introduces the material and provides a review of the structural, physical, and electrochemical properties. Chapter III focuses exclusively on rigorously ultra-pure (Fe-free) conditions to characterize and study Ni (oxy)hydroxide in the absence of Fe. A new analysis on the structure-stability relationship of Ni (oxy)hydroxide during and after prolonged OER catalysis is presented.

The most active catalyst for OER is not Ni (oxy)hydroxide, but actually an Fe-incorporated species Ni(Fe) (oxy)hydroxide. Chapter IV presents the activity and stability of Ni(Fe) (oxy)hydroxide during and after prolonged OER catalysis operation. There is an emphasis placed on the role of dynamic Fe incorporation/exclusion during operation and the potential role it plays in the both high activity of the Ni(Fe) (oxy)hydroxide material (compared to the Fe-free) and the higher stability.

Chapter V of this work presents an electrode-level-approach to using Ni(Fe) (oxy)hydroxide for PEC applications. In this chapter a full fabrication scheme is presented for photoanodes utilizing Ni(Fe) (oxy)hydroxide as a catalyst. This work builds on the fundamental studies of catalyst stability and broadens the scope to full photoanode stability for OER catalysis.

This dissertation contains entirely unpublished work at the time of authorship. Manuscripts for publication based on the material herein are in preparation.

CHAPTER II

BACKGROUND, PHYSICAL PROPERTIES AND ELECTROCHEMISTRY OF NICKEL (OXY)HYDROXIDE

Chapter II contains fully unpublished material. The content of this review chapter was written by me.

General background and introduction to $Ni(OH)_2$

Ni (oxy)hydroxide, NiO_xH_y, is commonly presented throughout this work as NiO_xH_y, indicating variable oxidation states predominant throughout different phases of operation depending on applied potentials. NiO_xH_y is widely used in electrocatalysis for the oxygen evolution reaction (OER) half-reaction of the overall water-splitting reaction. Ni (oxy)hydroxide has also been extensively used and studied in the battery field. At rest, in alkaline solution, the NiO_xH_y is predominantly the $Ni(OH)_2$ species.[11] The oxygen evolution reaction thermodynamically occurs at 1.23 V vs RHE, which is catalyzed by the predominant NiOOH species at this pH and potential.[11] Thus, when studying Ni (oxy)hydroxide as an OER catalyst it is necessary to also consider the redox behavior of the material since it will be cycling between the oxide and oxy-hydroxide as potential is applied to perform OER. The most general chemical equation for the reduction-oxidation reaction for the conversion between $Ni(OH)_2$ and NiOOH is:

$$Ni(OH)_2 + OH^- \leftrightarrow NiOOH + H_2O + e^- \qquad \text{(Eq. 2.1)}$$

This seemingly simple equation neglects a vital and complex factor that effects the activity and stability of this material: the substantial phase and structural changes that occur during cycling between the products and reactants. The Bode cycle (Fig. 2.1) has

long been accepted as the operative pathway this material will traverse during electrochemical reactions and cycling.[12,13] It established that there are two distinct forms of both the $Ni(OH)_2$ and the NiOOH, thus, four distinct phases that the operative material will cycle through depending on process and application. Figure 2.1 is the Bode cycle arranged and annotated to be most relevant for electrochemical processes, such as OER. Most depictions of the Bode cycle in the literature are from a battery perspective and often feature the initial or starting $Ni(OH)_2$ material as a result of hydrothermal synthesis (which is β-$Ni(HO)_2$ predominantly).

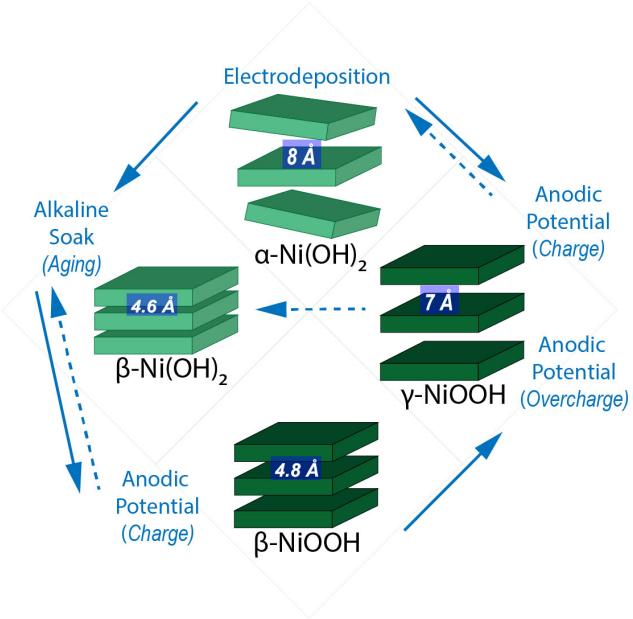

Figure 2.1. The Bode cycle for $Ni(OH)_2$/NiOOH annotated for relevance in electrochemical catalysis.[12,14]

It is critical to stress that when referring to a specific phase, it is merely the *predominate phase* under the given conditions. At any given time, and based on conditions and process, there can be, and often will be, co-existing phases in addition to 'activated' and 'deactivated' states of each.[15] Further, there is recent evidence of an 'intermediate phase' which is an interleaved structure of both α- and β-$Ni(OH)_2$.[16–18]

Physical properties and structure of the NiO_xH_y phases

Cathodic electrodeposition of $Ni(OH)_2$ from a Ni salt solution, such as $Ni(NO_3)_2$, leads to the α-$Ni(OH)_2$ phase.[19] The α-oxide is the most disordered and has the largest sheet spacing (~8 Å) of all four possible phases.[13] This phase is meta-stable, and readily converts into the β-$Ni(OH)_2$ after aging (exposure to and soaking in alkaline solutions). Although the four phases of the Bode cycle interchange in a complex manner depending on conditions and treatment, generally there are two redox pairs that will interconvert during cycling. The disordered, wide-spacing α-$Ni(OH)_2$ oxidizes to γ-NiOOH; this redox pair is hereinafter referred to as the α/γ pair. The ordered, close-packed β-$Ni(OH)_2$ readily oxidizes to the β-NiOOH; this redox pair will be referred to as the β/β pair.

The α-$Ni(OH)_2$ and β-$Ni(OH)_2$ have the same crystal structure with hexagonal layered structure. However, the inter-layer chemistries are notably different due to the differences in the degree of order, sheet spacing, and average oxidation state of the Ni^{+n}.[20] The sheet stacking for the β-$Ni(OH)_2$ is the tightest of all four phases, with sheet spacing of ~4.6 Å. The electrodeposited α-$Ni(OH)_2$, with ~8 Å sheet spacing, has intercalated water and anions causing a turbostratic-disordered structure.[17,21–24] The sheet spacing for the α-oxide are larger and resultantly, the Ni-Ni bond length contract by 0.05 Å; the Ni-Ni bond length in the β-phase is 3.13 Å, and 3.08 Å for the α-phase [20]. Thus, the α-$Ni(OH)_2$ has slightly stronger intramolecular bonding than the β-$Ni(OH)_2$ phase. Figure 2.2 is an illustration reproduction of early work done by Delahaye-Vaidal and Figlarz characterizing the two distinct phases of $Ni(OH)_2$.[21]

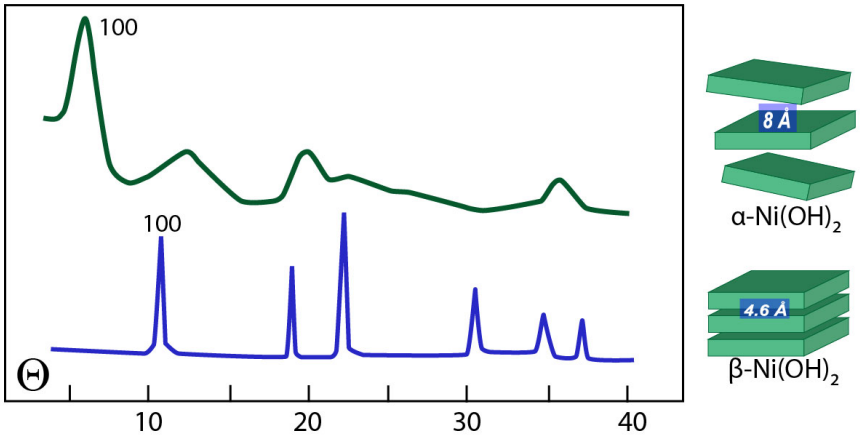

Figure 2.2. Illustration reproduction of Delahaye-Vaidal and Figlarz X-ray diffraction patterns collected for α-$Ni(OH)_2$ (green line) and β-$Ni(OH)_2$ (blue line).[21] The β-$Ni(OH)_2$ phase (blue) has well defined shape diffraction peaks indicating a high degree of crystallinity. The α-$Ni(OH)_2$ phase (green) has broad peaks indicating a more disordered structure.

The differences in the structure order/disorder are readily observed from the X-ray diffraction patterns. The sharp peaks of the β-phase indicate high degree of crystallinity, and broadening present in the α-phase pattern indicates a less crystalline and more amorphous material. The predominate species at ambient conditions is $Ni(OH)_2$ and is easily characterized via ex situ techniques such as XRD. However, since the NiOOH phase is only predominate in-situ at high oxidizing potentials and in alkaline electrolyte, characterizing the NiOOH is challenging.[13]

Oxidation state, conductivity and electrochemistry

The charge of the α- and β-$Ni(OH)_2$ are fairly identical, with an average oxidation state of 2.0^+ to 2.2^+ respectively. However, the corresponding oxy-hydroxide forms have notably different oxidation states. When the α/γ pair is oxidized from α-oxide ($Ni^{\sim 2+}$) to the γ-oxy-hydroxide it has an average state of 3.5^+ to 3.7^+. When the β/β pair is oxidized from β-oxide ($Ni^{\sim 2+}$) to the β-oxy-hydroxide it has an average state of 3^+.[15] The higher

oxidation state α/γ pair leads to higher charge capacities. One explanation for this is the larger sheet spacing of the α/γ pair allow for more intercalated water ions and cations.

The conductivity of the NiOOH species is five orders of magnitude higher than that of the $Ni(OH)_2$ species. Resultingly, there is a conductivity 'turn on' potential near 100 mV overpotential when the $Ni(OH)_2$ has been converted to NiOOH.[25] The efficiency with which the material can entirely cycle between $Ni(OH)_2$/NiOOH will have a significant impact on the conductivity of the overall material and correspondingly the effectiveness of the material to pass current during OER. Further, there is a notable difference in the conductivity between the β- and γ-oxy-hydroxide.[23] The difficult to preserve α/γ pair is reported to have better electrochemical performance than the β/β pair.[26] However, it is known that upon discharge/charge cycling the non-conductive phases can be trapped as non-conductive components of a resistive matrix of species/phases.[15,27,28]

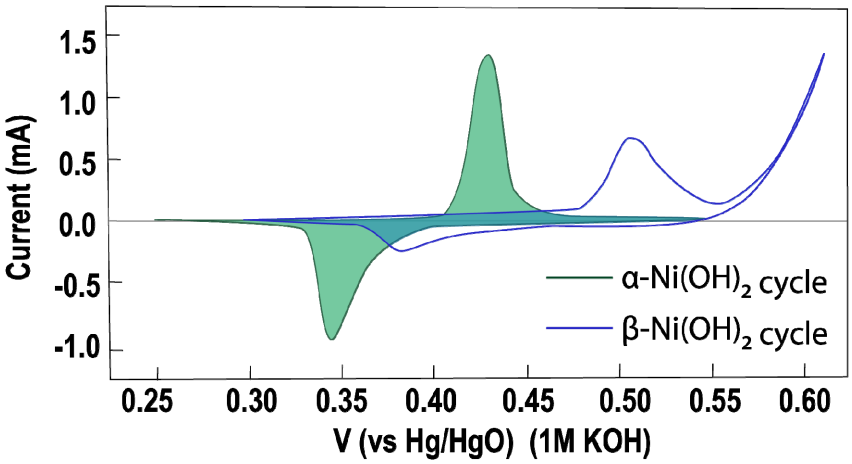

Figure 2.3. Illustration reproduction of cyclic voltammetry data on the $Ni(OH)_2$ material in the distinct α- and β-$Ni(OH)_2$ phases. Replication is of combined data from Cheek and O'Grady[29] and Wehrens-Dijksma and Notten.[14]

The α/γ and β/β pairs have distinct difference in their reduction potentials, and as such, have distinct cyclic voltammetry (CV) character (Figure 2.3). A freshly electrodeposited α-$Ni(OH)_2$ will have redox peaks at 0.43 V (oxidation) and 0.34 V (reduction) vs Hg/HgO respectively (in 1 M KOH). The β-$Ni(OH)_2$ phase, obtained by controlled hydrothermal synthesis or aging of the α-phase, presents with redox peaks that are shifted anodic and have a greater $peak_{an}$-$peak_{cat}$ spacing. The β- oxidation and reduction peaks are observed at 0.50 V (oxidation) and 0.38 V (reduction) vs Hg/HgO (in 1 M KOH). The integration of the redox peaks are greater for the α-phase compared to the β-phase, as well as the β-phase present with more asymmetry in anodic/cathodic peak integration; typically the β-phase anodic peak integration is greater than the cathodic integration.[14,29]

Conclusion and bridge

This brief review of the physical properties of the NiO_xH_y material demonstrates how inherently complex the material is. It is important to note, the above survey of NiO_xH_y applies to the pure material. However, in practice NiO_xH_y is rarely pure and nearly always includes Fe contamination (among many other cation species that can be incorporated from solution contamination). This Fe inclusion impacts significant aspects of NiO_xH_y including catalytic activity for OER, structure, and stability. Thus, if one desires to study NiO_xH_y great care must be taken to have rigorously Fe-free experimental conditions. Much of the work done in the last several decades were not reported to be rigorously Fe-free, thus, the results, discussions, and analysis leave room for debate regarding the applicability to the pure NiO_xH_y material or the common Fe-contaminated $Ni(Fe)O_xH_y$. Further, due to rigorous control of Fe-contamination being reported

diligently only in the last decade, there is a need to characterize and investigate the pure NiO_xH_y material for OER catalysis. The majority of this dissertation investigates the stability of pure NiO_xH_y, during and after prolonged OER catalysis, which is intimately connected to the structural changes that occur in operando.

CHAPTER III

STABILTIY, DEGREDATION, AND REGENERATION OF THE NICKEL (OXY)HYDROXIDE CATLAYST FOR THE OXYGEN EVOLUTION REACTION

Chapter III contains fully unpublished material. Prof. Boettcher and I conceived of the project. I performed and directed experiments, collected data, and analyzed data, as well as directed experiments that were conducted by L. Liu and several undergraduates. The content and analysis of this chapter was written by me with editorial assistance from Prof. Boettcher.

Introduction

$Ni(Fe)O_xH_y$ is presently known as the most-active catalyst for oxygen evolution reaction (OER) in alkaline electrolytes.[30] Much work has been done to understand the activity, mechanism, and stability of this catalyst.[31] Recently there has been a substantial amount of work focused on the stability-activity relationship of the $Ni(Fe)O_xH_y$ system. Several theories which are closely aligned have been emerging regarding the dynamic role of Fe incorporation and the impact it has on the stability of the catalyst.[32–34] However, the prolonged activity-structure-stability relationship of the NiO_xH_y material without Fe incorporation are not well studied in recent years. Understanding how this principal structure transforms and activates/deactivates without the presence of Fe might elucidate pathways for stabilizing the desired $Ni(Fe)O_xH_y$ structure for optimal OER activity.

The leading hypotheses for the mechanism of deactivation for $Ni(Fe)O_xH_y$ involves leaching of Fe from the either surface or interior sites of the mixed metal catalyst. The optimal Ni/Fe ratio for OER activity is roughly $Ni_{0.75}Fe_{0.25}O_xH_y$.[35,36] However, our work presented in Chapter IV indicates that there is no substantial Fe leaching and/or adsorption during prolonged OER operation that would impact stability. We show loss of OER activity in electrodes with stable Fe-content which we hypothesize may be due to changes with the structure of the material that affect activity, and not merely due to dynamic Fe. The intrinsic high activity of $Ni(Fe)O_xH_y$ is due to Fe-incorporation, however, meticulous studies of the base structure of NiO_xH_y in the absence of the enhancing Fe remains important. Design of electrocatalysts for oxygen evolution and water-splitting requires extensive knowledge of active-sites, catalytic mechanisms, structure-activity relationships, and pathways for degradation. This work characterizes the mechanisms for degradation of the NiO_xH_y during the OER.

Degradation pathways

$Ni(OH)_2$/NiOOH materials dynamically change throughout electrochemical analysis and operation as an OER catalyst. After electrodeposition, the material is initially in the disordered α-$Ni(OH)_2$ phase. As discussed in Chapter II, during electrochemical cycling, operation, or merely aging in electrolyte, the material can convert to the ordered and less electrochemically active β-$Ni(OH)_2$.[13] This transformation to the β-phase impacts the lattice structure (close-packed sheets versus larger sheet spacing) and electronic structure (lower average oxidation state) of the material, and thus, the physical properties are altered. These properties are discussed in detail in Chapter II of this dissertation. Characterizing the active material is a challenge due to these

transformations. To further obfuscate characterizing the active material at any given time, the incorporation of Fe into the system has pronounced effects on many aspects of the material, even trace amounts that are unintentionally incorporated.[37] Thus, analyzing and interpreting the electrochemical data as it evolves during operation can be complex. This work hypothesizes that there are two primary pathways for deactivation (and potential reactivation) of the NiO_xH_y material: semi-irreversible structural/phase changes and semi-reversible deactivation likely via charge trapping.

Semi-irreversible structural changes

The β-$Ni(OH)_2$ phase is more thermodynamically stable than the α-$Ni(OH)_2$.[38–40] On a fundamental level, one would predict that the NiO_xH_y material will move towards the β-phase to minimize system internal energy. In actuality, there may be a continuum of species present in an electrochemically perturbed $Ni(OH)_2$ system. However, to simplify the model we neglect other potential minor species. If we imagine that pure $Ni(OH)_2$ is a binary system (α- and β-phase) it would be reasonable to assume that to minimize the system internal energy the α-phase would convert to β-phase. This process is called coarsening, and occurs in countless metallic and nonmetallic systems.[41]

The system could be modeled by the difference in Gibbs free energy of the two phases, where the β-$Ni(OH)_2$ would have a more favorable free energy, thus the equilibrium over time will shift towards the β-phase despite a primarily α-phase deposition. However simply modeling the minimization of energy would neglect relevant pathways for these phase transformations wherein electrochemical processing could cause inhomogeneous regions of the binary mixture of various sizes. Cycling applied potentials such that repeated oxidation/reductions of NiO_xH_y may cause regions of the

different phases whose sizes vary. An initial α-phase (from electrochemical deposition) will have β-phase dispersed in the matrix and in an increasing volume ratio as the material is aged. The total energy of the two-phase system can be minimized by increasing the size of the β-phase (and a corresponding reduction in size of the α-phase). This process is Ostwald ripening/coarsening, which may occur in any instance where first-order transitions (α-phase to β-phase) results in a two-phase mixture. This chapter applies an Ostwald model to the phase transformation from α- to β-phase and we hypothesize there are two electrochemically assisted pathways producing different morphology and diffusion. We hypothesize that electrochemical treatment can produce a NiO_xH_y materials with two different morphologies which have different electrochemical activity and reversibility due to dissimilarities in porosity and grain boundaries.

Electrochemical accessibility, reversibility and charge trapping

In electrochemical catalysis one must consider the conductivity of the electrode material, the ionic conductivity of the electrolyte, and the electrolyte mobility (to, around, and through the catalyst). Electrochemical accessibility is a primary factor in assessing catalytic activity of a electrocatalysts. Fundamentally, the electrochemical accessibility is described as how many atoms (with respect to total loading) in the material can undergo an observable reduction and oxidation process. This is especially vital for Faradaic processes where the surfaces and interfaces of the catalyst is most relevant. Diffusion controlled reactions are sensitive to film thickness and porosity as the reactions take place at the surface region. Faradaic current is increased with increasing porosity for thin films. These effects have been studied extensively on model systems such as Pt planar and porous electrodes.[42] A highly porous material is likely to have high electrochemical

accessibility due to the electrolyte being able to fully permeate the material, facilitating up to 100% of the atoms to be used for catalysis. In contrast, in a material with little to no pores the electrolyte will need to pass around and through the limited pores to make contact with the surface of the catalyst.[43,44]

The α-phase obtained via electrochemical deposition has a turbostratic structure, meaning the sheet-structure of the material has misaligned and rotated layers that are easy to break apart, with more grain boundaries and structural defects than a properly stacked phase (β-phase). This work proposes that with increased electrochemical cycling of the $Ni(OH)_2$ catalyst the turbostratic α-phase structure converts to a less defective, less porous, and more densely packed morphology as it converts to the ordered β-phases. This causes a notable irreversible decrease in electrochemical accessibility which presents as a decrease in redox peak integration with cycling. As the material is cycled, the accessibility decreases along with the electrochemical reversibility. We hypothesize this is due to charge trapping of the material in a higher oxidation state.

Experimental

Electrolyte preparation and purification. All electrolyte (unless explicitly stated otherwise) used in this chapter is 0.1 M KOH (semiconductor grade 99.99% trace metal basis) which was rigorously cleaned of Fe impurities using a high-purity $Ni(OH)_2$ Fe-absorbent soak (~ overnight), as previously reported.[37] In previous works rigorously Fe-free solutions have been prepared using this cleaning technique, which has proven to remove Fe impurities existent in even the highest purity semiconductor-grade electrolytes.[37] However the Ni-based absorbent leaves behind $Ni(OH)_2$ particulates in the solution, leading to undesirable deposition onto working electrodes during experiments.

In these experiments it is vital to accurately quantify the catalyst loading before and after operation to assess if degradation is due to dissolution/loss of catalyst or deactivation. Accordingly, any unintentional deposition of $Ni(OH)_2$ during operation will make quantification of the retention/loss of catalyst unintelligible. Accordingly, prior to use, the Fe-cleaned electrolyte was filtered twice using a 0.1 μm Supor (polyethersulfone) membrane syringe filters (VWR, Pall Acrodisc®) to remove remaining $Ni(Fe)O_xH_y$ particulates. Necessity for this additional cleaning procedure and characterization of unwanted $Ni(OH)_2$ deposition from solution particulates can be found in Appendix A, Figures A.1 – A.2.

Electrochemical catalyst deposition and characterization. NiO_xH_y films were electrodeposited onto clean Pt foil electrodes from a 0.1 M $Ni(NO_3)_2$ solution. Depositions were performed in a glass cell using a two-electrode set-up with a home-made carbon cloth (Fuel Cell Earth) counter electrode by applying -0.1 mA cm^{-2} for 120 s. Immediately following the deposition, the electrodes were electrochemically characterized by performing cyclic voltammetry in ultra-pure 0.1 M KOH. Catalyst loading was determined by integration of the anodic peak. The depositions on the home-made Pt foil electrode substrates produced electrodes with fairly consistent mass loadings (~ 4 ug/cm^2 Ni), but with variable absolute catalyst loading due to the slight variations in the surface areas of the home-made Pt electrodes (between 400-1000 ng Ni per electrode with varying surface areas of electrodes).

Electrochemical analysis and characterization. Electrochemical experiments in this chapter were performed in rigorously Fe-free 0.1 M KOH in a PTFE cell using precisely 10 mL of electrolyte. The three-electrode set up used a Hg/HgO reference electrode and a

freshly cleaned (1 M H_2SO_4 and aqua regia) Pt coil as the counter electrode. Cyclic voltammetry (CV) and steady-state chronoamperometry (CA) measurements were recorded using a BioLogic SP200 or SP300 potentiostat in a Nalgene® three-electrode cell with a Pt-wire counter electrode, Hg/HgO (CH Instruments) reference electrode. CVs were performed with a scan rate of 10 mV s^{-1}. Uncompensated resistances were measured to be 20-50 Ω for all electrodes, which are within expected range for 0.1 M KOH.

Results and Discussion

Fresh electrodeposited Ni (oxy)hydroxide catalyst have higher OER activity than cycled catalysts. Chronoamperometry was performed with an applied potential of 1.0 V-iR vs Hg/HgO (0.688 V-iR overpotential) on a series of electrodes with varying amount of cyclic voltammetry prior to chronoamperometry. The electrode with the least electrochemical cycling prior to chronoamperometry (only 3 CV to characterize the catalyst) has the highest OER activity. As seen in Figure 3.1, as the number of CV cycles prior to chronoamperometry increases, the OER current activity decreases. Current activity is reported here as current per catalyst loading (mA/μg cm^{-2}) to normalize for slight variations in both surface area and catalyst loading from sample to sample. Corresponding current densities are reported in Appendix A, Figure A.3, along with Table A.1 containing the surface areas and catalyst loadings for each electrode. Catalyst loading was determined via charge integration of the redox peaks immediately following electrodeposition and reported as μg/cm^2 of Ni atoms.

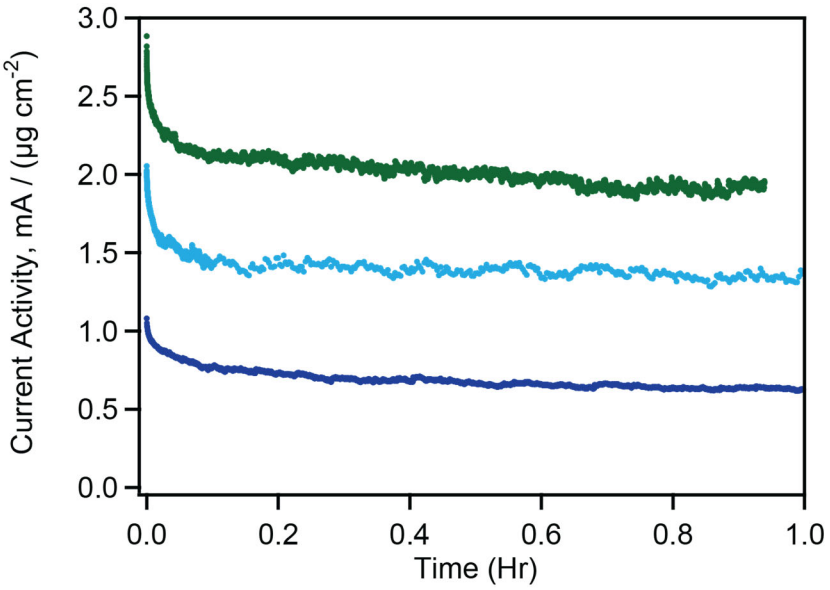

Figure 3.1. Chronoamperometry operated at 1.0 V-iR vs Hg/HgO (0.688 V-iR overpotential) after 3 CVs (green) electrochemical cycling prior, 20 CVs prior (teal), and 40 CVs prior (dark blue).

Upon fresh electrodeposition the catalyst is in the α-$Ni(OH)_2$ phase.[19] As the materials is cycled it is transformed from the turbostratic hydroxide to the more ordered phase: α → β, much as it would via aging conditions in alkaline solution.[21] Here, based known CV characteristics of α- and β-phases[14,29], we posit the decrease in OER activity is correlated the decrease in α-NiO_xH_y as the predominate species, where the material is converting from primarily α-NiO_xH_y (only 3 CVs), to increasing predominance of β-NiO_xH_y (after 20 CVs and 40 CVs). These OER current activities correspond to current densities between 20-50 mA/cm^2 (Figure A.3).

The long-term OER current stability is correlated to stability in redox peak position shifting. Cyclic voltammetry was performed immediately before and after chronoamperometry on two electrodes, one intentional Ni(Fe)O_xH_y and another in rigorously Fe-free conditions (Figure 3.2). The Ni(Fe)O_xH_y electrode performs OER (when Fe^{3+} is present in the electrolyte) with a **very stable** current output over 4 h

(1.0 V-iR vs Hg/HgO, 0.688 V-iR overpotential). The rigorously Fe-free Ni(Fe)O_xH_y performs OER under the same conditions with **continuous degradation** over the 4 h operated. The difference in stability between the two can be examined not merely in terms of Fe-inclusion, but in terms of the electrochemical character of the electrodes. When the catalyst has stable performance, there is no shift in the $Ni(OH)_2$/NiOOH redox peak position before and after operation. On the other hand, when there is degradation in the OER current, the post-operation cyclic voltammetry reveals a significant ~250 mV anodic shift in the $Ni(OH)_2$/NiOOH peak position. The difference in the OER onset and max current density is due to the known enhancements resulting from Fe-inclusion.[37]

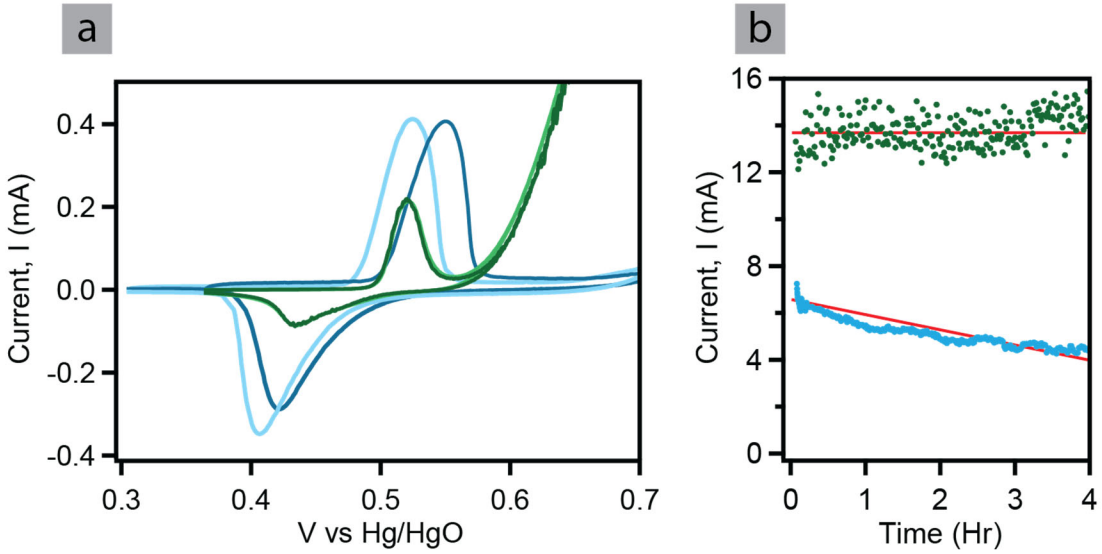

Figure 3.2. (a) Cyclic voltammetry of $Ni(Fe)OH_2$ (green traces) before (light green) and after (dark green) prolonged OER operation. Cyclic voltammetry of Fe-free $NiOH_2$ (blue traces) before (light blue) and after (dark blue) prolonged OER operation. (b) Chronoamperometry performed at 0.688 V overpotential on $Ni(Fe)OH_2$ (green) and Fe-free $NiOH_2$ (blue). Red linear traces are provided as a guide for the eye.

There is an acknowledged correlation between Fe-uptake and an anodic shift in the redox peak position.[45] Thus, there may be concerns that the Fe-free electrode is undergoing slow Fe-uptake over time. However, the experiment here is assuredly Fe-free

as evidenced by: (i) the electrolyte and electrode were prepared in rigorously Fe-free conditions (ii) there is no increase in OER current, which would be evident in the cyclic voltammetry if even trace Fe was present; and (iii) ICP-MS was conducted on the digested electrode post operation and there was no Fe detected above the levels of detection for the experiment (non-zero detection of Fe via ICP-MS was on the order 1-10 ng consistent with Fe-free controls limits of detection for Fe).

Klaus and coworkers have shown that $Ni(OH)_2$ aged in Fe-free KOH over 6 days will present with an anodic shift in NiO_xH_y redox peak positions, and an increase in OER overpotential (i.e. a decrease in OER activity).[45] Following the Bode scheme for phase changes of the material, this is in line with the deposited α-phase (more electrochemically favorable) converting to β-phase (less electrochemically favorable) when aged in alkaline solution. Further, their quartz crystal microbalance (QCM) studies provide evidence that the aged catalyst has (to an indeterminate extent) converted into the β-phase.[45] These conclusions from the literature alongside the evidence presented here are in support of our hypothesis that the Fe-free α-phase as deposited converts to the β-phase during prolonged OER applied potential analogous to an aging process. Superficially, this seems in contradiction to the well-accepted Bode-cycle, where 'overcharging' conditions should convert the α-$Ni(OH)_2$ to the γ-NiOOH instead of the β-NiOOH. The Bode cycle traditionally used in the battery community refers a regime where the NiO_xH_y material is held at a charging state (the NiOOH species) for a prolonged period. Translation of these principles to electrochemical catalysis (rather than battery research) may lead one to conclude that 'overcharge' and prolonged catalysis are analogous. However, it is our hypothesis that holding an applied potential *such that the*

catalyst is driving OER is not in fact 'overcharging' the material. If the applied potential resulted in Faradiac processes occurring (OER), the material is not necessarily being merely 'held in overcharging'.

Reduction in redox peak integration with increased electrochemical cycling correlates to a less electrochemically active material. A decrease in OER activity after prolonged operation can be directly related to the degree of electrochemical cycling prior to chronoamperometry. The electrodeposited α-$Ni(OH)_2$ will convert to β-$Ni(OH)_2$. However, the process by which the material is allowed to proceed through the phase transition can have significant impacts on the stability and regenerative ability.

Chronoamperometry at 1.0 V-iR vs Hg/HgO was performed for 4 hours, with cyclic voltammetry performed before and after each 4-h operation period (Figure 3.3). The number of CV cycles was increased for each electrode, where 5 cycles was the minimum (Figure 3.3a) and 50 cycles was the maximum tested (Fig. 3.3d). There is a direct correlation between increasing CV cycles and decrease in redox peak integration. It is important to note that the degree of anodic shift in the redox peaks are fairly consistent across the electrodes, which we propose indicates equivalent overall phase transformation from α- to β-phase. The principle difference in the data is the loss of peak integration and loss of electrochemical activity after numerous CVs. We propose this can be explained by the two pathways producing **different morphology** and thus **dissimilar diffusion** resulting from the electrochemical treatment.

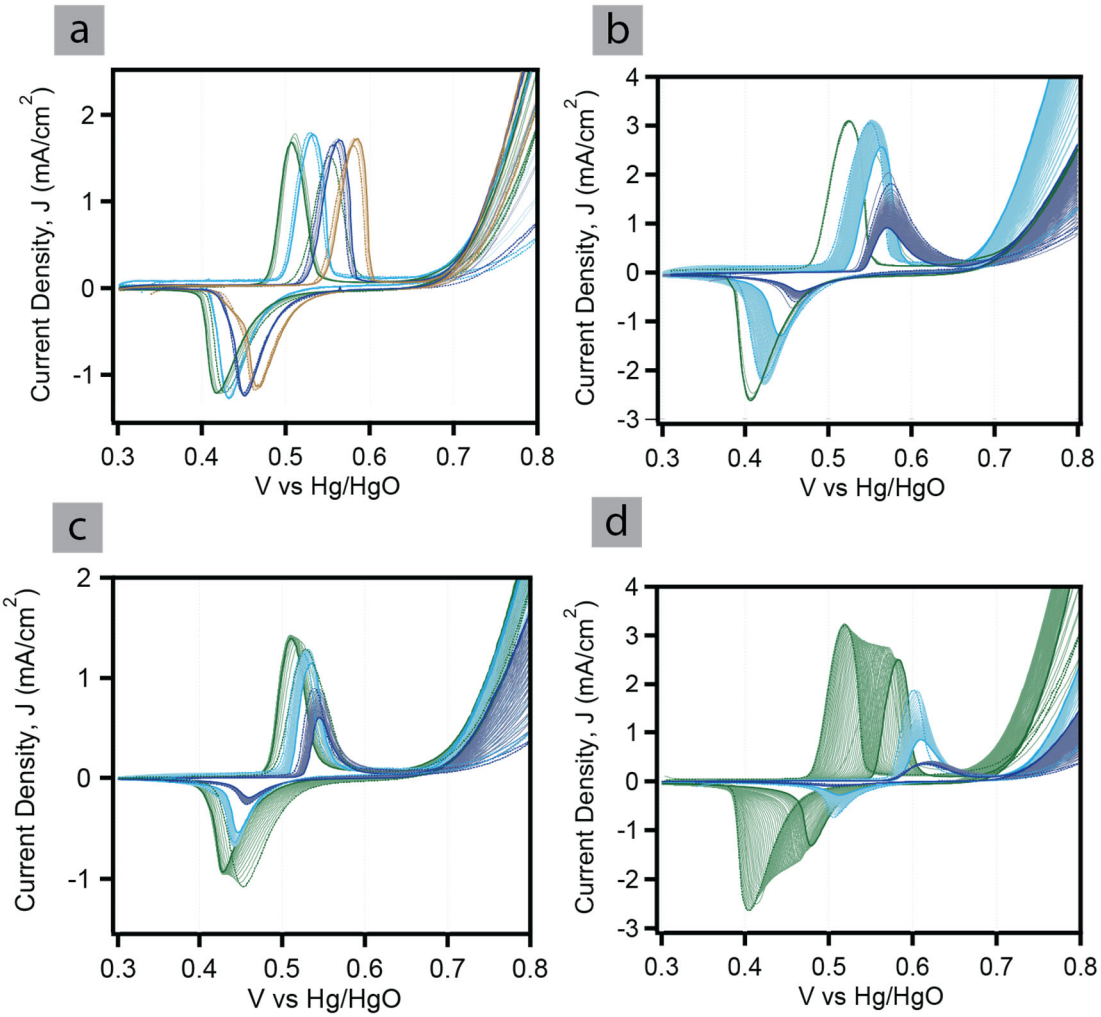

Figure 3.3. Cyclic voltammetry performed on Fe-free $NiOH_2$ every 4 hours of prolonged OER operation at 0.688 V overpotential. Green traces are first CVs before CA. Teal traces are CVs after 4 hours CA. Blue traces are after another 4 hours CA (8 hours total). Gold traces are after another 4 hours CA (12 hours total). Dashed traces are the first cycle and solid traces are the final cycle. (a) 5 CV cycles every 4 hours, (b) initial 5 cycles, 50 CVs every 4 hours, (c) 20 cycles every 4 hours, (d) 50 CVs every 4 hours.

We hypothesize that the transition between α/β-phases can be described using a standard Ostwald ripening model. For quintessential Ostwald ripening there is a binary system with particles of an average intrinsic 'small-radius' and an average intrinsic 'large-radius' property. Over time the 'large-radius' particles grow and the 'small-radius' particles shrink until there is conversion to the species with the larger particle size. In this

case, the α-Ni(OH)$_2$ are the 'small-radius' particles, whereas the α-phase is the more turbostratic phase with many grain boundaries. The β-phase is the "large-radius" particles, whereas β-phase forms ordered sheet stacks with less grain boundaries. Initially, upon pristine cathodic electrodeposition, the α-Ni(OH)$_2$ phase is deposited with an average particle 'radius' of R_α. At this time, the assumption is that there are nominal or no β-Ni(OH)$_2$ phase present, which have a larger average particle size, R_β*. Initially the number of particles is represented as $R_\alpha > R_\beta$*. Over time, Ostwald ripening leads to continual growth of R_β*, where eventually $R_\alpha \ll R_\beta$*. The size of R_β* (regions of the ordered β-Ni(OH)$_2$ phase) depends directly on the diffusion, and we propose that the morphology and diffusion is determined by the electrochemical processing.

Ostwald ripening provides an asymptotic growth rate of the average spherical particle, thus the average particle radius, $\bar{R}$, with respect to concentration, C, and the diffusion, D, as given in Equations 3.1-3. According to classical Ostwald formulation,[46] the average particle size is proportional to the cube root of the diffusion (Eq. 3). The apparent diffusion through a porous medium is less than the molecular diffusion. Thus, more porosity will lower diffusion and will lead to a decrease in average particle size.

$$\frac{d}{dt}\left(\frac{4\pi}{3}R^3\right) = 4\pi R^2 \mathcal{D}\left.\frac{dC(r)}{dr}\right|_{r=R} \quad \text{(Eq. 3.1)}$$

$$\frac{dR}{dt} = \mathcal{D}\left(\Delta_C - \frac{l_c}{R}\right) \quad \text{(Eq. 3.2)}$$

$$\bar{R}(t) = \left(\frac{4\mathcal{D}l_c t}{9}\right)^{1/3} \quad \text{(Eq. 3.3)}$$

The physical properties of the particle are combined and termed the capillary length, l_c. For mathematical ease, several variables are represented in the capillary length here as dimensionless terms (Eq. 3.4).

$$l_c = \frac{2\gamma \mathrm{V}_m}{R_B T} \cdot \frac{1}{r} = \frac{2\gamma \mathrm{V}_m C_\infty}{R_B T} \qquad \text{(Eq. 3.4)}$$

Where γ is the specific interfacial energy (mJ/m^2) of the matrix-particle boundary, V_m is the molar volume of the particle (m^3/mol), R_B is the universal gas constant, and T is temperature. C_∞ is the concentration at the interface of the particles.

When the material is cycled through many CVs the turbostratic structure is opened and closed rapidly and repeatedly (depending on number of cycles). We propose this increases the sheet contact and gradually decreases the degree of grain boundaries. Thus, our hypothesis is that the material becomes less porous and has less grain boundaries than the original highly disordered alpha phase (Figure 3.4). On the other hand, with minimal CV cycling prior to the CA operation, the sheet contact is minimized and the average R will be lower overall. The material is still undergoing an overall transition from α- to β- phase at a comparable rate, but the character overall is more similar to the favorable turbostratic structure, with many grain boundaries and pores (Figure 3.4c and 3.4d). This hypothesis agrees with the chronoamperometry data (Fig. 3.1) indicating a continual decrease in maximum OER current achieved with an increase in CV cycling prior to operation. The fairly consistent rate of decay during prolonged applied bias correlates to our hypothesis that there is ongoing conversion from α- to β- phase due to thermodynamics notwithstanding the cyclic voltammetry assisted Ostwald-type ripening (Fig. 3.4).

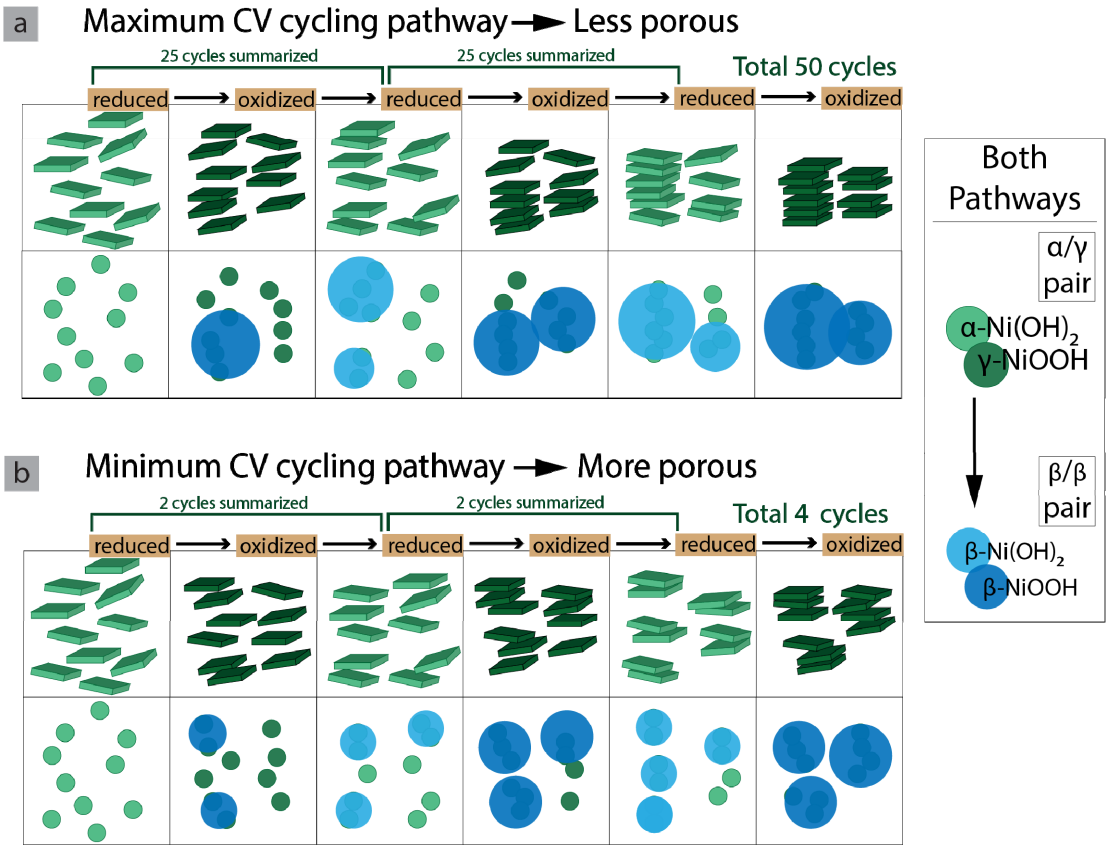

Figure 3.4. Depiction of α/γ redox pair converting to β/β pair via two different electrochemical processing pathways. (a) Maximum CV cycling of initial α/γ (green circles) producing larger β/β zones (blue circles) and a less porous result. (b) Minimum CV cycling of initial α/γ (green circles) producing smaller β/β zones with more boundaries and a higher porosity (blue circles). Side panel indicates the overall transition from green to blue (aside from size of circles) represents the overall thermodynamic phase change process of α/γ to β/β.

The degree of cyclic voltammetry impacts the electrochemical reversibility and recovery of OER current. As the number of CV cycles increase prior to the constant voltage hold there is a large decrease in redox reversibility; the redox peak integration not only decreases as discussed above, but there is increasing difference between the integrated charge in the cathodic and anodic peaks. The electrochemical reversibility factor, χ_{rev}, is determined by the ratio of the anodic and cathodic redox peak integrations, $\chi_{rev} = \frac{Q_C}{Q_A}$, where Q_C is the cathodic peak integration and Q_A is the anodic peak integration. For fully reversible redox process $\chi_{rev} = 1$. When $\chi_{rev} < 1$ the material is not fully reversible; a

portion of the charge is not reduced via the typical reduction potential and not accounted for in the integrable reduction peak.[28]

Table 3.1. Electrochemical reversibility factor, $\chi_{rev,}$ as a function of increasing cyclic voltammetry cycling between chronoamperometry. Integrations were calculated on the first cycle of each respective series.

Electrochemical Cycling	χ_{rev} 4 Hours	χ_{rev} 8 Hours	χ_{rev} 12 Hours
5 CVs	0.99	0.89	0.95
20 CVs	0.71	0.26	0.19
50 CVs	0.52	0.21	--

The reversibility factors for the electrodes shown in Figure 3.3 are reported in Table 3.1. With minimal CV cycling the reversibility of the material is nearly fully reversible. As CV cycling increases the χ_{rev} decreases, indicating increasing charge trapping. This increase in charge trapping corresponds to the decrease in porosity of the material. Figure 3.5 demonstrates the impact on the maximum OER current: a minimally cycled electrode loses current density during the CA operation, but regains 100% of the lost current activity upon minimal CV cycling. On the other hand, a highly cycled electrode loses current density during CA and does *not* recover all of the lost current activity. The OER current recovery is reported in Figure 3.5d. Here, it can be seen that the more an electrode is cycled (before and between CA) the less it is able to regenerate to the maximum OER activity. There is a notable regeneration effect for all electrodes tested, however, only the minimally cycled electrode regained OER activity to maximum levels.

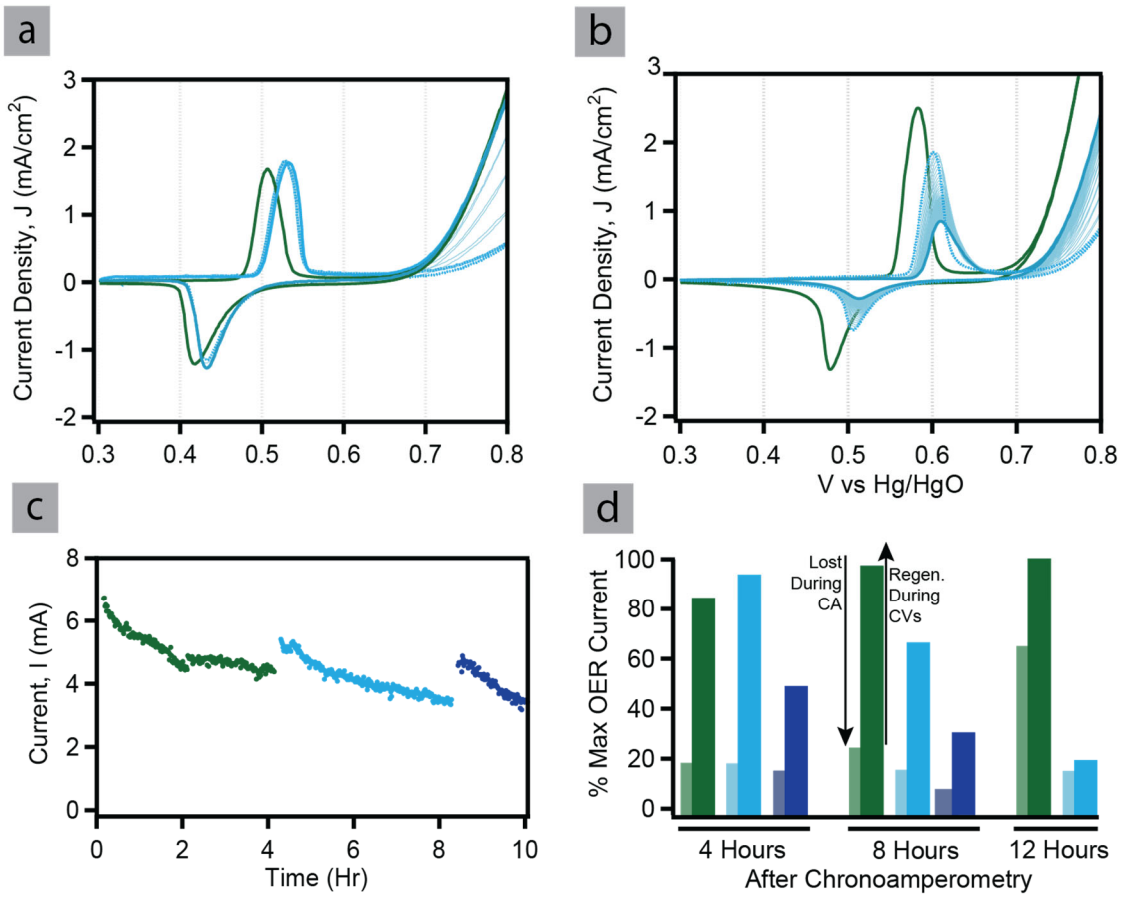

Figure 3.5. CV cycle immediately before chronoamperometry (green traces), CV cycle immediately after 4 h chronoamperometry (teal dotted trace), and after CV regeneration (teal solid line). (a) 5 CV cycles before and after CA, regeneration is nearly 100% effective. Green trace is cycle 5. (b) 50 CV cycles before and after CA, only partial regeneration. Green trace is cycle 50. (c) Chronoamperometry with applied potential at 0.688 V overpotential. Performed on the "5 cycle" sample with degradation of current over the 4 hours, and regeneration (gap regions) resulting from the CVs. (d) OER current lost and regenerated every 4 hours during the CV cycling. Current is characterized at 0.8 V vs Hg/HgO and is normalized to the maximum OER current for the given electrode. The light bars are the OER current lost during the CA, and the dark bars are the current regenerated from the CVs. Green bars are the '5 CV electrode', Teal bars are the '20 CV electrode', and Blue bars are the '50 CV electrode'.

Consistently, when there is no Fe present, the NiO_xH_y electrodes show that the (i) higher OER current densities and (ii) regeneration of trapped charge, is correlated to the electrochemical processing (i.e. degree of CV cycling). As cycling increases there is a decrease in redox reversibility and loss in OER activity that is not reversed by CV re-activation. These results may be explained by the fact that the more-cycled electrodes

have less boundaries, and are less porous. Thus, there is less surface and accessible catalytic sites. This hypothesis could be tested further via TEM analysis of the material before and after cycling. Additionally, this hypothesis is consistent with studies from the battery research findings that a porous structure provides a higher discharge capacity than a bulk structure.[47]

The OER activity loss during chronoamperometry can be partially recovered. During chronoamperometry of the Fe-free NiO_xH_y the OER current decays notably over the course of only a few hours. We propose this is primarily the result of charge trapping under prolonged operation. The more porous, less CV cycled electrodes can regenerate the lost OER activity by pausing the CA to perform minimal cyclic voltammetry, wherein the cyclic voltammetry acts as a regenerative process. Our hypothesis stated above was that prolonged OER operation is *not* analogous to holding a catalyst in an 'overcharging' regime as assumed by the Bode cycle (which would lead to a phase transformation to γ-NiO_xH_y.). We further investigate this and examine if the deleterious effects from prolonged OER are also observed in a regime of more accurate 'overcharging'. Chronoamperometry at (a) 0.8 V vs Hg/HgO and (b) 0.65 V vs Hg/HgO was performed for 2 h, with minimal characterizing cyclic voltammetry performed before and after each 2-h operation period (Figure 3.6).

Potential hold (a) represents the prolonged operation, non-overcharging state. Potential hold (b) represents an electrochemical analog to an overcharging state. The non-overcharging electrode (a) has an initial slight improvement in OER activity after the

first CA period, yet there is **no further improvement to the catalysis** and the electrode presents with a clear decrease in electrochemical reversibility over time (χ_{rev}).

Potential hold (b) represents an overcharging electrode state. Here, (b) presents with a continuing increase in OER activity after each CA overcharging hold. Further, the overcharged electrode has superior electrochemical reversibility over time (χ_{rev}), which correlates to literature reports that α/γ-NiO_xH_y redox pair has higher charge/discharge capacities and better electrochemical performance.[26] These factors may support a possible hypothesis that the benefits of overcharging of the Ni (oxy)hydroxide material and conversion to the favorable γ-NiO_xH_y only occur while the material is overcharged at a potential lower than that required to drive OER. However, this hypothesis does not account for the ongoing shift of the redox peak positions more anodic during the chronoamperometry.

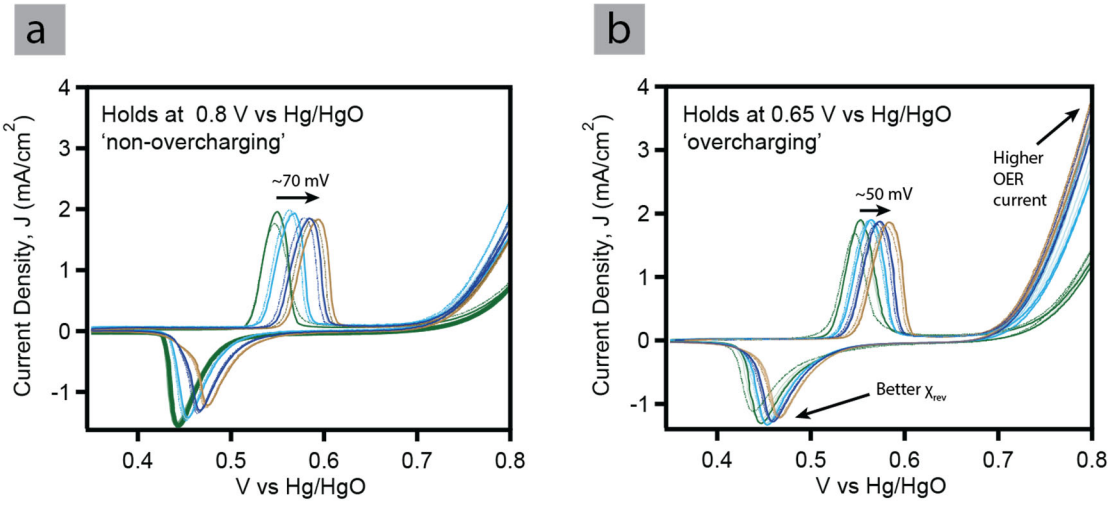

Figure 3.6. Cyclic voltammetry on two different NiO_xH_y electrodes, where 5 CV cycles were collected every 2 hours chronoamperometry at (a) 0.80 V vs Hg/HgO (b) 0.65 V vs Hg/HgO. Initial cycle (green), after 2 hours (teal), after 4 hours (blue), and after 6 hours (gold).

The shifting redox peak do appear to occur to a far lesser degree in (b, overcharged) compared to (a, non-overcharged). While the exact nature of the continuing shifting redox peak positions remains unclear, the differences in reversibility (χ_{rev}) and maximum OER current densities suggests that 'overcharging' at potentials less than that required to drive OER has benefits compared to holding potentials where OER is occurring. Thus, we propose holding potentials such that OER occurs is not the 'overcharging' regime of the traditional Bode cycle.

Regarding the potential of trace-Fe incorporation as the cause of the improved performance: improvements in (b) are not due to trace Fe-enhancements. Electrodes benefiting from Fe-enhancements will have clear, significant, and recognizable enhancement character, even extremely trace amounts (Fig. A.4).

Conclusions and bridge

This chapter studied the long-term stability and charge regeneration of the $Ni(OH)_2$/NiOOH catalyst when Fe-enhancement is not present. There is a direct correlation between degree of CV cycling and OER activity, where excessive cycling is detrimental to the catalyst. The minimal cycling is hypothesized to be beneficial due to a more porous material obtained as a result of divergent Ostwald ripening pathways for minimal cycling and highly cycled films. We further hypothesize that higher cycling forms a more interconnected and less porous material, regardless of the overall conversion from the α/γ to β/β redox pair over time. Additionally, the regenerative property of the $Ni(OH)_2$/NiOOH catalyst in the absence of Fe was investigated. The minimally cycled films showed clear regeneration and a high degree of electrochemical

reversibility. On the other hand, the highly cycled material was not able to regenerate as efficiently and had significant loss in electrochemical reversibility.

These results are evidence that there are additional factors existent than previous reports of regeneration have encapsulated. Previous work by Markovic and coworkers examined the regeneration of the $Ni(Fe)O_xH_y$ catalyst due to Fe incorporation cycling during operation.[33] While the impact of dynamic Fe is not in dispute here, the work presented here indicates the NiO_xH_y lattice, when Fe is not present, undergoes transformations that aid regeneration of the catalyst. The following chapter investigates these factors when the Fe-enhancement is present, and assessing Fe-dynamics occurring during degradation.

CHAPTER IV

CHARACTERIZATION OF IRON INCORPORATION IN NICKEL (OXY)HYDROXIDE DURING PROLONGED CATALYSIS FOR THE OXYGEN EVOLUTION REACTION

Chapter IV contains fully unpublished material. Prof. Boettcher and I conceived of the project. I performed and directed experiments, collected data, and analyzed data, as well as directed experiments that were conducted by several undergraduates. The content and analysis of this chapter was written by me with editorial assistance from Prof. Boettcher.

Introduction

Ni(Fe)-based oxides/(oxy)hydroxides, are presently known as the most-active OER catalysts in alkaline electrolyte and have been a focus of numerous investigations by various groups.[30] Many approaches have been employed to explore a variety of Ni(Fe)-based OER catalysis strategies, including thin-films, nanoparticles, layered double hydroxides, mixed metal-Ni-oxide/carbon foams, thin Ni oxide nanosheet wafers, rock-salt-like Ni/Co oxide nanocrystals, metal-doped Ni oxide on gold supports, and many others not specifically named here.[37,48–55] In addition to these approaches utilizing the preeminent $NiFeO_xH_y$ catalyst, deep investigations of this leading catalyst have recently focused on **active-site identification** and **catalytic mechanisms**.

Iron incorporates readily into $Ni(OH)_2$/NiOOH films, and this Fe incorporation is necessary to achieve paramount catalytic activity for oxygen evolution reaction (OER) in alkaline media.[19,37] Technological advances in operando characterization techniques and

computational chemical modeling using density functional theory (DFT) have given way to research attempting to settle the debate over the oxidation state and precise role of the Fe in the system. Advanced techniques such as operando XAS paired with DFT calculations were used by Friebel et al. to report M-O bond length changes and support the hypothesis that Fe^{3+} is the predominant Fe oxidation state and is the active site for the OER catalysis.[56] Results from XAS and EELS done by Nocera and coworkers also support Fe^{3+} as predominant, however, asserted the active sites to be Ni^{4+} promoted by Fe^{3+}.[57] Similarly, Strasser et al used XAS and DEMS and reported consistent oxidation of Ni (≥+3 state) with no evidence of Fe^{4+}. Their work suggests a Ni active site with necessary synergistic relationship between Ni-Fe.[58,59] Conversely, Stahl and coworkers investigated Fe in $NiFeO_xH_y$ catalysis using Mössbauer spectroscopy and found presence of Fe^{4+}.[60] Consistent with these findings, Gray and coworkers used in situ spectroscopic measurements and non-aqueous media to reveal the presence of high-valent (Fe^{6+}) species and supporting the hypothesis of highly oxidized Fe as the active site.[61]

Gray et al. reviewed the state of knowledge in these above-mentioned, and other, works and supports the hypothesis that Fe is the active site.[31] Correspondingly and simultaneously, operando XAS by Boettcher et al. shows Fe oxidation is occurring concurrent with OER for Co(Fe) oxide catalysts (which have long been used as a close electronic and structural analog for the $NiFeO_xH_y$ system). These results conclude that Fe plays a key role in the catalysis, and supports different mechanisms for OER with and without the presence of Fe.[62] Despite a decade of focused work towards unraveling the enigma of the $NiFeO_xH_y$ OER catalyst, some disagreements remain regarding the predominate oxidations states, identification of the catalytic active site, and mechanism

for OER catalyzed by $NiFeO_xH_y$. Yet, regardless of existing unanswered questions and some disparate hypotheses surrounding $NiFeO_xH_y$, there is one unassailable factor surfaced in the past decade: there is an essential synergy between Ni and Fe that is the cause of the optimal OER activity of the $NiFeO_xH_y$ electrocatalyst.

Despite rapid advances in the field understanding *catalytic activity and mechanisms*, there has been little progress understanding **the fate, dynamics, and stability of Fe** in the of $Ni(Fe)O_xH_y$ during prolonged OER.[32,33,63] It is important to understand the fate of Fe within the Ni(Fe) oxide structure over prolonged applied potentials performing OER with high current densities. Characterizing the stability, dynamics, and effects of prolonged operation on Fe in $Ni(Fe)O_xH_y$ may be an important piece in the story of the role of Fe in this high-activity catalyst.

The importance of benchmarking and reporting the activity-stability relationship of OER catalysts has been discussed by Chorkendorff and coworkers.[64] However, a full battery of experiments and investigations into the $Ni(Fe)O_xH_y$ activity-stability is still needed. Markovic et al. have recently published a close examination of short-term dynamics of Fe active sites in the $Ni(Fe)O_xH_y$ system, reporting remarkable 'dynamic stability' by balancing Fe dissolution and re-deposition within the $Ni(Fe)O_xH_y$ host.[33] This work brings to light short-term dynamics on a fresh $Ni(OH)_2$ host, yet, it leaves unanswered questions about the fate of Fe in aged $Ni(OH)_2$ and in a system structurally evolving under prolonged applied potential. For instance, earlier work done by Bell et al. reports unique changes to the catalyst structure after prolonged Fe-impurity aging not observed in Fe-free aging. They theorize that Fe impurities are substituted into the $Ni(OH)_2$ lattice forming NiFe layered double hydroxide (LDH) and potentially

converting into Fe-rich phases as Fe content increases.[45] Clearly there is evidence that prolonged aging alone impacts the structure of the catalyst, and will undoubtedly impact the structure-function relationship. Boettcher and coworkers hypothesized that two different Fe factors are at play in the unique OER activity of $Ni(Fe)O_xH_y$, where edge and defect Fe are responsible for enhancement of OER activity, while Fe in the bulk effects the Ni charge/discharge modulation seen in the voltammetry.[35]

While studies such as these report on changes in catalytic activity after *aging* or short-term exposure of NiO_xH_y to Fe sources, there are insufficient reports under prolonged (>1 hour) *operating conditions* with substantial current densities (>30 mA/cm^2). Conceivable degradation mechanisms for this water oxidation catalyst could proceed via Fe-cycling in the system and/or a detrimental restructuring of the $Ni(OH)_2$/NiOOH lattice. Characterizing and understanding the fate of Fe in the $Ni(Fe)O_xH_y$ catalysts is an essential step towards making use of this high activity catalyst for practical water-splitting and electrolysis devices. Rational design within the OER catalysis field requires the knowledge of this Fe-Ni synergy not merely on a short time scale relevant to laboratory investigations of chemical mechanisms, but also of prolonged operation under conditions with high current density.

Here, we characterize the changes in stability and performance of $Ne(Fe)O_xH_y$ operating at high current densities (>50 mA/cm^2) for prolonged periods of time (4-48 hours) using cyclic voltammetry (CV) and chronoamperometry. These results are coupled with quantification of Ni and Fe content and characterize the changes to the Fe% throughout the lifetime of the system using inductively coupled plasma mass spectrometry (ICP-MS). The electrodes are characterized at different stages within the

charge-overcharge-discharge cycles to elucidate the fate of the essential Fe sites during throughout the electrode lifetime.

Our results herein show that Fe-uptake is dependent on the oxidation state of the NiO_xH_y material. When NiO_xH_y is aged or subjected to cyclic voltammetry cycling it can incorporate maximum levels of Fe (up to ~22-25%). However, if the NiO_xH_y is exclusively held in the NiOOH species (performing OER) the material only uptakes and/or adsorbs ~10-15%. Our results further show that while there may be dynamic cycling and leaching of Fe during operation, leaching does not appear to be complete and up to ~10-15% will be retained in the material and is likely not the primary mode for any degradation of the overall OER activity of the material. We show here that stability of prolonged OER operation depends vitally on the presence of Fe^{3+} in solution, regardless of the degree of Fe present in the $Ni(Fe)O_xH_y$. This is an extension of the current state of knowledge merely acknowledging Fe in solution is required for high activity. These results elucidate the activity-stability relationship of the $Ni(Fe)O_xH_y$ catalyst and can help answer outstanding questions about the fate of Fe during prolonged OER operation. Understanding the role of Fe in the catalyst failure mechanisms is essential to future mechanistic and design studies for improved catalysts.

Experimental

Electrochemical analysis and characterization. Cyclic voltammetry (CV) and steady-state chronoamperometry (CA) measurements were recorded using a BioLogic SP200 or SP300 potentiostat in a Nalgene® three-electrode cell with a Pt-wire counter electrode, Hg/HgO (CH Instruments) reference electrode. CV for characterization of electrochemical catalyst deposition was performed with a scan rate of 10 mV s^{-1}, and CV

for electrochemical experiments was performed with a scan rate of 20 mV s^{-1}. CA for prolonged operation experiments was performed using an applied potential of 1.5 V vs Hg/HgO (*convert to RHE*) producing current densities between 50-100 mA cm^{-2}.

Electrochemical catalyst deposition and characterization. Electrodeposited NiO_xH_y films were deposited onto clean Pt foil electrodes from a 0.1 M $Ni(NO_3)_2$ solution. Depositions were performed in a glass cell using a two-electrode set-up with a home-made carbon cloth (Fuel Cell Earth) counter electrode by applying -0.1 mA cm^{-2} for 120 seconds. Using constant current and normalizing according to the variable surface area of the hand-made Pt foil electrode substrates produced electrodes with fairly consistent current densities (~3 ug/cm^2), but with slight variable absolute catalyst loading (between 400-1000 ng). Immediately following the deposition the electrodes were electrochemically characterized by performing cyclic voltammetry in 0.1 M KOH (semiconductor grade 99.99% trace metal basis) which was rigorously cleaned of Fe impurities using a high-purity $Ni(OH)_2$ Fe-absorbent followed by filtration using a 0.1 μm Supor (polyethersulfone) membrane syringe filters (VWR, Pall Acrodisc®) to remove remaining $Ni(Fe)O_xH_y$ particulates.[37]

Elemental quantification analysis. Quantification of Ni and Fe was performed using inductively coupled plasma mass spectrometry (ICP-MS). An iCAP™ Qs ICP-MS (Thermo Scientific™, Bremen, Germany) was used for offline analysis using an ASX-500 autosampler (Agilent, Waldbronn, Germany). The ICP-MS was operated in the hot plasma mode with a Ar cooling gas rate of 14 L/min and auxiliary Ar gas flow of 0.8 L/min. Samples were introduced with the equipped self-aspirating PFA 100 MicroFlow nebulizer (ESI, Omaha, USA), a cooled quartz spray chamber (2.7 degrees Celsius), and

a nebulizer Ar gas flow of 0.970 L min^{-1}. Dwell time for analysis was set to 1000 ms per peak and 5 sweeps. Signals were recorded for ^{60}Ni, ^{57}Fe, and ^{45}Sc, with Sc serving as an internal standard. New 15mL disposable polypropylene centrifuge tubes were used for all standards and samples. Multi-element standards were prepared at concentrations of 10, 25, 50, 100, and 300 ppb gravimetrically by adding appropriate quantity of stock solution (Millipore Sigma 1000 ppm elemental standards) and Trace-Metal grade 10% HNO_3. Trace-Metal grade 10% HNO_3 was used for the blanks and for the system rinse solution. Percent Fe content was calculated as Fe/(Fe+Ni), scaled with the internal standard in all samples. Error analysis and propagation was calculated from the standard deviation in the method (collection) (Table B.1). Uncertainties associated with concentration of the standard solutions and sample dilution were not included as they are commonly insignificant compared to the instrument method precision.[65,66]

Results and Discussion

Fe incorporation reaches a maximum threshold with increasing cyclic voltammetry and does not affect stability. Cyclic voltammetry was performed in 0.1 ppm Fe-spiked 0.1 M KOH where the increasing number of cycles increased the Fe-incorporation into the Ni oxide until a threshold of ~22-25% Fe is reached (Figure 4.1, Figure B.1). This threshold is reached after approximately 100 cycles, regardless of catalyst loading (Figure B.1). This is consistent with maximum Fe uptake levels for the Ni oxide reported elsewhere in the literature.[33,35,45,56,67]

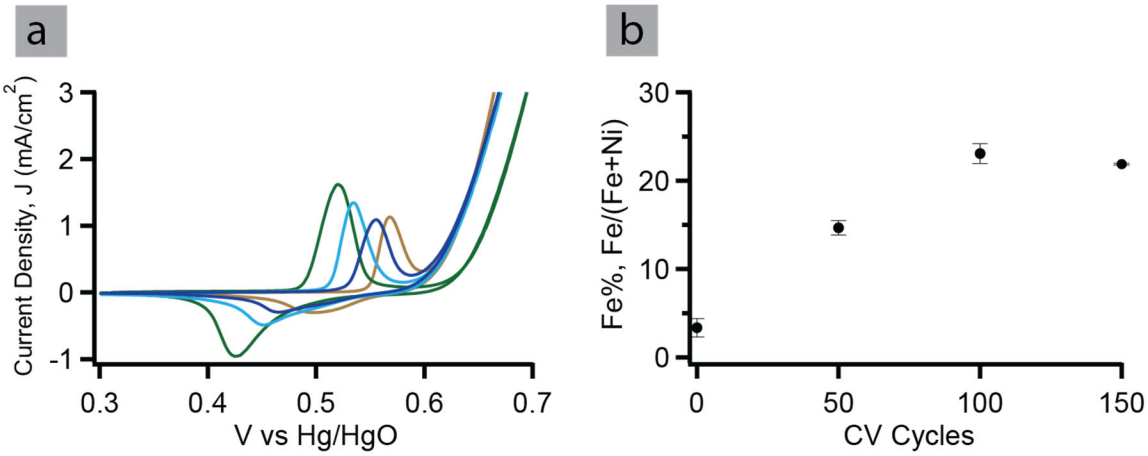

Figure 4.1 (a) Cyclic voltammetry demonstrating anodic shifts in redox peak positions. After 2 CV cycles (green), after 50 CV cycles (teal), 100 CV cycles (blue), 150 CV cycles (gold). (b) Fe content determined by ICP-MS for Fe/(Fe+Ni) as a function of increasing CV cycling.

The OER onset improves by ~50mV over potential after only 50 cycles of cyclic voltammetry, with ~15% Fe (Figure 4.1a). The overpotential required for OER does not continue to improve with increase in Fe incorporation. These results indicate that the initial Fe adsorption at the surface is the primary mode for Fe-enhancement of OER activity. Over time, and more cycling, Fe incorporates more homogeneously until the maximum incorporation level is reached. These bulk incorporated Fe do not have an impact on the Fe-enhancement of OER activity. This hypothesis is in agreement with widely-held theories that the increase in OER activity of the $Ni(Fe)O_xH_y$ upon Fe incorporation depends on the local structure (surface adsorbed and bound Fe), and not on the bulk properties (bulk incorporation of Fe throughout the lattice).[32,34,35]

However, the increase in Fe incorporation with increasing cyclic voltammetry has an irrefutable impact on the $Ni(Fe)O_xH_y$ structure; the redox waves of the $Ni(OH)_2$/NiOOH shift anodic with increasing cycles and increasing Fe uptake (Figure 4.1a). The anodic shift and decrease in peak integration of the waves lessens as Fe uptake reaches its maximum. This is consistent with reports that Fe incorporation

causes shifts in the Ni oxide redox peak positions.[45,68] It is important to note that even in *rigorously Fe-free electrolyte* there will be slight shifts in the redox peak positions due to continuous phase transitions of the NiO_xH_y structure; this phenomenon is clearly reported in Chapter III of this dissertation, as well as corroborated by work done by Bell and coworkers.[45] According to the Bode cycle and published electrochemical data, the α/γ redox waves are more cathodic than the β/β structures (Figure 2.3).[12,19]

Work done by Wu et al. concluded that even trace amounts of Fe on thin-layer Ni oxide favors the β-NiOOH structure (the β/β couple).[32] In agreement with Wu et al. and with the Bode cycle characterization[15,69] of β/β redox positions, here, our observed shifts in the redox peaks to a more positive potential and decrease in peak integration are hypothesized to be correlated with the formation of β-NiOOH structure, facilitated and expedited by the inclusion of Fe in the lattice.

In Chapter III we investigated how changes in phase and morphology of Fe-free NiO_xH_y impact stability and long term electrochemical behavior. Work by Bell et al. reported prolonged aging in Fe-containing electrolyte causes substitution of Fe impurities into the $Ni(OH)_2$ lattice, and that there are **unique catalyst structural changes after prolonged Fe-impurity aging not present in Fe-free aging**.[45] Further, Boettcher et al. studied the surface morphology via atomic force microscopy (AFM). They reported increases in effective surface volume with CV cycling in Fe-free electrolyte up until ~200 CV cycles with a fairly linear trend. After Fe was spiked into solution the effective surface volume increased significantly > 25%.[67] Thus, it seems prudent to examine the $Ni(Fe)O_xH_y$ catalyst for structure–stability–activity in a similar manner than was done for the pristine NiO_xH_y material.

Electrodes were exposed/cycled in Fe^{3+} spiked electrolyte to different degrees (Fig. 4.1b and Fig. B.1). Electrodes briefly exposed (brief soak on the order of one minute) to the Fe^{3+} source result in Fe uptake between 5-10%. Electrodes cycled for 50 CV cycles prior to chronoamperometry result in Fe uptake between 15-18% Fe. Electrodes cycled for ≥ 100 CV cycles prior to chronoamperometry result in Fe uptake between 22-25%. Chronoamperometry at 1.0 V-iR vs Hg/HgO was performed on the electrodes

Any degree of pre-incorporation of Fe into electrodes operated in Fe^{3+}-spiked 0.1 M KOH produces reasonably stable OER current densities over 4-hours test. These results show that varying degrees of Fe incorporation has no impact on stability under the given conditions. The stability is consistent and not dependent on initial Fe uptake or CV cycling prior to chronoamperometry (Figure 4.2).

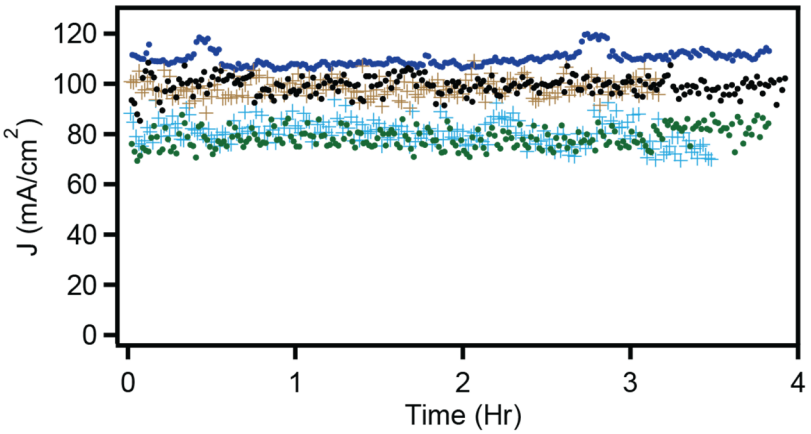

Figure 4.2. Chronoamperometry (CA) at 1.0-iR V vs Hg/HgO in 0.1 M KOH electrolyte spiked with 0.1ppm Fe^{3+}. With minimal exposure to Fe-spike KOH prior to CA with Fe% ~5-10% (black circles), 50 cycles of CV prior to CA, ~15% Fe (blue circle and green circle), 100 cycles of CV prior to chronoamperometry ~25% Fe (teal cross and gold cross).

Maximum Fe incorporation occurs only when $Ni(OH)_2$ is present. Maximum Fe incorporation is not achieved during prolonged OER operation in the NiOOH state. As discussed above, maximum Fe-uptake of ~22-25% into NiO_xH_y occurs after approximately 100 CV cycles. Fe-uptake is ~15% for electrodes cycled only 50 cycles (Figure B.1). Minimal exposure to Fe-spiked KOH leads to rapid Fe-incorporation of up to 10% Fe/Fe+Ni. Chronoamperometry at 1.0 V-iR vs Hg/HgO was performed on $Ni_{0.9}Fe_{0.1}O_xH_y$, $Ni_{0.85}Fe_{0.15}O_xH_y$, and $Ni_{0.8}Fe_{0.2}O_xH_y$ electrodes in identical 0.1ppm spiked 0.1 M KOH. Composition of Ni/Fe was achieved via Fe-uptake into pristine NiO_xH_y from Fe-spiked solution as described above (via controlled CVs). The impact of Fe-uptake is immediately and readily observed in the CV data as expected, as shown from cycle 1 to cycle 2 (Figure 4.3a, gold traces). Upon pristine deposition the OER activity is poor, with an onset at nearly 0.65 V vs Hg/HgO. However, after just one cycle in the Fe-spiked electrolyte the OER onset improves by ~500 mV. There is no continued improvement as the electrode is cycled and more Fe is incorporated. After the electrode has been cycled 50 times the Fe incorporation is **only ~15% and is lower than the maximum** (Fig. 4.3a, green trace). Chronoamperometry was immediately performed with no changes to the cell or electrolyte. There is **no significant increase in Fe-uptake during the CA (Figure 4.3b)**. The change in Fe% during CA is only ~1-4% increase regardless of the duration of the CA. If NiOOH was able to uptake Fe to the same degree that $Ni(OH)_2$ can, we would expect an increase in the Fe content up to the maximum of ~22-25%. While the catalyst is held in the NiOOH phase, it does not uptake Fe in the same manner as the $Ni(OH)_2$ species. One characterizing CV was collected post 10-h CA to determine the extent of changes to the (i) redox peak positions and (ii) OER onset (Fig.

4.3a, teal trace), The pre-CA and post-CA cyclic voltammetry character is nearly identical.

Similarly, an electrode was cycled 50 times (~15-18% Fe) and CA was performed for up to 10 hours (Fig. 4.3a, blue trace). Even after 10 hours of operation, the Fe-incorporation does not reach the maximum level. The post-operation ICP-MS indicates the Fe% stays at ~18% regardless of the duration of CA. Care was taken to remove the electrodes from the Fe-containing electrolyte during operation, to capture the Fe content present while the material was in the NiOOH phase. Any degree of exposure to the Fe-spiked KOH in a resting state of $Ni(OH)_2$ will cause additional Fe-uptake.

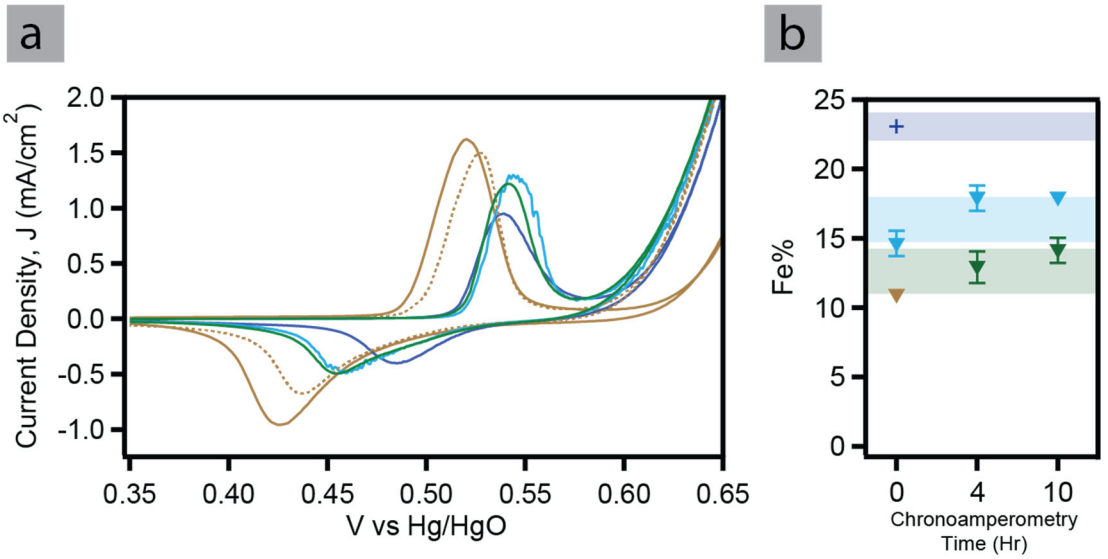

Figure 4.3. (a) Cyclic voltammetry on a pristine NiO_xH_y electrode in Fe-free 0.1 M KOH (gold trace). Electrode was placed in 0.1 ppm Fe-spiked KOH and one CV was collected (gold dotted trace); there is immediate Fe-uptake to ~10%. Electrode cycled for 50 CVs has anodic shift in redox peaks (green trace) and increase in Fe content to 15%. CA for 4-hours was performed on the 50 CV cycled electrode at 1.0-iR vs Hg/HgO with one characterizing CV collected post CA (teal trace). There is no change in CV character and only a ~2-4% change in Fe content, still well below maximum. CA was performed on another CV cycled electrode for 10-hours with one characterizing CV collected post CA (blue trace). There is minimal change in CV character and only a ~2-4% change in Fe content, still well below maximum. (b) Fe content of $Ni(Fe)O_xH_y$ after varying duration of chronoamperometry, indicating Fe% for only 1 cycle (gold) and, no CVs pre-CA (green), 50 CVs pre-CA (teal), and 100 CVs indicating maximum Fe uptake possible (blue).

This may seem to indicate that the NiO_xH_y only uptakes Fe during the $Ni(OH)_2$ phase and during cyclic voltammetry. However, further experiments revealed that NiOOH does also uptake Fe but differently than $Ni(OH)_2$. Chronoamperometry at 1.0 V-iR vs Hg/HgO was performed on pristine NiO_xH_y electrodes in rigorously Fe-free conditions (methods for preparation reported in Chapter III). After the electrodes were operated for ~1-hour in Fe-free conditions (Fig. 4.4a, light green), 0.1 ppm Fe^{3+} was spiked into solution in situ (Fig. 4.4a, dark green). Pre-spike, the electrodes were operating at ~30-40 mA/cm^2 at 1.0V-iR vs Hg/HgO which is consistent with NiO_xH_y activity with no Fe incorporation. The current response improves immediately upon Fe spike, doubling the current density.

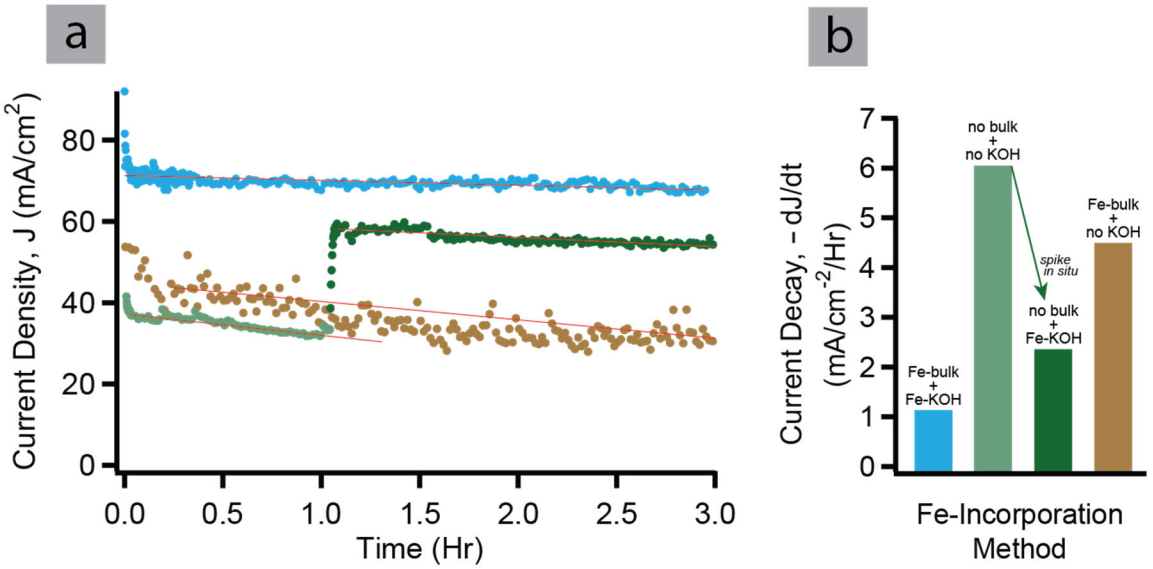

Figure 4.4. Chronoamperometry at 1.0V-iR vs Hg/HgO on a pristine NiO_xH_y electrode in originally rigorously Fe-free 0.1 M KOH (light green). Fe-spike of 0.1 ppm Fe^{3+} was added in situ after 1-hour of operation (dark green). The significant increase in current density is due to Fe-uptake, measured by ICP-MS to be 9%. $Ni(Fe)O_xH_y$ electrode with ~15% Fe operated in Fe-free KOH (gold). The stable and high current density $Ni(Fe)O_xH_y$ operated in Fe-spiked 0.1 M KOH is shown for reference (teal). (b) Rates of degradation of OER current over time as a function of method of Fe incorporation.

Post-operation ICP-MS was performed on all electrodes tested in this manner, and were determined to have between 5-10% Fe incorporation (Fe/Ni-Fe). This is consistent with the minimum values measured for electrodes exposed only briefly to Fe-spiked KOH and is evidence that the NiOOH phase in fact does uptake and/or adsorb Fe, however, to a far less degree than the $Ni(OH)_2$ phase. None of the electrodes tested contained more than 10% Fe (10 hours tested).

This electrode was initially Fe-free, then spiked in-situ with Fe^{3+} in solution. We also tested a $Ni(Fe)O_xH_y$ electrode in Fe-free electrolyte. Electrodes were cycled 50 times in 0.1 ppm Fe^{3+} was spiked 0.1 M KOH which generally produces a catalyst with ~15% Fe. Electrodes were placed in rigorously Fe-free KOH and chronoamperometry at 1.0 V-iR vs Hg/HgO was performed for 4 hours (Fig. 4.4, gold). Interestingly, the current density immediately drops to the levels of the Fe-free electrode (Fig. 4.4, green). This prolonged activity and stability is consistent with the Fe-free catalyst. However, analysis via ICP-MS revealed the electrode still contained 13% Fe (Fe/Fe+Ni). Thus, despite there being Fe incorporated in the catalyst, the lack of solution-Fe results in activity levels that are as low as when there is no Fe present at all. These experiments support the hypotheses that the performance *and stability* is not determined by bulk Fe, but by more loosely bound surface Fe. The solution Fe is vitally important for the $Ni(Fe)O_xH_y$ system.

These results are in close agreement with work done by Halaoui and coworkers, wherein they used electrochemical methods to also conclude that regardless of Fe-content in the electrode, the in-solution Fe is required for the high-activity of the catalyst.[63] Their work does hypothesize that bulk-Fe may be leached out but will redeposit in active surface sites if solution-Fe is present in sufficient concentrations. The perspective of

leaching and redeposition of Fe strongly agrees with work by Markovic et al. claiming the stability of $Ni(Fe)O_xH_y$ is due to the dynamic dissolution and redeposition at the surface sites.[33] Our results identifying incomplete/fractional Fe-leaching are consistent with similar work done by Boettcher et al. on the analogous $Co(Fe)O_xH_y$ concluding that Fe will leach out of $Co(Fe)O_xH_y$ when operated in Fe-free electrolyte.[34]

Further, these results indicate that the solution-Fe is not only necessary for high OER activity, but also play a role in the stability of the catalyst. Figure 4.4b demonstrates the various rates of OER current decay as a function of method of Fe-incorporation. The stability of the catalyst with bulk-Fe and with Fe^{3+} available in solution performs with the best stability, only with a -1 mA cm^{-2}/Hr degradation rate. On the other hand, a rigorously Fe-free electrode in Fe-free KOH has the highest rate of degradation at nearly -6 mA cm^{-2}/Hr. Simply spiking Fe^{3+} into the solution in situ dramatically increases not just the OER performance, but the stability as well. The solution-Fe improved the degradation to only -2.3 mA cm^{-2}/Hr. Finally, the electrode with intentional Fe incorporation via cycling for 50 cycles in a Fe-spiked solution was transferred to a rigorously Fe-free cell with Fe-free KOH. Despite the presence of bulk-Fe and no substantial loss of said Fe during operation (discussed above), the rate of degradation is nearly as high as a fully Fe-free electrode, degrading at -4.4 mA cm^{-2}/Hr. Several repeat experiments corroborate these results. Our work not only is in agreement with the recent works from Markovic et al.[33], Halaoui et al.[63], and He et al.[32] regarding the necessity of solution-Fe for high activity of $Ni(Fe)O_xH_y$, we also conclude it is vital for the long-term stability under high-current density operating conditions regardless of bulk Fe-incorporation.

Catalyst activity loss is dependent on pH of electrolyte. The various current studies on $Ni(Fe)O_xH_y$ generally have disparate experimental conditions, especially in terms of electrolyte. The Markovic, et al. work on dynamic Fe-sites and stability based on Fe dissolution/redeposition reported results for only 0.1 M KOH.[33] The He and coworkers recent work reported their electrochemical characterizations specifically for 12.88 pH.[32] On the other hand, Halaoui et al. presented results only for 1.0 M KOH.[63] To further explore the prolonged stability of $Ni(Fe)O_xH_y$ we performed experiments in 1.0 M KOH that complement the results set forth herein for the 0.1 M regime. Prolonged chronoamperometry experiments performed above were repeated in 1.0 M KOH spiked with 0.1ppm Fe^{3+}. Cyclic voltammetry was performed on each electrode for 50 cycles, then prolonged chronoamperometry was performed at 0.75 V vs Hg/HgO (~430 mV overpotential). The data shows a steady and consistent degradation of catalytic activity (Figure 4.5). Regardless of the maximum current density achieved by the electrode (varies slightly based on differences in catalyst loading), the rate of degradation of current (dJ/dt, mA cm^{-2}/Hr) is consistent at about -2 mA cm^{-2}/Hr. Figure 4.5b shows that the redox state of each of the electrodes tested before prolonged CA were essentially identical. The slight differences in peak integration and max current densities are from minor differences in catalyst loading and electrode surface area.

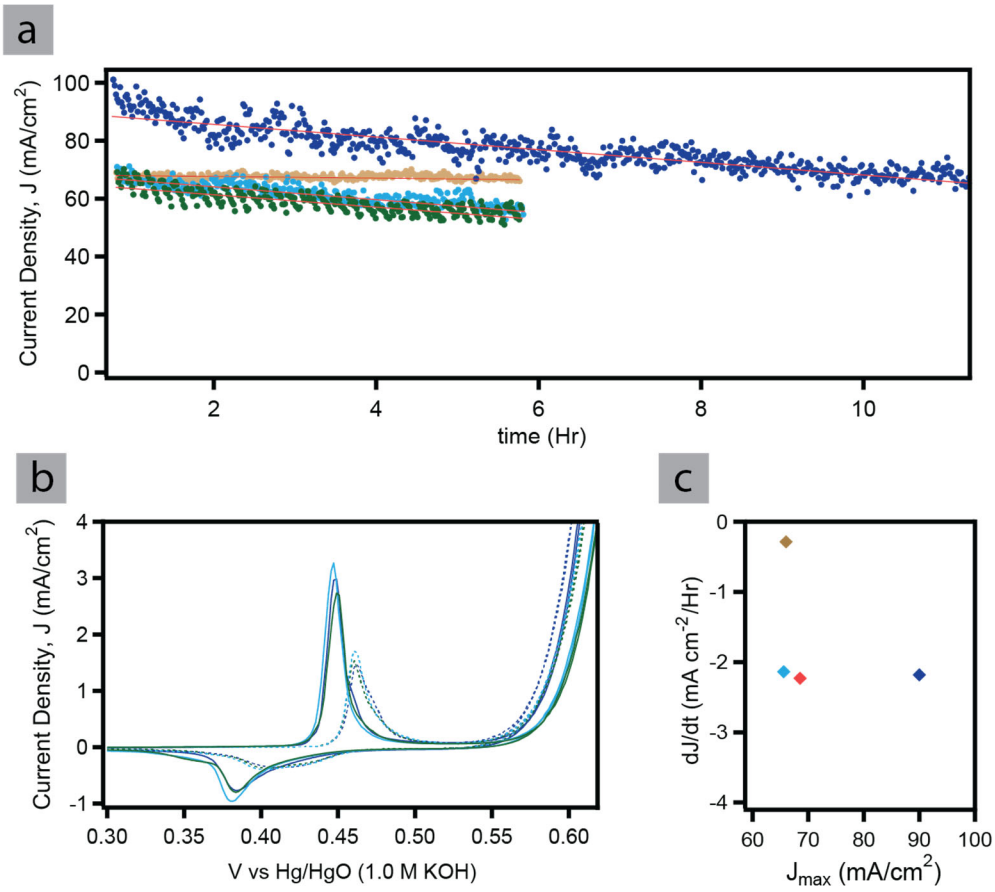

Figure 4.5. (a) Chronoamperometry for Ni(Fe)O_xH_y electrodes run in at 0.75 V vs Hg/HgO in 1.0 M KOH with 0.1ppm Fe^{3+} spike. Gold trace is Ni(Fe)O_xH_y run in 0.1 M KOH (1.5 V vs Hg/HgO) for comparison of stability in pH 13 versus degradation in pH 14. Red lines are linear fits. (b) Cyclic voltammetry of initial CV cycle (solid color curves) and cycle 50 (dashed color curves) in 1.0 M KOH with 0.1ppm Fe^{3+} immediately preceding CA. (c) Rates of degradation of OER current over time as a function of maximum initial current density. Degradation is consistent for all 1.0 M KOH electrodes. Gold mark is in 0.1 M KOH for comparison of stability.

One presumption one might make is that the loss in OER current is merely loss of catalyst and catalyst dissolution. However, a comparison of the integrated oxidation peak from the pristine catalyst with Ni measured from ICP-MS provides a ratio of 1.75 ± 0.11 (Figure 4.6).

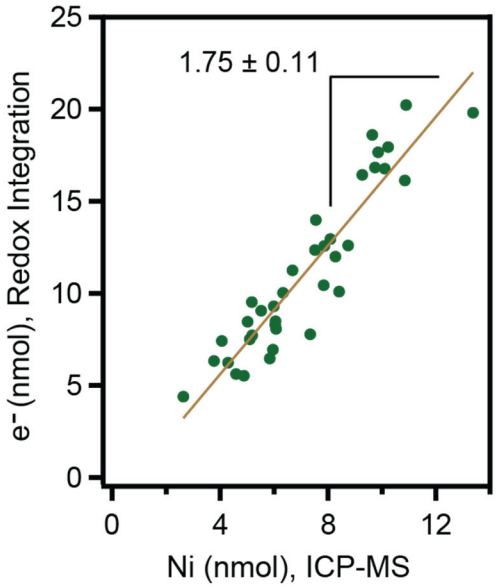

Figure 4.6. Comparison of redox wave integration (oxidation wave) and ICP-MS for determined Ni loading of electrodes. Data collected from 37 different electrodes (green) and fit to a linear equation (gold line). Moles of e^- are from CV integration as a function of moles of Ni via ICP-MS analysis from digestion of electrodes.

This 1.75 e-/Ni electrochemical activity is consistent with literature reports of expected e-/Ni for a film thickness in our range (on the order of 10 nm, with the typical thickness of our films between 10-30 nm).[70,71] There is no apparent evidence of loss of catalyst for the films reported here such that one would expect such significant loss in current density over 10 hours (30 mA/cm^2 loss, Fig. 4.5a).

Accordingly, since fatal dissolution isn't likely, there isn't a clear explanation in the data for the pH dependence of degradation. A probable answer to this question could be that the structure of the Ni(Fe)O_xH_y progresses through the Bode phase cycle changes more rapidly. The solubility of the various Ni species is higher with increasing pH (reported most readily for Ni^{2+} species)[40,72]. While this doesn't appear to lead to significant dissolution (loss without redeposition) within the 10 hours tested, it may facilitate phase transformations more easily. Chapter III of this dissertation proposed that

regardless of electrochemical treatment, the α/γ-NiO_xH_y will ultimately transform to the more thermodynamically stable β/β-NiO_xH_y. The pH dependence seen in this work here could likely be this α/γ conversion to β/β expedited due to slightly higher solubility in the higher alkaline environment.

It is important to study degradation and activity-stability under prolonged operation conditions. Several sources in the recent years have reported 'stability' of the Ni(Fe)O_xH_y catalyst; however, these works examine the catalyst in low current density and short-duration operation regimes.[32,33,73] In a short-duration experiment (~1 hour) there is insufficient data to determine the degree and rate of degradation of catalytic activity. Figure 4.7 illustrates this point where the same data is shown in panel (a) and panel (b): Ni(Fe)O_xH_y catalyst run in the 0.1 M KOH demonstrates fairly stable catalytic activity for the 5 hours tested where the sample run in 1.0 M KOH demonstrates degrading catalytic activity with a stable rate of degradation of -2 mA cm^{-2}/hr. If these electrodes were run for only 1 hour each, they appear to have identical stable behavior. Further, at high current densities there may be more noise in the data making the trend over time more difficult to assess; there is steady and high production of oxygen bubbles on the surface of the electrode which are continually growing and being pulled away into solution via vigorous stirring. Accordingly, in assessing, characterizing and making determination regarding the stability of the Ni(Fe) oxide catalysts, experiments should be run for prolonged periods permitting proper analysis of the activity-stability.

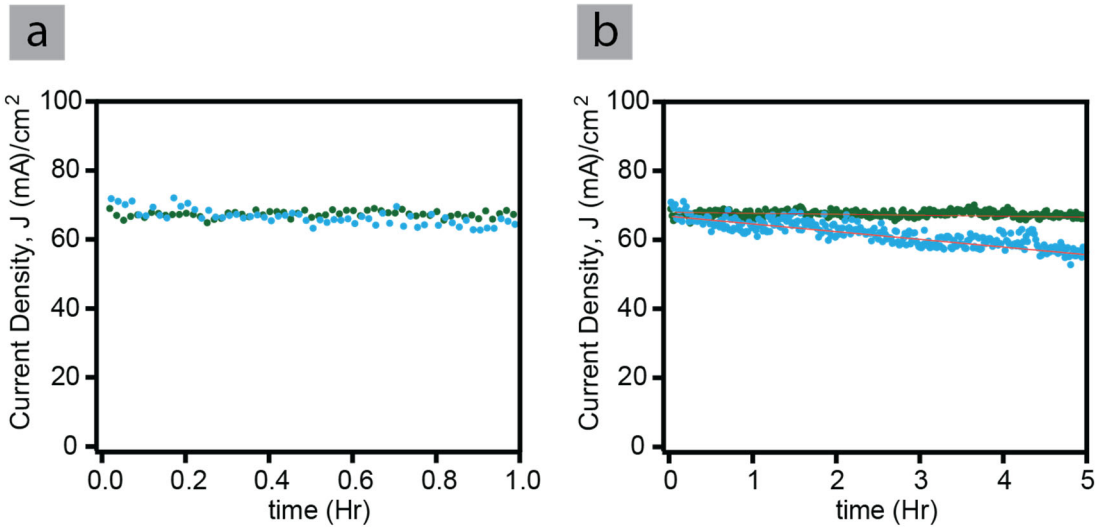

Figure. 4.7. Chronoamperometry data of Ni(Fe)O_xH_y catalyst run in 0.1 M KOH (green) and 1.0 M KOH (teal). (a) Data truncated to mimic an experiment limited to one-hour operation where data appears identically stable for pH 13 and pH 14. (b) Full data showing 5 hours of operation clearly characterizing the degradation of catalyst activity in the different pH electrolyte. Red traces are linear fits of the current decay.

Conclusion and bridge

In this work we studied the stability and activity of Ni(Fe)O_xH_y with conditions for prolonged high current density OER operation. We characterized a maximum Fe incorporation threshold of ~20-25% Fe occurs after cyclic voltammetry or aging, which is consistent with the current state of knowledge in the literature. We have shown that Fe-uptake is dependent on the oxidation state of the NiO_xH_y material, where the NiOOH species does uptake and/or adsorb Fe, but to a far less degree (only ~10-15%) than full incorporation possible via aging or CV cycling (up to ~22-25%).

Our results herein agree with the current state of knowledge that maximum incorporation of Fe is not necessary to obtain maximum OER activity in 0.1 M KOH. We have also shown that the source of Fe does have a definite impact on stability. Our work shows that even if there is Fe incorporated into the Ni(Fe)O_xH_y the prolonged operation

OER activity cannot be stable without Fe in solution. Even if there is Fe incorporated into the $Ni(Fe)O_xH_y$ the prolonged operation OER activity cannot be stable without Fe in solution. We have shown that this is not merely due to Fe leaching from the electrode, as $Ni(Fe)O_xH_y$ run in Fe-free electrolyte for up to 10 hours retain sufficient levels of Fe (~10%). We further investigated the impact of pH on the prolonged operation and found that with increasing pH there is an increase in current decay. We purport these results complement our results from Chapter III, wherein we identify a primary mode for degradation is the conversion from α/γ-redox pair to the β/β-redox pair. Here, we believe the pH factor expedites this process due to increases in the solubility at higher pH.

CHAPTER V

FABRICATION STRATEGIES FOR STABLE PHOTOANODES USING SILICON WITH NICKEL (OXY)HYDROXIDE CATALYST FOR SOLAR WATER SPLITTING

Chapter V contains fully unpublished material. Dr. Sebastian Oener and I conceived of the project with project feedback from Prof. Boettcher. I performed experiments, collected data, and analyzed data with help from Dr. Oener. The content and analysis of this chapter was written by me with editorial assistance from Prof. Boettcher.

Introduction

The previous chapters in this dissertation have been focused exclusively on the Ni (oxy)hydroxide catalyst used for the oxygen evolution half reaction of overall water splitting. Applications involving $Ni(OH)_2$/NiOOH as an OER catalyst may include more complex architectures, such as electrolysis involving membranes and photoelectrochemical cells with semiconductor interfaces. Thus, when considering practical applications using the high performing Ni-$Fe(OH)_2$ one must also consider the stability and corrosion of the multicomponent electrode for efficient incorporation. Photoelectrochemical (PEC) cells have the potential to be a promising solution for alternative renewable energy. PEC water splitting in particular offers a pathway to obtain renewable energy from sunlight by splitting water into hydrogen and oxygen gas, where the only by-product is water. The PEC cell uses a light absorbing semiconductor in connection with a chemical catalyst to drive the water splitting reaction.[7]

Research into the various materials that are suitable for OER, chiefly, metal oxides, semiconductors, sulfides, and III-V materials is ongoing.[74–76] As a model system this chapter will focus solely on silicon (Si). Silicon remains the most widely used material for many photovoltaic applications; Si is Earth-abundant, low cost, and has a band structure that is desirable for water splitting, with a narrow gap (E_g = ~ 1.1 eV) well aligned with the spectrum of solar energy.[77] However, Si, like many photoanodes, suffer from *two serious deficiencies*: passivation and dissolution. The former (passivation) occurs in aqueous solution below pH ~ 11. Si is quickly oxidized to the electrically insulating phase SiO_2(s). The latter (dissolution) occurs in alkaline solutions of with pH ~11 and higher, where Si etches, i.e. it converts into soluble SiO_3^{-2}(aq) and dissolves.[78] Accordingly, much of the research of Si photoanodes for water splitting has focused on strategies for stabilizing and protecting the surface.[79,80]

The general term of deactivation and degradation of a semiconductor in photovoltaics is corrosion. Corrosion of semiconductor materials is complex and can proceed through three distinct routes: chemical, photoelectrochemical, electrochemical. Chemical corrosion of a semiconductor denotes dissolution and/or oxidation of the material during exposure to the surrounding environment (the electrolyte). Electrochemical and photoelectrochemical corrosion both describe processes of degradation during net charge transfer via transfer of majority charge carriers and minority carriers respectively.[79] This work presents a novel fabrication scheme for *chemical protection* of Si photoanodes in highly alkaline conditions appropriate for OER.

Chemical protection – the conductivity/transparency trade-off

A traditional method for chemical protection of the semiconductor surface is deposition or growth of a protective layer. This creates a layer between the semiconductor and the electrolyte such that the electrolyte-induced dissolution and/or oxidation of the material cannot occur. These layers are often referred to as a protection layer. There are two important properties of protection layers that need be considered: **electrical conductivity** and **optical transparency**. Unfortunately, these characteristics are generally mutually exclusive (Fig. 5.1).

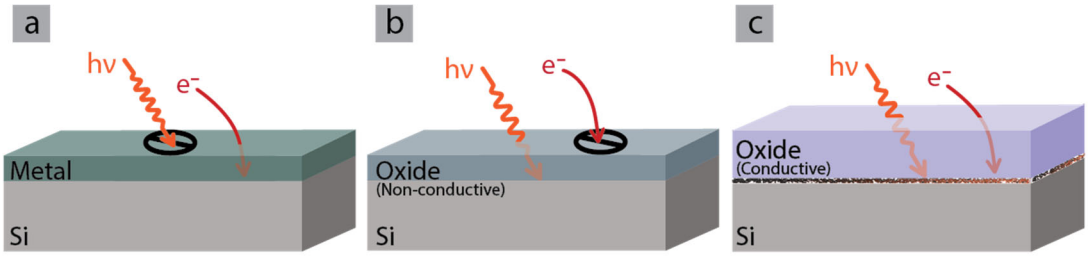

Figure 5.1. Three typical methods of protecting Si photoanodes, (a) thin metal films that conduct charge carriers, but block light, (b) non-conductive metal oxides that are optically transparent, but do not conduct charge carriers, and (c) conductive metal oxides that are optically transparent and conduct charge carriers, but aren't as chemically stable and can lead to photocorrosion.

Coating the surface with a thin-film of metal would provide the chemical protection and electrical conductivity required; noble metals such as platinum and palladium are stable even in the harshest alkaline environments where OER is most efficient. However, metal thin films are optically dense, blocking photon absorption by the underlying photoanode Si material. Thick metal-oxide layers (~100 nm) that have sufficient optical transparency have been used to protect Si. However, stable oxides are dielectrics and the electrical conductivity is insufficient, and conductive oxides are generally not stable in alkaline conditions. Further, reports in the literature show evidence that these structures are

susceptible to intrinsic light-dependent photo corrosion, bringing about a trade-off between the chemical and photocorrosion processes.[81] Non-conductive, yet optically transparent, thin films (< 2 nm) have been used as chemical protection of Si. Here, charge carriers can be extracted through the barrier via quantum mechanical tunneling. Due to the thinness required to extract the charge carriers, the chemical stability benefit is minimal, with reports of only ~100 hours of lifetime.[82,83] Consequently, continuing research into passivation of Si photoanodes is necessary.

There is no single chemical protection layer that can effectively protect the Si semiconductor from corrosion while maintaining high PEC functionality. Thus, using a combination of the best approaches is a promising method to obtain maximum chemical protection for PEC anodes. In this work, a transparent protective oxide layer is used for passivation of the bulk, permitting maximum photon absorption over the bulk of the surface, and metal micro-contacts are embedded to provide charge transport pathways through the electrically insulating oxide (Fig. 5.2).

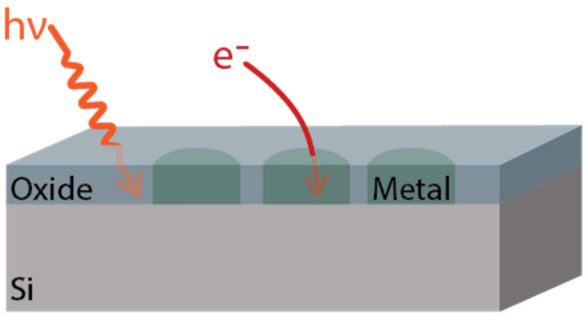

Figure 5.2. Illustration demonstrating the combination of optical transparency of a protective metal oxide layer with the electrical conductivity of embedded metal micro-contacts.

When considering which oxide material to use one should consider three important factors: (i) stability in both acidic and alkaline solutions (most particularly

alkaline), (ii) semiconductor surface defect passivation, and (iii) charge carrier selectivity at the semiconductor interface. No single material will maximize the benefits of each one of these three factors, thus a multi-layer structure is often employed with more than one material. In this work, a two-layer oxide structure is utilized. The first layer (passivation and selectivity) is directly in contact with the semiconductor surface; this layer needs to be optimized for surface defect passivation and charge carrier selectivity. The second layer (protection) need only be optimized for stability in the conditions of the electrolyte, which is outside of the scope of this work. This dissertation chapter *focuses exclusively on achieving optimal* ***chemical protection*** of the Si photoanode. The electrical passivation and selectivity would need to be improved upon for the fabrication techniques presented herein to have overall desirable PEC performance.

Methods and fabrication techniques

A fabrication scheme that produces a multi-layered photoanode with optimal physical and chemical stability is presented in this chapter. A detailed discussion justifying the decisions made in this fabrication scheme follows at the end of this methods section.

The overall fabrication has three primary phases (Figure 5.3). Phase A is the cleaning and preparation of the semiconductor substrate. This phase may also include the deposition of the electrical passivation layer if one is required for proper rectification of the semiconductor/contact interface. Phase B is the first lithograph process where the contacts are patterned in an array and deposited onto the substrate via thermal or electron beam depositions. Phase C is the second lithography and etching process. Here, the

chemical protection layer is deposited, applying another array pattern and etching the array pattern to expose the underlying-covered contacts.

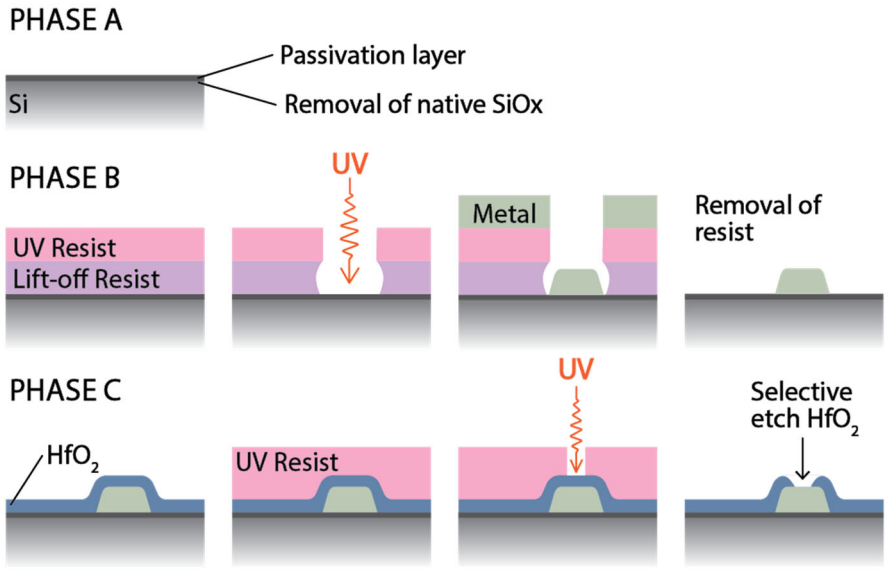

Figure 5.3. Multi-layered fabrication scheme for protection of photoanodes. Phase A is cleaning commercially available Si wafer, removal of the native oxide growth, and deposition of an electrical passivation layer. Phase B is implementation of the first layer of the lithography pattern, and deposition of the metal contacts. Phase C is the deposition of the chemical protection layer, implementation of the second layer of the lithography pattern, and etching the protection layer to expose the metal contacts.

Phase A. Cleaning and preparing the substrate

Commercially available n-Si wafers were cleaned in 100°C piranha solution (3:1 concentrated H_2SO_2 and H_2O_2) for 30 minutes to clean any trace organics from the surface. A thin native oxide layer (SiO_2) will always be present as pristine commercial Si have been gradually oxidizing in air. This oxide layer is not optimal for the semiconductor-metal interface, and thus it is removal of this layer immediately preceding the next step in the fabrication scheme. The native oxide (SiO_2) was removed by 2 minute etch in buffered HF (30:1). Freshly cleaned substrates were *immediately* used for the next fabrication step to prevent regrowth of the detrimental native oxide layer.

For electrodes where an electrical passivation layer was included a thin (~1 nm) layer of Al_2O_3 was used. Al_2O_3 has been used as an optimal material for passivation of both n- and p-Si semiconductor substrates.[84–86] Immediately after substrate cleaning, Al_2O_3 was deposited using low-temperature ALD (atomic layer deposition). ALD Al_2O_3 film was grown using a viscous-flow ALD reactor (Savannah G2 Thermal ALD, Veeco/Ultratech/Cambridge NanoTech). The chemical precursor used was $Al(CH_3)_3$ [trimethylaluminum (TMA)] (Akzo-Nobel, semiconductor grade, 99.9999%). Films were deposited at 75°C by 8-cycles of alternating TMA and H_2O flows with N_2 carrier flow gas. Under these conditions each cycle produces a Al_2O_3 layer of ~1.2 Å thickness. Thus, an 8 cycle procedure produced a ~9.6 Å Al_2O_3 film.[87] Recipe and specifications were provided by the manufacturer, Veeco/Ultratech/Cambridge NanoTech.

Phase B. Conductive contact points

Phase B of the fabrication scheme is the deposition of the micro-contact array. This is achieved via a double layer optical resist technique. Optical lithography is a technique where a light-sensitive polymer (the photoresist) is deposited onto a substrate and exposed to UV light to form relief patterns in the substrate.[88] Generally, the photoresist is spin-coated atop the substrate and then directly patterned: a simple two-step procedure. However, undesirable side-wall formations can occur when the subsequent layer is a film deposited via evaporation or sputtering (Fig. 5.4a). Side-wall formations (a crowning effect) can be prevented by imposing intentional undercutting of the polymer mask. This is difficult to achieve with the photoresist alone, thus a double layer resist mask technique is employed. In double-layer lithography a lift-off resist is deposited first

via spin coating onto the Si substrate. The photoresist is then deposited via spin-coating atop the lift-off resist. During development of the photoresist (after UV exposure), the developer solution dissolves an undercut region of the lift-off resist. The height of the double layer relief mask should be minimum of ~ 5:1 depth ratio to the desired subsequent layer deposition. A smaller depth ratio results in persistent side-wall depositions.

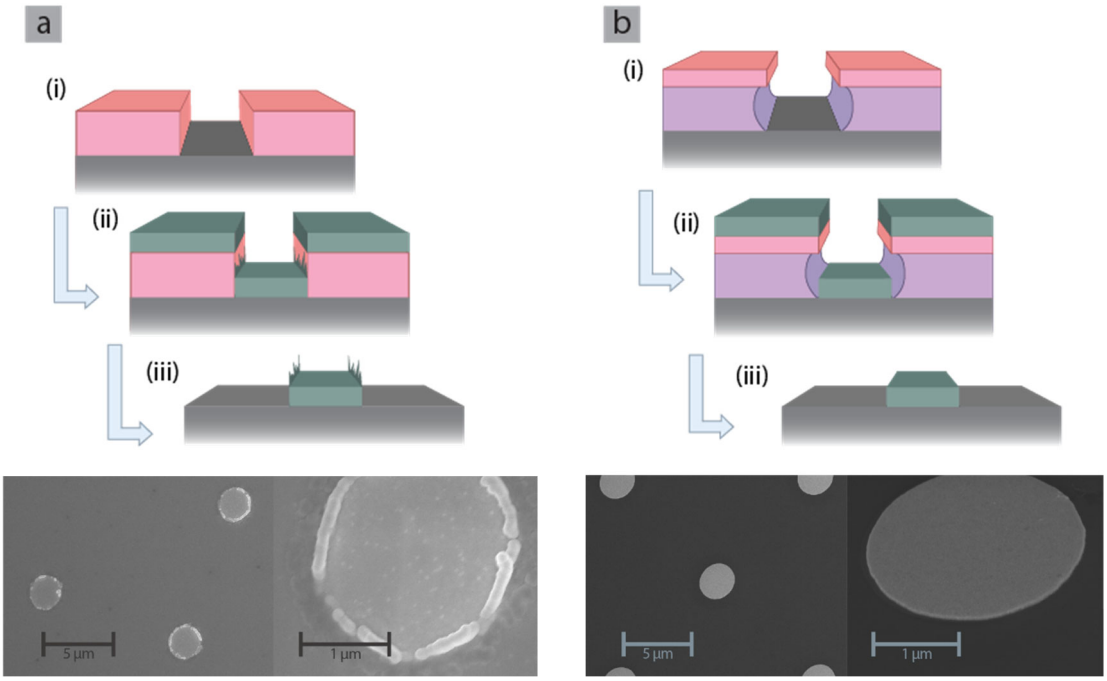

Figure 5.4. Illustrations and SEM images demonstrating the importance of an optimal mask layer prior to 3D metal pattern deposition: (a) technique employing only a UV photoresist, (i) spin-coating resist, (ii) metal deposition with undesirable side-wall deposition along photoresist walls, and (iii) removal of photoresist mask, leaving 3D patterned metal with undesirable 'crown' due to side-wall deposition. (b) Technique employing optimal double layer resist, (i) lift-off resist deposited via spin-coating under the photoresist, with depth > 5× desired metal deposition. The walls of the lift-off resist are under-cut by the photoresist developer, preventing side-wall deposition of metal. (iii) Perfectly patterned metal contacts remain after removal of double layer resist.

In this work, we aim to have a *thick* (up to 100 nm) layer of metal/oxide covering the substrate to maximize chemical protection of the underlying Si. Thus, the ideal thickness for the relief mask for this work should be at minimum 500 nm.

The following lithography steps were performed in a clean-room environment. Even minor particulate contamination on the substrate will be fatal to the overall fabrication process. A lift-off resist, PMGI SF 25 (MicroChem Corp.), was cast using a spin-coating recipe of 2000 rpm for 30 seconds, followed by a soft bake at 190°C for 1 minute (the final sixth layer was soft-baked for 5 minutes). This recipe results in a lift off layer that is ~100 nm thick. This recipe was 'stacked' six times to form a resist layer of the necessary thickness. A minimum of 5 minutes wait time between each iteration is necessary to allow drying and hardening of each layer. This prevents re-dissolution of the layer as it is coated with the new solution for the next iteration of spin-coating. Failure to allow each stack layer to dry between stacking the recipe results in thinning of overall lift off layer. It is not recommended to use N_2 gas or any inert gas stream to assist drying as keeping the process as particulate-free as possible is exceptionally important.

After six iterations of this process the total lift-off layer was approximately 1,000 nm thick, measured by stylus profilometry. The photoresist AZ®1512 (Integrated Micro Materials) was then cast, with a spin-coating recipe of 4000 rpm for 30 seconds, followed by a soft bake at 100°C for 1 minute. The UV exposure was done as a 50 x 50 array of 10 μm diameter circles, spaced closer than the diffusion length of the n-Si (40 μm spacing), at a power of 401 mJ/cm^2. Photoresist was then developed using AZ® 300MIF developer (Integrated Micro Materials) for 3 minutes to achieve optimal resist undercutting. Developing the resist for too long results in insufficient undercutting, which leads to the formation of detrimental side walls during the metal deposition phase. Samples were imaged in an optical microscope to confirm quality array patterning. Total

thickness measured in Figure 5.5 includes the depth added from the UV resist via atomic force microscopy (and by stylus profilometry).

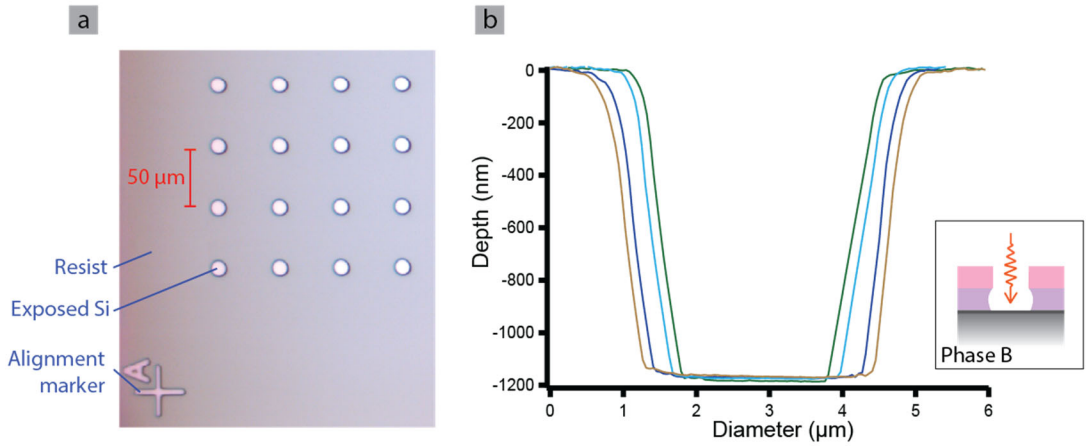

Figure 5.5. Characterization of a finished double layer optical resist technique. (a) Optical microscope images, top down image. (b) Atomic force microscopy measuring the depth and width of the mask pattern as a function of illumination power, 401 mJ/cm^2 (blue trace), 505 mJ/cm^2 (gold trace), 610 mJ/cm^2 (green trace), 702 mJ/cm^2 (black trace). The inset illustration corresponds to the step in Phase B of the overall fabrication scheme from Figure 5.3.

For samples with Si-oxide (SiOx) electrical passivation layers (instead of the Al_2O_3), the samples were set to rest for ~24 hours to allow for native oxide growth on the freshly exposed patterned regions. For samples with Al_2O_3 passivation layers (or no passivation layers) substrates were immediately progressed to the metal deposition phase of the fabrication process to prevent unwanted native SiOx growth. Contacts were deposited onto/into the UV mask as multi-layer metal stacks. Nickel is an optimal choice for the micro-contacts as $Ni(Fe)O_xH_y$ is presently known as the most-active catalyst for oxygen evolution reaction (OER) in alkaline electrolytes. However, the Ni becomes electrolyte permeable once fully converted into $Ni(OH)_2$/NiOOH during electrochemistry in alkaline electrolyte. Since a primary goal of this fabrication scheme is to protect the underlying Si surface from exposure to the electrolyte, the permeability of $Ni(OH)_2$/NiOOH is ultimately fatal to these electrodes. Thus a two metal stack structure

was employed, where a dense metal layer is deposited first and the Ni metal atop. The dense metal layer will prevent electrolyte permeating to the Si, and will permit free conduction of charge carriers to the Ni. Choice of metal interlayer is of utmost importance. This phase of fabrication creates a metal-oxide-semiconductor (MOS) interface where vital photogenerated electron-hole recombination must be minimized. A metal with an appropriate work function for a rectifying junction needs to be considered based on the band gap of the absorber semiconductor.[89] Here, we used only Pt or Pd as the dense metal interlayer.

The metal layers were deposited using a physical vapor deposition technique, electron beam (e-beam) evaporation. Solid metal material is placed in a high-temperature crucible and bombarded with a high intensity electron beam. The metal is heated to the point of melting and the vapor pressure causes a stream of evaporated metal to strike and deposit onto the substrate under high vacuum conditions of ~10^{-7} Torr.[90] Crucible choice is vital. Many metals will form alloys with improperly selected crucible materials, such as a commonly used tungsten crucible will form an alloy with palladium metal resulting in the loss of potentially thousands of dollars' worth of precious metals. More inert crucibles, such as graphite, will not form an alloy with palladium. However, graphite crucibles are highly susceptible to thermal shock and breakage. Graphite crucibles should only be used with slow and lower temperature metal depositions. In this work, a proprietary FABMATE® (99.9995% elemental carbon) crucible obtained from Kurt J. Lesker Company was used for depositions of nickel and palladium. Platinum was deposited from a common tungsten crucible obtained from Kurt J. Lesker Company.

Once the metal contacts were deposited into the relief pattern in the double layer resist, the lift-off resist is dissolved, removing both the lift-off and UV photoresist, and leaving the patterned metal array. Resist removal was conducted with a three-bath system. First, substrates were immersed in a heated (60-80 °C) bath of Remover PG (MicroChem Corp.) with rapid stirring near the substrates for 1-hour. Rapid stirring aids in the pristine removal of the resists, however care should used to not permit stirring near the substrates as mechanical shock can cause the loss of the unprotected metal contacts. Substrates were removed from the Remover PG, rinsed with acetone, and immersed in an ambient temperature acetone bath with stirring for a short duration (1-3 minutes). Substrates were then removed from the acetone, rinsed with isopropyl alcohol (IPA), and immersed in an ambient temperature IPA bath with stirring for a short duration (1-3 minutes). Finally, substrates were removed and thoroughly rinsed with DI water and dried with a filtered N_2(g) stream.

Phase C. Chemical protection.

The third phase of the fabrication is the deposition/growth of the metal oxide protective layer. Metal oxide layers to protect photoelectrodes have been regularly implemented since popularized by the use of TiO_2 in the 1970's.[91] Since that time, TiO_2 remains heavily researched and is still considered one of the most ideal materials for long-term stabilty.[79,80,82,92,93] However, in recent years hafnium oxide (HfO_2), hafnia, has emerged as a promising new material for chemical protection.[94–96] Hafnia has a relatively high refractive index in the visible spectrum (1.89), has a wide band gap of ~5.41 eV, and is highly optically transparent with insignificant absorption for wavelengths higher than 250 nm.[97] These favorable properties lead to a protective layer with higher light limited

currents than can be achieved with the alternative TiO_2. Further, hafnia has superior chemical stability in highly basic electrolytes, making it an ideal passivation layer for OER in alkaline conditions.[98]

The hafnia protection layer was deposited via atomic layer deposition (ALD). ALD provides the ability to deposit ultra-thin, uniform, and defect free films on planar and 3D patterned substrates. This technique grows the oxide in atomic monolayers continuously cycled to obtain the thickness desired.[99,100] Since the charge transport pathways in the photoanodes fabricated in this work are not through the protective oxide it is not necessary to keep the hafnia layer thin (tunneling of charge carriers not required). Thus, a "thick" ~25 nm layer was deposited to maximize long-term chemical stability of the anodes.

ALD HfO_2 film was deposited using a viscous-flow ALD reactor (Savannah G2 Thermal ALD, Veeco/Ultratech/Cambridge NanoTech). The chemical precursor used was Tetrakis(dimethylamido)hafnium, (TDMAHf). Films were deposited at 150°C by 250-cycles of alternating TDMAHf and H_2O flows with N_2 carrier flow gas. Under these conditions each cycle produces a HfO_2 layer of ~1.1 Å thickness. Thus, a 250 cycle procedure produced a ~25 nm Al_2O_3 film. Recipe and specifications were provided by the manufacturer, Veeco/Ultratech/Cambridge NanoTech.

The final steps in the fabrication scheme removes a small portion of the protective layer directly on top of the patterned Ni array, providing a direct interface between the metal and electrolyte and a charge carrier transport pathway to the underlying Si. This is achieved via a two-layered pattern approach for the lithography. An illustration of the two distinct layers to the lithography were programed: layer 1 (larger diameter circles)

was exposed during Phase B, and layer 2 (smaller diameter circles) were exposed during Phase C (Fig. 5.6). A two-layer pattern with alignment markers (a cross was used here) at least three of the four corners of the overall pattern is necessary for proper alignment of the lithography.

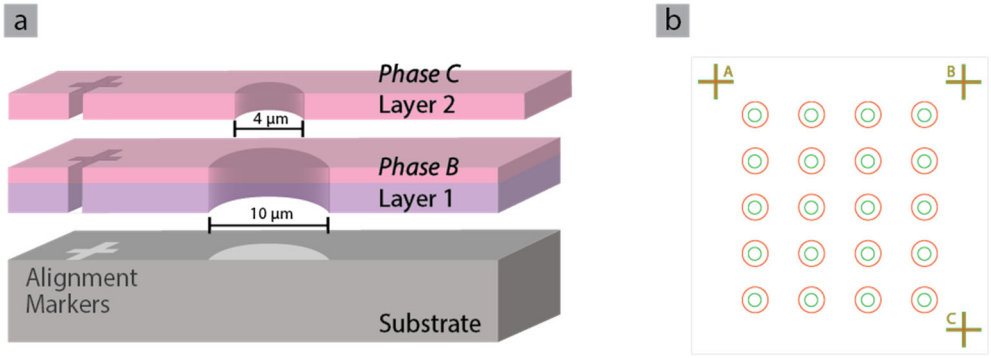

Figure 5.6. (a) Illustration of two-layer pattern used for UV lithography. (b) Illustration of two-layer pattern using alignment markers (layer 1, green; layer 2, orange). Alignment markers should be used in the corners of the overall pattern. Attempting two separate patterns versus a single two-layer pattern is not advisable due to difficulties that will be inherent in attempting to align two separate patterns.

The photoresist (AZ® 1512 without a double layer lift-off resist underlying) was deposited onto the hafnia via spin coating, with a recipe of 4000 rpm for 30 seconds, followed by a soft bake at 100°C for 1 minute. UV exposure was done of 4 µm diameter circles in a 50 x 50 array, aligned directly over the 10 µm diameter Ni array, at a power of 401 mJ/cm^2. After exposure the wafer was developed in AZ® 300MIF for 3 minutes. Following, ~4 µm diameter areas of the hafnia are exposed and can be etched away.

The final step is etching away a small area of the protective hafnia to expose a portion of the top of the Ni contacts. Both wet and dry (plasma) etching were investigated. While general etch rates of HfO_2 have been reported in the literature, there has been insufficient thorough characterization of the surface morphology and

photoelectrochemical activity of etched HfO_2 covered nickel metal surfaces.[101] Here, wet etching with buffered HF was compared to dry etching using reactive ion beam etching (RIBE) with Ar/CHF_3 gas mixture.

Ideally, wet etching leads to an isotropic etching, where dry etching is an anisotropic process (Fig. 5.7a). However, if the substrate has an initial surface roughness that is less than ideal, with high spatial frequency of rough surface features, the etching will not be ideally isotropic and will result in a highly roughened etched surface (Fig. 5.7b).[102] The HfO_2 layer to be etched is not perfectly smooth, and has high spatial frequency roughness, thus, idealized wet etching cannot be achieved as fabricated (Fig. 5.7c).

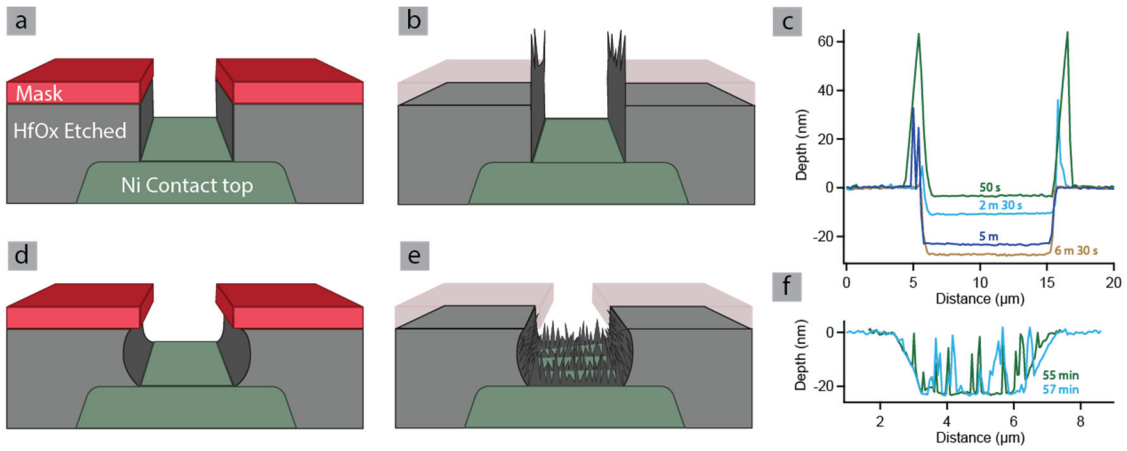

Figure 5.7. Illustrations and AFM data for wet and dry etching techniques. (a) *Idealized* anisotropic etching using dry etching method. (b) Illustration of dry etching where redeposition of bombarded material creates a side-wall or crowning effect. (c) AFM topology with side-wall formations. (d) *Idealized* isotropic etching using wet etching method. (d) Wet etching can result in a highly roughed surface. (f) AFM topology of wet etching demonstrating excessive roughening.

Dry etching can be superior under some conditions since the initial quality of the layer to be etched is not as significant a factor. However, dry etching can commonly result in redeposition of the bombarded material around the edges of the etch zone. This

causes undesirable side-wall or crowning formations. These formations are fairly thin and can be easily removed with mechanical shock via sonication in DI water for ~10 minutes. Optimization of etch technique and rates was done by performing several etches at different times (Fig. 5.7c). The morphology of the etched surfaces was investigated using atomic force microscopy (AFM). While the AFM measurements do not provide information about the degree of undercutting of the isotropic etching, the most important factor to investigate is to what degree each etching processes exposes (without destruction) the underlying nickel contacts. As can be seen in the AFM topological maps, even at the longest etch times using wet etching, the surface roughness is excessive and indicates insufficient exposure of the nickel. The topology of the dry etched surfaces reveals that after sufficient etching the nickel was sufficiently exposed with desired smoothness. A "descumming" technique via UV-ozone cleaning was applied to the HF wet etched samples to ascertain of the roughness was merely debris that could be removed. The roughness and definition of the holes actually worsened after UV-ozone cleaning (Fig. C.1).

These results were investigated electrochemically to determine the photoelectrochemical performance after each etching process. Despite etching for >55 minutes in the HF solution, the photocurrent for the wet etched HfO_2 covered nickel was severely depressed which correlates well with the rough and incomplete etching observed via AFM. Conversely, the dry etched samples indicate complete removal of the HfO_2 and an adequate photoelectrochemical response. Any deleterious effects potentially caused by over-etching were investigated via electrochemical characterization of etched Ni surfaces (Fig. C.2).

Electrochemical results and stability characterization

Photoanodes were fabricated using the procedures detailed above. Scanning electron microscopy (SEM) images were taken on the final structure to confirm successful structure formation (Fig. 5.8). Cross section SEM images show clean edges obtained from successfully optimizing the optical lithography and metal deposition steps of fabrication. The electrode shown has Ti as a thin bottom-most layer in the metal stack. This serves as a thin conductive 'adhesion' layer as Pd as poor adhesion to Si. The benefit to use Ti should be considered versus the care required in using the Ti layer. Ti readily oxidizes to TiO2 which would not be favorable (at the thickness deposited of 5-10 nm). Thus, if Ti is used to aid Pd adhesion to the Si the electrode should be moved *immediately* to the next fabrication step to cover the bare Si and exposed edges of the Ti with protective HfO_2. Prolonged resting between fabrication steps may be fatal to the electrode. Palladium (Pd) was used as the dense conductive layer in the metal stack. This layer serves (i) to set the work function at the Si interface, and (ii) to prevent electrolyte from reaching the Si (since NiO_xH_y is electrolyte permeable). Palladium as a high work function of 5.22 – 5.60 eV, leading to a high barrier height and greater hole-selectivity at the interface. While Pd also has less than ideal adhesion to Si, it was used as an alternative to Pt (also high work function, 5.12 – 5.93 eV) due to inferior adhesion of Pt on Si.

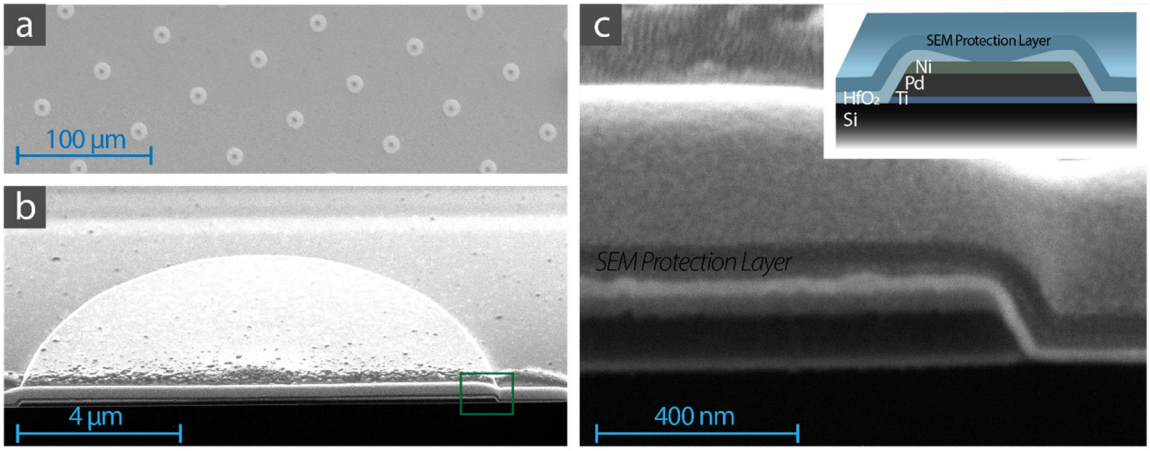

Figure 5.8. (a) SEM image of well-formed micro-contact structures. (b) Cross section image. Green box indicates enlarged area displayed in (c). Inset is a 2D cross-section illustration of the contact stack.

The electrochemical behavior of the electrode in the light limited current region demonstrates stability during prolonged operation at exceptionally high overpotential (2.8 V vs RHE, 1.6 V OER overpotential) for up to 24 hours tested in 0.1 M KOH (pH ~13) under ~1 sun illumination (Fig. 5.9a). Electrodes were also tested in the OER current region (2.0 V vs RHE, 770 mV OER overpotential) stability for 80 hours tested in 0.1 M KOH (pH ~13) under ~1 sun illumination (Fig. 5.9b). Performance was assessed in terms of (i) catalytic stability and activity, and (ii) anode structural stability.

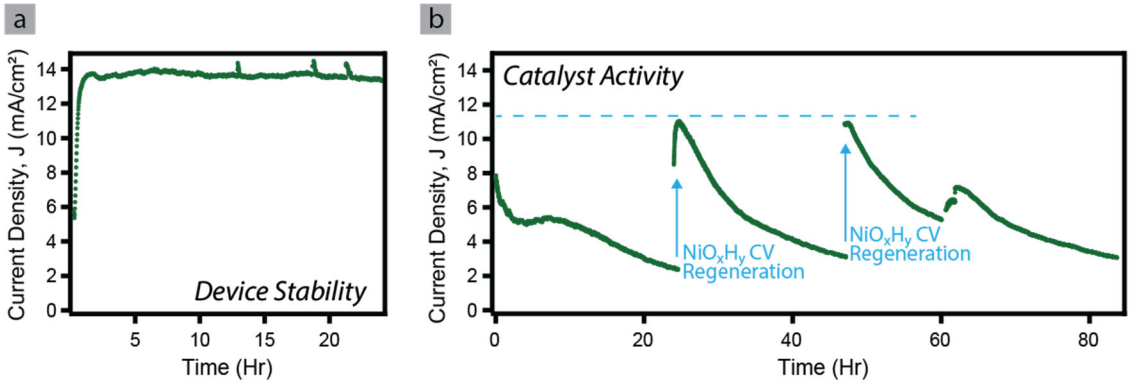

Figure 5.9. (a) Stable chronoamperometry in the light limiting current region (2.8 V vs RHE, 1.6 V OER overpotential) for 24 hours. (b) Chronoamperometry in OER catalytic region (2.0 V vs RHE, 770 mV OER overpotential) for 80 hours.

(i) Assessment of catalysis for stable photoanodes. The chronoamperometry data in the OER catalysis region (2.0 V vs RHE, 770 mV OER overpotential) displays a degradation/regeneration cycle for each 24-hour set of CVs-CA-CVs (Fig. 5.9b). This is characteristic of the Ni(Fe)O_xH_y catalyst and is discussed in more detail in Chapter III of this dissertation. Successful regeneration of the catalyst appears be sustainable up to 60 hours of operation. In the initial 72 hours the overall performance increases, and the Ni redox peak integration increases (Fig. 5.10). This is consistent with the deposition of Ni metal and the continuous conversion of all of the Ni metal to the NiO_xH_y material and uptake of Fe^{3+} for solution to form the active catalyst Ni(Fe)O_xH_y. This improvement is not related to the fabrication and is unique to the catalyst behavior (enhancement effects of Fe^{3+} in solution is discussed in Chapter IV of this Dissertation). An analogous control sample was run to demonstrate increasing NiO_xH_y redox peak with cycling due to the conversion of the Ni metal to NiO_xH_y (Fig. C.3). After 72 hours the electrochemical characterization of the electrodes presents with a decline in the OER activity and a significant degradation of the Ni redox peak integration and character. This indicates the catalyst may have reached the end of its useful operation period. However, does not indicate the overall anode structure has corroded or degraded.

(ii) Assessment of photoanode physical structure. Separate from any changes in the catalysis over time, the physical stability of the fabricated structure is well intact. Inspection of the electrode via optical microscopy demonstrate the changes in the catalyst region (roughening and darkening over time) have no deleterious effect on the structure,

nor have there been any general damage to the overall structures after 100 hours of operation (Fig. 5.10f).

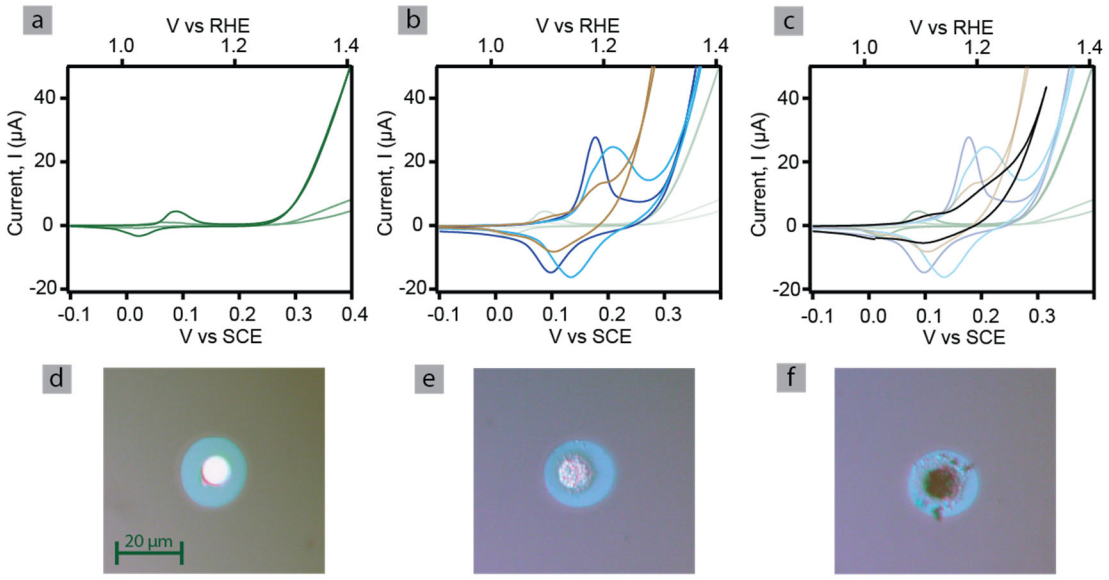

Figure 5.10. Cyclic voltammetry in 0.1 M KOH (pH ~13) collected every 24 hours of high overpotential chronoamperometry (2.0 V vs RHE, 770 mV OER overpotential). (a) Initial cycle 1 (light blue) and cycle 40 before any CA (dark green). (b) CV taken after 24 hours (teal), 48 hours (blue), and 72 hours (gold). (c) CV taken after 96 hours of operation (black curve, previous curves are lightened for clarity). (d) Pristine contact imaged under an optical microscopy, (e) Contact imaged after 72 hours of operation. (f) Contact imaged after 96 hours of operation.

The fabrication methods developed here have been successful in protecting the photoanodes from chemical corrosion in the harsh 0.1 M KOH solutions (pH ~13). Further work would be warranted using these methods for chemically protected photoanodes with more a robust OER catalysts. Further work would also benefit greatly from optimization of the semiconductor interface to reduce interfacial electron-hole recombination that is likely reducing the maximum achieved light limiting current obtained in our electrodes.

Selecting a fabrication scheme for stable micro-contacts: embedding into protection layer versus covering with protection layer.

When considering the fabrication scheme and structure, there were two interfaces of utmost importance: the semiconductor/contact interface and the catalyst/electrolyte interface. The two example fabrication designs *embedded* and *covered*, demonstrate two approaches considering both vital interfaces (Fig. 5.11).

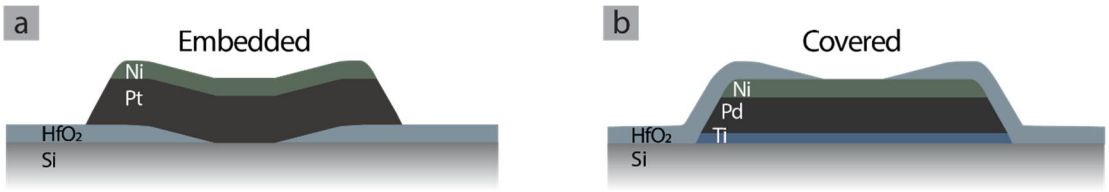

Figure 5.11. Two approaches for fabrication of photoanodes to protect an underlying substrate. (a) Embedded contact technique. (b) Covered contact technique.

Photoelectrochemical water splitting includes a semiconductor which brings about photogenerated holes to oxide water. Many photoanodes have a layered structure, where the semiconductor is coated with a catalyst or hole conducting layer. Thus, the interface of the semiconductor/contact should be considered when designing a fabrication scheme. The photogenerated holes must pass to and/or through this layer before they can be used for water oxidation. In the methods presented, the Ni(Fe)O_xH_y catalyst over-layer serves as a collector of photogenerated holes.[103] Ni (oxy)hydroxide is an electrolyte permeable catalyst, therefore, the photogenerated holes which pass into the catalyst can accumulate throughout the bulk. Steady state conditions are achieved when the net flux of hole from the semiconductor into the catalyst is equal to the flux out of the catalyst. Thus, if the surface area of the semiconductor/catalyst interface is not equal to that of the catalyst/electrolyte interface there will be different theoretical current densities at each

interface. On the one hand, maximizing semiconductor/catalyst interface surface area (*covered*) can be beneficial for stability and even charge distribution across and throughout the contacts. However, minimizing semiconductor/catalyst interface surface area (*embedded*) can have exceedingly favorable consequences; there are significant changes to the interfacial physics that govern efficient charge transfer when the contact dimension approach or become less than the depletion length of the semiconductor (on the order of 10-1,000 nm).[104,105] Further, there is a considerable catalytic benefit in maximizing the catalyst interface with the electrolyte (*embedded*). Since the exceptional OER catalysts such as NiO_xH_y are most catalytically active at surface and defect sites, maximizing accessible catalytic surface sites will lead to higher TOF when comparing identical catalyst loading between embedded and covered fabrication schemes. For these reasons, the *embedded* approach has many advantages compared to the *covered* approach.

However, the embedded technique tends to facilitate delamination and loss of contacts as a primary failure pathway for photoanodes. As shown in the 2D cross-section illustration of the embedded contact, atop the silicon the contact stack is a dense metal and then a catalyst (Fig. 5.12a). The high-work function metal is necessary for proper rectifying qualities to prevent electron-hole recombination at the interface. However, appropriate metals such as Pt and Pd do not have good adhesion to the Si substrate. This causes prompt delamination of the contact before and during operation (Fig. 5.12b-c). One common solution to poor adhesion is the addition of an adhesion layer between the Si substrate and the high-work function metal layer. Materials such as TiO_2 have been used as optimal adhesion layers. However, an embedded scheme exposes all of the stack layers to the electrolyte, and thus, all layers must be resistant to corrosion. This presents a

problem as many adhesion layers are not stable in highly alkaline electrolyte. Finally, the importance of an electrical passivation layer was mentioned in this work, but not addressed in depth. Further development of these fabrication schemes will require inclusion of an electrical passivation layer at the semiconductor interface to minimize charge recombination. However, identical to the stability issues present for adhesion layers, common electrical passivation layers are generally not stable when exposed to the highly alkaline electrolyte.

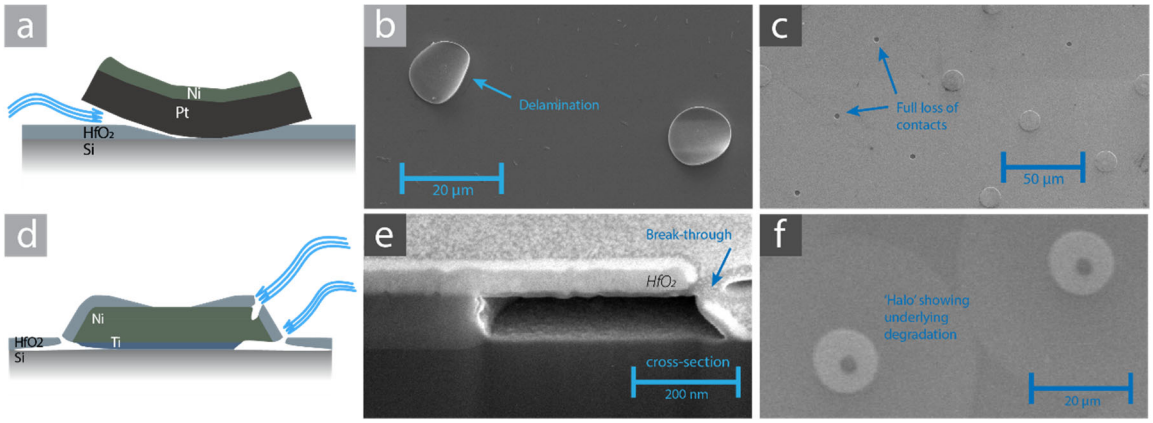

Figure 5.12. Illustrations and SEM images of the pathways for degradation and photoanode failure (a) Embedded technique leads to delamination of the contacts. (b) SEM images of curling and delaminating contacts, and (c) loss of entire contacts. (d) Covered technique has the risk of electrolyte break-through of the protection layer. (e) SEM images of electrolyte break-through causing dissolution of stack layers and (f) 'halos' around the contacts indicating likely oxidation of the underlying Si substrate.

A covered approach can address many of the problems existent in the embed fabrication scheme. The covered technique is superior to embedded in terms of physical stability and maintenance of the contacts. However, the geometry of the structure is now reversed, with a large surface area at the semiconductor/contact interface and a smaller surface area at the catalyst/electrolyte interface. Consequently, two substantial sacrifices are made: forfeiture of any potential nano-scale benefits and higher catalytic activity. Nano-scale benefits become more difficult as fabrication schemes would require more

advanced techniques such as electron-beam lithography and difficulties during the etching steps due to very small diameter pores to wet and dry etch cleanly.

The stability benefits will also allow for improved treatment of the semiconductor/catalyst interface. Since the layers in the contact stack are no longer exposed to the electrolyte a much-desired electrical passivation layers can be incorporated. While this scheme has its structural advantages, there are still failure pathways that need to be considered. Deposition of the HfO_2 needs to be optimized. Too thick and the pores become deep and difficult to conduct flawless UV lithography and etching without detrimental side-wall depositions. Further, if there are any side wall formations during the metal deposition step and these thin side walls are covered by the HfO_2 protection, there is a greater possibility of edge breakage and then exposure to the electrolyte. Additionally, simply too thin a protection layer and the edges and corners of the protection layer are susceptible to electrolyte break-through, which can lead to dissolution of adhesion/passivation layers. Thus, fatal break-through can be the result of protection layers that are (i) too thin, (ii) have pinholes, and/or (iii) have covered side walls formations that readily break away. Overall, the covered technique was deemed superior for the reasons described in this section.

Conclusions

Effective methods for protection and passivation of solar absorbers remain a primary consideration for researchers furthering the advancements in the photoelectrochemical water splitting field. Here, Si is used as a model material to develop a fabrication scheme for chemically stable photoanodes for the oxygen evolution reaction performed in highly alkaline electrolytes. The fabrication method presented uses a multi-

layered approach to deposit an array of contacts and cover the electrode with an overall protection oxide. The electrodes fabricated using this scheme have shown physical stability up to 100 hours tested, with no break-down of the contact array structures. There was, however, degradation related to the catalyst which was addressed separately in Chapters III and IV of this dissertation. In addition to presenting the methods for fabrication and reporting on the stability of the photoanodes fabricated using this scheme, a discussion was presented regarding important factors to be considered when selecting methods and strategies for photoanode fabrication. Further work in this area would be warranted to explore the trade-off between high activity and stability, and to investigate catalysts with higher chemical stability to assess this photoanode fabrication scheme to the limits of stability.

APPENDIX A

CHAPTER III SUPPORTING INFORMATION

Electrolyte purification and removal of particulates

After the Fe impurities are removed using a high-purity $Ni(OH)_2$ Fe-absorbent soak (~overnight) there are $Ni(OH)_2$ particulates in the solution. A freshly cleaned (aqua regia) Pt coil used as a working electrode was cycled 150 times (50 mV/s). Redox peaks for NiO_xH_y grow in indicating significant deposition of $Ni(OH)_2$ on the surface of the Pt coil from solution particulates (Fig. A.1). The electrode was removed and cleaned in 1.0 M H_2SO_4 for 2 minutes and aqua regia for 2 minutes. The process was repeated until NiO_xH_y redox peaks were no longer present. This process required 6 iterations, for a total of ~900 CV cycles to remove *most* particulates that would cause unintended deposition.

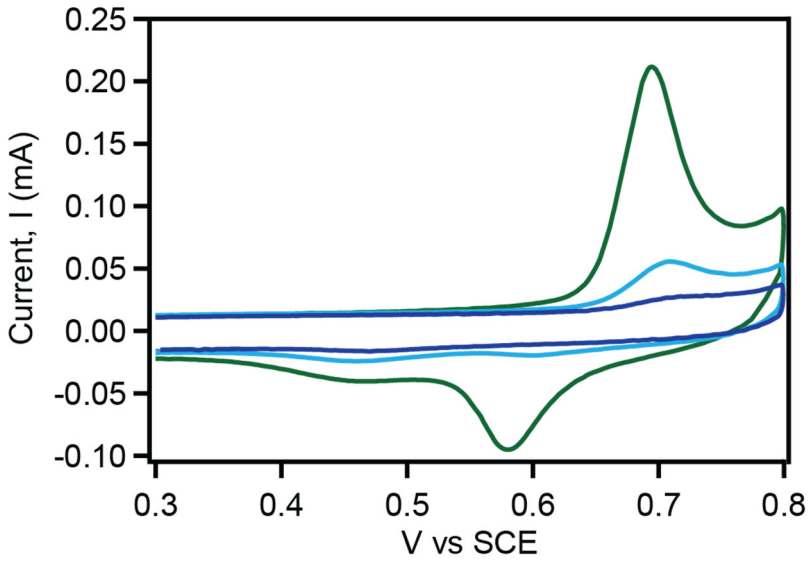

Figure A.1. Cyclic voltammetry demonstrating the necessity for removing $Ni(OH)_2$ particulates from electrolyte. In Fe-cleaning 0.1M KOH electrolyte, after 150 CV cycles there is significant $Ni(OH)_2$ deposition on a Pt coil working electrode (green trace). After cleaning and an additional 300 CV cycles, $Ni(OH)_2$ deposition is still present (teal trace). A minimum of 900 CVs was required to remove the majority of $Ni(OH)_2$ deposition (blue trace), with very trace deposition still present.

As seen in Fig. A.1, after the 6 iteration of electrochemical particulate removal there is still very slight redox character visible, indicating a minor deposition still occurring. As an alternative to electrochemical removal of particulates, a double-filtration cleaning process was implemented using a 0.1 μm Supor (polyethersulfone) membrane syringe filters (VWR, Pall Acrodisc®). This resulted in the removal of all detectible $Ni(OH)_2$ particulates and a pristine Pt surface after CV cycling (Fig. A.2a).

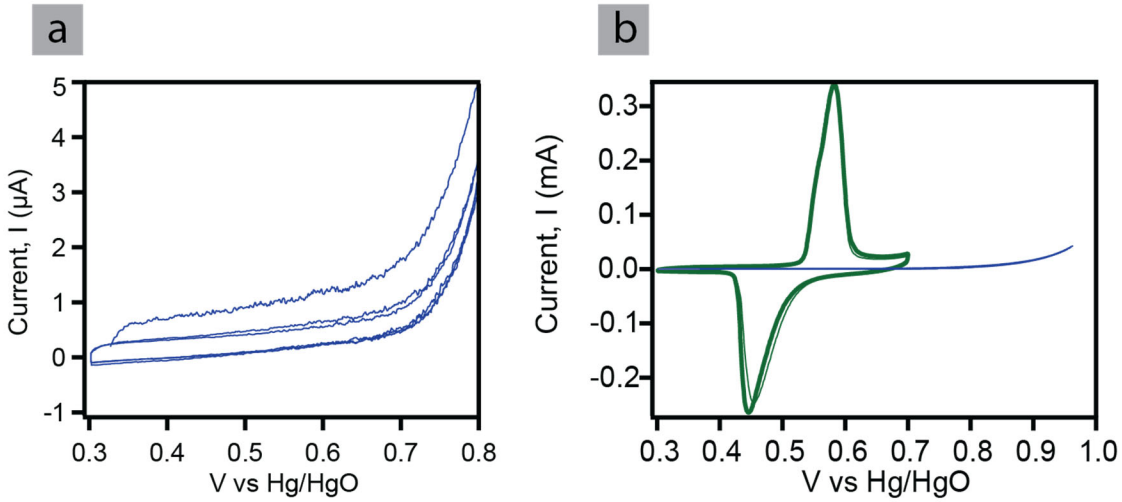

Figure A.2. (a) Characterization of clean Pt substrate surface prior to deposition of catalyst. (b) Characterization of catalyst after deposition (green) compared to the pre-deposition clean Pt substrate (blue). 0.1 M Fe-free KOH, 10 mV/s scan rate.

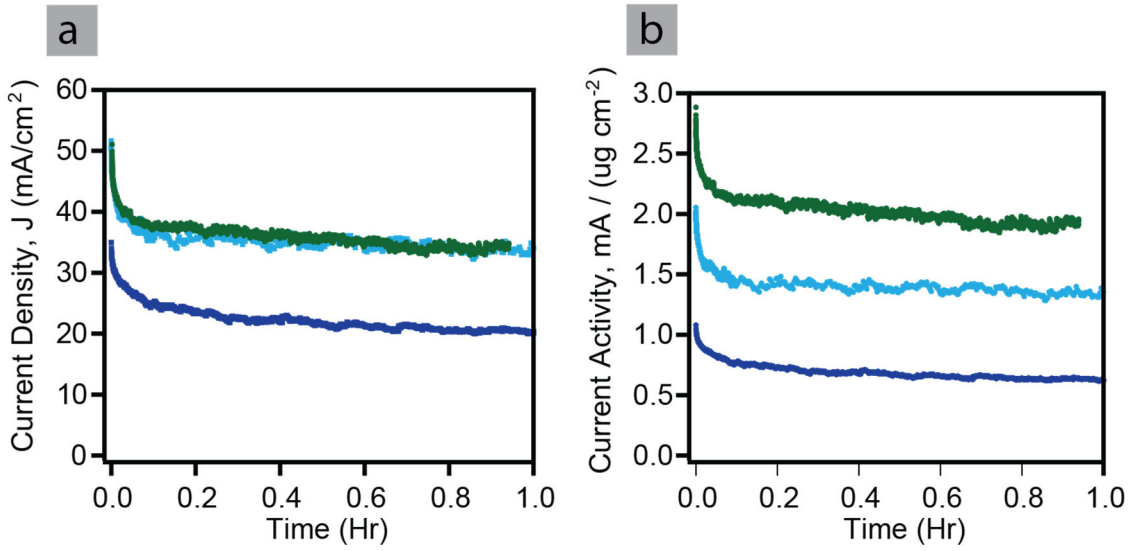

Figure A.3. Chronoamperometry operated at 1.0 V-iR vs Hg/HgO (0.688 V-iR overpotential) after 3 CVs (green) electrochemical cycling prior, 20 CVs prior (teal), and 40 CVs prior (dark blue). (a) Reported a current density, with convoluted results due to difference in both surface area and catalyst loading of the '3 CV' electrode. (b) Reported as current activity to normalize for variance in surface area and loading.

Table A.1. Electrode surface areas and catalyst loading for chronoamperometry cycling-activity experiments (Fig. 3.1). Table indicates the similarities in the '20 CV' and '40 CV' electrodes and the dissimilarity of the '3 CV' electrode in comparison. Catalyst loading was determined via charge integration of the redox peaks immediately following electrodeposition.

Electrode Cycling	Pt Substrate Surface Area (cm^2)	Ni deposited (ng)	Ni Loading ($\mu g/cm^2$)
3 CV	0.2436	1036.57	4.26
20 CV	0.1553	605.94	3.90
40 CV	0.1428	558.84	3.91

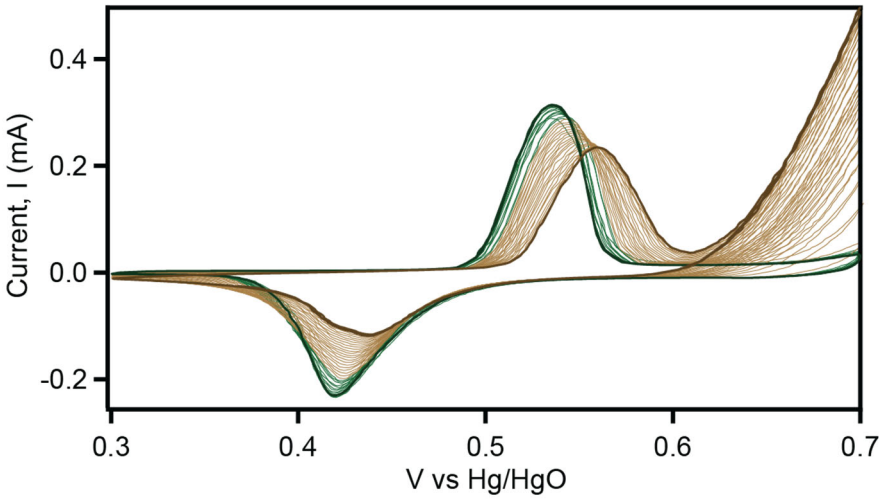

Figure A.4. Cyclic voltammetry performed on an initially rigorously Fe-free electrode in Fe-free 0.1 M KOH (dark green trace). Diminutive quantities of Fe were spiked in-situ to simulate trace impurities potentially existent in 'Fe-free' experiments. Spikes between 0.1 ppb through 0.25 ppb show no enhancement from cycle 1 through cycle 13 (green traces). At 0.7 V vs Hg/HgO the traces are indistinguishable. No enhancement factor is visible until a spike of 20 ppb at cycle 14 (gold traces) which presents with an immediate, clear, and significant OER enhancement through the final cycle 36 (dark gold).

APPENDIX B

CHAPTER IV SUPPORTING INFORMATION

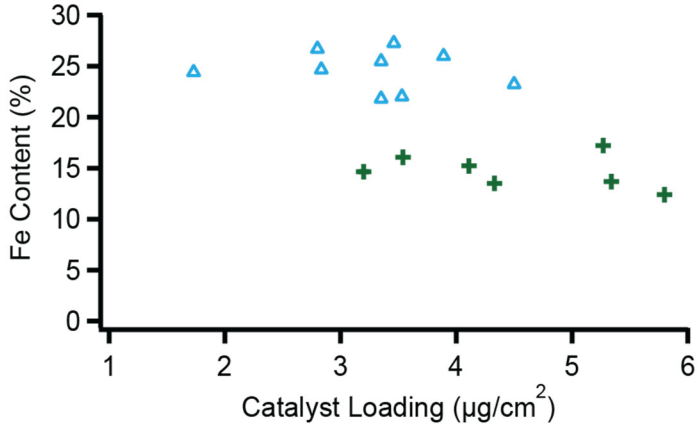

Figure B.1. Fe content determined by ICP-MS for Fe/(Fe+Ni) as a function of catalyst loading. There is no apparent dependence of Fe uptake based on catalyst loading in this loading regime of < 6 µg/cm^2. Fe content is ~15% after 50 cycles of cyclic voltammetry (green cross), ~22-25% after 100 or more cycles (teal triangles). There is a clear correlation between Fe uptake and number of cycles.

Determination of Fe% from ICP-MS and calculations for propagation of uncertainties

The analysis and reporting of uncertainties associated with inductively coupled plasma mass spectrometry (ICP-MS) presented here are consistent with guidelines published regarding analytical ICP-MS.[65,66,106] Dominant contributions to uncertainty in ICP-MS are instrument method precision and instrument drift. Uncertainties with this method associated with standard calibration solution concentrations and analyte sample dilutions are considered negligible when analytical care is used to perform the technique.[65] Accordingly, our propagation of uncertainty will not include these negligible values. Further, the use of an internal standard was used to correct for instrument drift, and as such, instrument drift is not explicitly included in our uncertainty analysis. The uncertainties reported herein are due to instrument method precision with respect to

measured analyte concentration, ppm (directly measured as counts s^{-1}), and is propagated through to determine Fe content as a percentage of total analyte mass.

Initial ppb values direct from digested electrodes was obtained from ICP-MS measurements, collected with a method of 5 replicate measurements, $A_{ppb} \pm \delta A_{ppb,}$ where A is the analyte atomic identity and δA is the uncertainty with respect to the method precision, or the standard deviation of the 5 replicate measurements. These concentrations were converted to mass (ng) of atomic analyte by multiplying by the volume (mL) of the analyte solution, $A_{ng} \pm \delta A_{ng}$, where δA is propagated uncertainty calculated in quadrature per Equation B.1. As stated above, uncertainty with respect to solution measurements (done gravimetrically for all work done here) is negligible and omitted in these equations.

$$\frac{\delta A_{ng}}{A_{ng}} = \sqrt{\left(\frac{\delta A_{ppb}}{A_{ppb}}\right)^2} \qquad (Eq.\ B.1)$$

Percent Fe content (Z) in the electrodes presented in this work is Fe/(Ni+Fe), where Ni+Fe (T_{ng}) is the sum in units of mass (ng) determined via ICP-MS as described above, $T_{ng} \pm \delta T_{ng}$, where δT_{ng} is propagated uncertainty calculated via sum, per Equation B.2.

$$\delta T_{ng} = \sqrt{\delta Fe_{ng}{}^2 + \delta Fe_{ng}{}^2} \qquad (Eq.\ B.2)$$

Percent Fe is then reported as $Z \pm \delta Z,$ where δZ is propagated uncertainty calculated in quadrature per Equation B.3.

$$\frac{\delta Z}{Z} = \sqrt{\left(\frac{\delta Fe_{ng}}{Fe_{ng}}\right)^2 + \left(\frac{\delta T_{ng}}{T_{ng}}\right)^2} \qquad (Eq.\ B.3)$$

Table B.1. Representative sample of electrodes analyzed via ICP-MS for %Fe content with propagation of uncertainty.

Technique	KOH M	ICP-MS Fe ppb	STD	mL	Fe ng	δ	RDS	Ni ng	δ	RDS	Total ng	δ	Fe %	δ	RDS
Min. Exposure	0.1	8.562	0.53	4.953	42.41	2.61	0.06	331.71	10.33	0.03	374.12	15.56	11.34	0.84	0.07
Min. Exposure	0.1	8.987	0.74	5.288	47.53	3.91	0.08	448.55	20.41	0.05	496.07	24.05	9.58	0.92	0.10
4Hr Only	0.1	12.22	0.47	5.099	62.30	2.40	0.04	447.58	13.75	0.03	509.88	18.20	12.22	0.64	0.05
4Hr Only	0.1	10.92	0.33	5.038	55.00	1.67	0.03	259.55	10.47	0.04	314.55	15.67	17.49	1.02	0.06
4Hr Only	0.1	22.57	0.7	5.256	118.60	3.69	0.03	792.27	14.60	0.02	910.87	19.28	13.02	0.49	0.04
10Hr Only	0.1	12.38	0.44	5.135	63.55	2.25	0.04	357.19	11.50	0.03	420.74	16.60	15.10	0.80	0.05
10Hr Only	0.1	14.99	0.46	5.079	76.11	2.35	0.03	492.99	17.27	0.04	569.10	20.95	13.37	0.64	0.05
50CV	0.1	16.61	0.27	4.980	82.73	1.34	0.02	482.16	9.91	0.02	564.89	15.17	14.65	0.46	0.03
50CV	0.1	11.47	0.28	5.078	58.23	1.41	0.02	485.49	11.28	0.02	543.71	16.26	10.71	0.41	0.04
50CV	0.1	18.12	0.34	4.948	89.68	1.69	0.02	468.87	11.29	0.02	558.55	16.08	16.06	0.55	0.03
50CV	1.0	13.17	0.48	5.089	67.03	11.90	0.18	368.40	14.06	0.04	435.43	18.42	15.39	2.81	0.18
50CV	1.0	24.97	0.6	5.105	127.46	12.09	0.09	646.64	13.92	0.02	774.10	18.44	16.47	1.61	0.10
50CV-4Hr	1.0	16.22	0.7	5.059	82.06	12.12	0.15	362.35	14.75	0.04	444.40	19.09	18.46	2.84	0.15
50CV-4Hr	1.0	13.44	0.47	5.045	67.79	11.80	0.17	283.59	13.42	0.05	351.38	17.87	19.29	3.50	0.18
50CV-10Hr	1.0	13.93	0.92	5.110	71.21	12.62	0.18	235.83	11.91	0.05	307.04	17.35	23.19	4.31	0.19
100CV	0.1	15.62	0.69	5.154	80.52	3.56	0.04	294.32	16.17	0.05	374.84	20.33	21.48	1.50	0.07
100CV	0.1	32.63	1.12	5.025	163.99	5.63	0.03	501.04	22.56	0.05	665.03	25.94	24.66	1.28	0.05
50CV-4Hr-50CV	0.1	10.1	0.58	5.211	52.65	3.02	0.06	140.57	10.42	0.07	193.22	16.13	27.25	2.76	0.10
50CV-4Hr-50CV	0.1	17.14	0.51	5.250	89.97	2.70	0.03	263.17	11.24	0.04	353.14	16.68	25.48	1.43	0.06
50CV-4Hr-50CV	0.1	21.34	0.65	5.015	107.00	3.27	0.03	293.93	12.43	0.04	400.93	17.23	26.69	1.41	0.05
50CV-4Hr-50CV	0.1	36.76	1.51	4.975	182.87	7.50	0.04	520.82	11.99	0.02	703.69	18.16	25.99	1.26	0.05
50CV-11Hr-50CV	0.1	10.44	0.82	5.018	52.38	4.10	0.08	162.27	10.06	0.06	214.65	15.82	24.40	2.62	0.11
50CV-10Hr-50CV	0.1	35.43	0.79	5.188	183.81	4.11	0.02	607.62	10.63	0.02	791.43	16.46	23.22	0.71	0.03
50CV-10Hr-50CV	0.1	23.68	0.92	4.973	117.77	4.55	0.04	289.75	11.00	0.04	407.52	16.47	28.90	1.62	0.06

APPENDIX C

CHAPTER V SUPPORTING INFORMATION

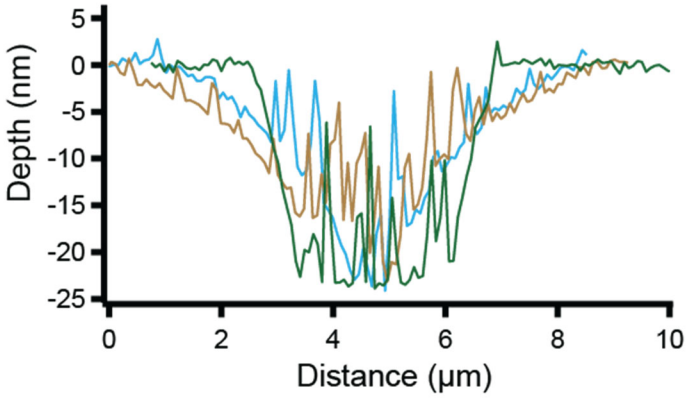

Figure C.1. Atomic force microscopy (AFM) topology of etched holes in the HfO_2 protection layer via wet (HF) etching for 57 minutes (green). UV-ozone cleaning was performed for 2 minutes (teal) and 4 minutes (gold) which did not improve the surface roughness of the etch region.

Before the dry etching method was applied to the fabrication scheme, the impact of over-etching was investigated. The topography calibration tests indicated RIBE etching for approximately 7 minutes was sufficient to obtain a smooth exposed Ni contact, free from the 25 nm HfO_2 protection layer etched away. In the event ~7 minutes was slightly more than necessary, causing effective over-etching. This may etch and/or damage the Ni layer.

Using planar Ni deposited on Si, the electrochemical consequences to potential over-etching was investigated. Figure C.2 reports over etching has no detrimental effects up to approximately 1-minute over-etching. However, over-etching in excess of 1 minute up to 2 minutes tested proved to damage and etch the Ni resulting in a decrease in Ni

redox peaks and a reduction of light limited current. It is noted, however, that the OER onset was no effected.

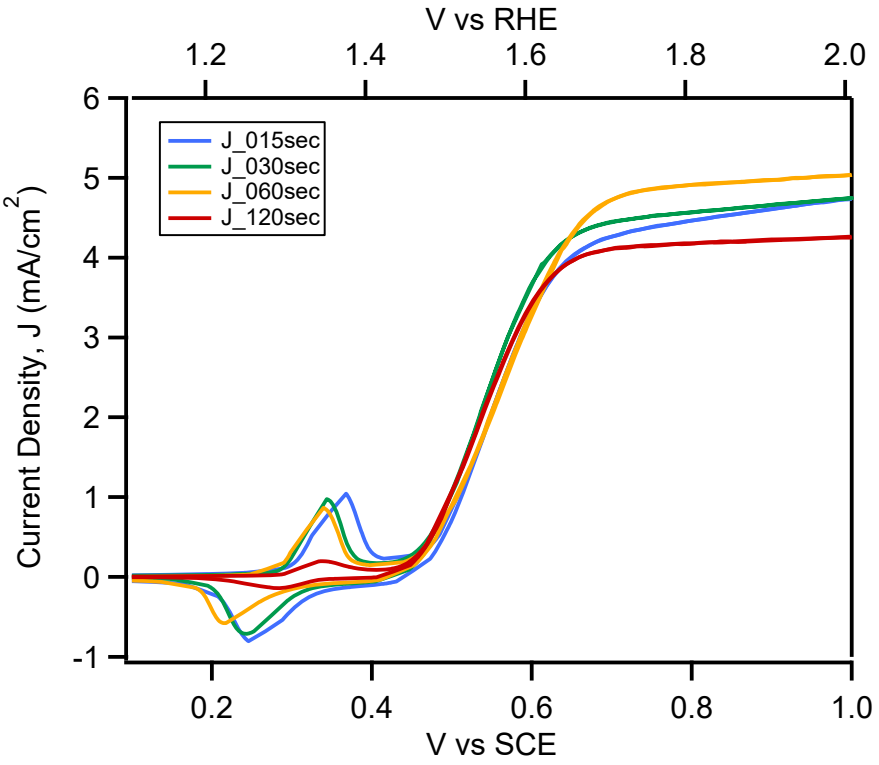

Figure C.2. Cyclic voltammetry of silicon substrates covered with 25 nm Ni film (illuminated ~1 sun at Ni face). Light limiting current is depressed due to full coverage of Ni metal film over the photo-absorbing Si substrate. Electrodes were directly exposed to the RIBE technique to assess potential damage to the Ni catalyst. No detrimental effects were seen for 15 seconds (blue trace), 30 seconds (green trace), and 60 seconds (gold trace). RIBE of 120 seconds presents with decreasing Ni redox peaks and a decrease in light limited OER current (red trace). The OER onset is unaffected for all over-etching tested.

This control electrode is Ni metal directly on the Si photoanode with no protection layers coating/obstructing the Ni contacts. The initial poor OER behavior and improvement with only 40 cycles is consistent, indicated both conversion from Ni metal to the active $Ni(OH)_2$/NiOOH catalyst and advantageous uptake of trace Fe from the electrolyte (discussed extensively in Chapter 3 of this Dissertation).

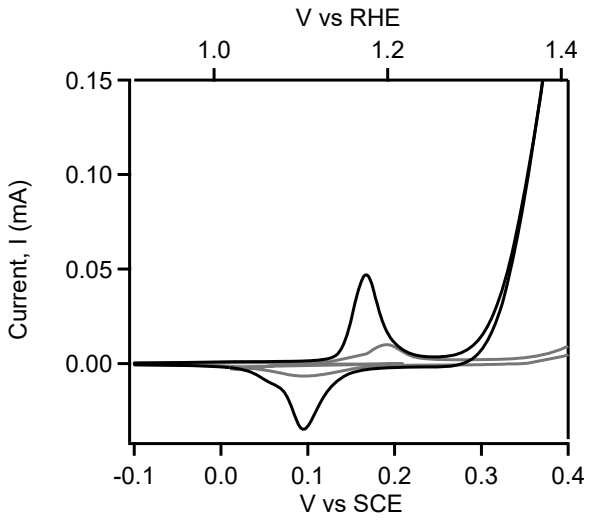

Figure C.3. (a) Cyclic voltammetry 0.1 M KOH (pH ~13) of a control electrode of Ni-metal contacts on a Si photoanode with no protect layers. The initial CV curve (gray) has poor OER onset and small redox peaks. After the initial 40 cycles (black) there is an improved OER onset and significant increase in redox peaks.

REFERENCES CITED

(1) Rosenstock-Huessy, E. The Scientific Grammar of Michael Faraday (1791-1867). In *Rosenstock-Huessy Papers, Volume 1*; Wipf & Stock Pub: Eugene, OR, 1981.

(2) BP p.l.c. *Bp Statistical Review of World Energy 2020*; 69th edition; S&P Global Platts, 2020; p 68.

(3) Lashof, D. A.; Ahuja, D. R. Relative Contributions of Greenhouse Gas Emissions to Global Warming. *Nature* **1990**, *344* (6266), 529–531. https://doi.org/10.1038/344529a0.

(4) Climate Change 2007: The Physical Science Basis. In *Intergovernmental Panel on Climate Change*; Solomon, S., Qin, D., Manning, M., Marquis, M., Averyt, K., Tignor, M. M. B., Miller, Jr., H. L., Chen, Z., Eds.; Cambridge University Press: Cambridge ; New York, 2007.

(5) IRENA. *Renewable Energy Options for the Industry Sector: Global and Regional Potential Until 2030*; Background to "Renewable Energy in Manufacturing" Technology Roadmap; International Renewable Energy Agency IRENA: Abu Dhabi, 2015; p 85.

(6) Gurney, K. R.; Mitra, B.; Roest, G.; Dass, P.; Song, Y.; Moiz, T. United States Fossil Fuel Carbon Dioxide Emissions and the COVID-19 Pandemic: The Implications of near-Real-Time Fuel Consumption Data. **2021**.

(7) Kudo, A.; Miseki, Y. Heterogeneous Photocatalyst Materials for Water Splitting. *Chem. Soc. Rev.* **2008**, *38* (1), 253–278. https://doi.org/10.1039/B800489G.

(8) Xiang, C.; Papadantonakis, K. M.; Lewis, N. S. Principles and Implementations of Electrolysis Systems for Water Splitting. *Mater. Horiz.* **2016**, *3* (3), 169–173. https://doi.org/10.1039/C6MH00016A.

(9) Haynes, W. M.; Lide, D. R.; Bruno, T. J. *CRC Handbook of Chemistry and Physics: A Ready-Reference Book of Chemical and Physical Data.*, 2015th–2016th, 96th Edition / ed.; CRC Press: Boca Raton, Florida, 2015.

(10) Doyle, R. L.; Lyons, M. E. G. The Oxygen Evolution Reaction: Mechanistic Concepts and Catalyst Design. In *Photoelectrochemical Solar Fuel Production*; Giménez, S., Bisquert, J., Eds.; Springer International Publishing: Cham, 2016; pp 41–104. https://doi.org/10.1007/978-3-319-29641-8_2.

(11) Revised Pourbaix Diagrams for Nickel at 25–300 °C. *Corrosion Science* **1997**, *39* (5), 969–980. https://doi.org/10.1016/S0010-938X(97)00002-4.

(12) Bode, H.; Dehmelt, K.; Witte, J. Zur Kenntnis Der Nickelhydroxidelektrode—I.Über Das Nickel (II)-Hydroxidhydrat. *Electrochimica Acta* **1966**, *11* (8), 1079–1087. https://doi.org/10.1016/0013-4686(66)80045-2.

(13) McBreen, J. Nickel Hydroxides. In *Handbook of Battery Materials*; Besenhard, J. O., Ed.; Wiley-VCH: New York, 1999; pp 135–151.

(14) Wehrens-Dijksma, M.; Notten, P. H. L. Electrochemical Quartz Microbalance Characterization of Ni(OH)2-Based Thin Film Electrodes. *Electrochimica Acta* **2006**, *51* (18), 3609–3621. https://doi.org/10.1016/j.electacta.2005.10.022.

(15) Oliva, P.; Leonardi, J.; Laurent, J. F.; Delmas, C.; Braconnier, J. J.; Figlarz, M.; Fievet, F.; Guibert, A. de. Review of the Structure and the Electrochemistry of Nickel Hydroxides and Oxy-Hydroxides. *Journal of Power Sources* **1982**, *8* (2), 229–255. https://doi.org/10.1016/0378-7753(82)80057-8.

(16) Faure, C.; Willmann, P.; Delmas, C. Preparation and Characterization of Cobalt-Substituted a-Nickel Hydroxide Stable in KOH Medium Part II. a-Hydroxide with a Turbostratic Structure. *J. Power Sources* **1991**, No. 35, 263–277.

(17) Bernard, M. C.; Cortes, R.; Keddam, M.; Takenouti, H.; Bernard, P.; Senyarich, S. Structural Defects and Electrochemical Reactivity of β-Ni(OH)2. *Journal of Power Sources* **1996**, *63* (2), 247–254. https://doi.org/10.1016/S0378-7753(96)02482-2.

(18) Rajamathi, M.; Subbanna, G. N.; Kamatha, P. V. On the Existence of a Nickel Hydroxide Phase Which Is Neither a nor b. *J. Mater. Chem.* **1997**, *7* (11), 2293–2296.

(19) Corrigan, D. A. The Catalysis of the Oxygen Evolution Reaction by Iron Impurities in Thin Film Nickel Oxide Electrodes. *J. Electrochem. Soc.* **1987**, *134* (2), 377. https://doi.org/10.1149/1.2100463.

(20) Greaves, C.; Thomas, M. A. Refinement of the Structure of Deuterated Nickel Hydroxide, Ni(OD) $_2$, by Powder Neutron Diffraction and Evidence for Structural Disorder in Samples with High Surface Area. *Acta Crystallogr B Struct Sci* **1986**, *42* (1), 51–55. https://doi.org/10.1107/S0108768186098592.

(21) Delahaye-Vidal, A.; Figlarz, M. Textural and Structural Studies on Nickel Hydroxide Electrodes. II. Turbostratic Nickel (II) Hydroxide Submitted to Electrochemical Redox Cycling. *J Appl Electrochem* **1987**, *17* (3), 589–599. https://doi.org/10.1007/BF01084134.

(22) Tessier, C.; Haumesser, P. H.; Bernard, P.; Delmas, C. The Structure of Ni (OH) 2: From the Ideal Material to the Electrochemically Active One. *J. Electrochem. Soc.* **1999**, *146* (6), 2059–2067. https://doi.org/10.1149/1.1391892.

(23) Tong, G.-X.; Liu, F.-T.; Wu, W.-H.; Shen, J.-P.; Hu, X.; Liang, Y. Polymorphous α- and β-Ni(OH)2 Complex Architectures: Morphological and Phasal Evolution Mechanisms and Enhanced Catalytic Activity as Non-Enzymatic Glucose Sensors. *CrystEngComm* **2012**, *14* (18), 5963. https://doi.org/10.1039/c2ce25622c.

(24) McEwen, R. S. Crystallographic Studies on Nickel Hydroxide and the Higher Nickel Oxides. *The Journal of Physical Chemistry* **1971**, *75* (12), 1782–1789. https://doi.org/10.1021/j100681a004.

(25) Burke, M. S.; Enman, L. J.; Batchellor, A. S.; Zou, S.; Boettcher, S. W. Oxygen Evolution Reaction Electrocatalysis on Transition Metal Oxides and (Oxy)Hydroxides: Activity Trends and Design Principles. *Chemistry of Materials* **2015**, *27* (22), 7549–7558. https://doi.org/10.1021/acs.chemmater.5b03148.

(26) Yu, J.; Pan, S.; Zhang, Y.; Liu, Q.; Li, B. Facile Synthesis of Monodispersed α-Ni(OH)2 Microspheres Assembled by Ultrathin Nanosheets and Its Performance for Oxygen Evolution Reduction. *Front. Mater.* **2019**, *6*. https://doi.org/10.3389/fmats.2019.00124.

(27) McBreen, J. Nikel Hydroxides. In *Handbook of Battery Materials*; Claus, D., Besenhard, J. O., Eds.; VCH: Weinheim ; New York, 1996; Vol. 1, pp 149–165.

(28) Batchellor, A. S.; Boettcher, S. W. Pulse-Electrodeposited Ni–Fe (Oxy)Hydroxide Oxygen Evolution Electrocatalysts with High Geometric and Intrinsic Activities at Large Mass Loadings. *ACS Catalysis* **2015**, *5* (11), 6680–6689. https://doi.org/10.1021/acscatal.5b01551.

(29) Cheek, G. T.; O'Grady, W. E. Redox Behavior of the Nickel Oxide Electrode System: Quartz Crystal Microbalance Studies. *Journal of Electroanalytical Chemistry* **1997**, *421* (1), 173–177. https://doi.org/10.1016/S0022-0728(96)04821-8.

(30) Dionigi, F.; Strasser, P. NiFe-Based (Oxy)Hydroxide Catalysts for Oxygen Evolution Reaction in Non-Acidic Electrolytes. *Advanced Energy Materials* **2016**, *6* (23), 1600621. https://doi.org/10.1002/aenm.201600621.

(31) Hunter, B. M.; Winkler, J. R.; Gray, H. B. Iron Is the Active Site in Nickel/Iron Water Oxidation Electrocatalysts. *Molecules* **2018**, *23* (4). https://doi.org/10.3390/molecules23040903.

(32) Wu, Y.; Zhao, M.-J.; Li, F.; Xie, J.; Li, Y.; He, J.-B. Trace Fe Incorporation into Ni-(Oxy)Hydroxide Stabilizes Ni^{3+} Sites for Anodic Oxygen Evolution: A Double Thin-Layer Study. *Langmuir* **2020**, *36* (19), 5126–5133. https://doi.org/10.1021/acs.langmuir.0c00264.

(33) Chung, D. Y.; Lopes, P. P.; Farinazzo Bergamo Dias Martins, P.; He, H.; Kawaguchi, T.; Zapol, P.; You, H.; Tripkovic, D.; Strmcnik, D.; Zhu, Y.; Seifert, S.; Lee, S.; Stamenkovic, V. R.; Markovic, N. M. Dynamic Stability of Active Sites in Hydr(Oxy)Oxides for the Oxygen Evolution Reaction. *Nature Energy* **2020**, *5* (3), 222–230. https://doi.org/10.1038/s41560-020-0576-y.

(34) Zhang, T.; Nellist, M. R.; Enman, L. J.; Xiang, J.; Boettcher, S. W. Modes of Fe Incorporation in Co–Fe (Oxy)Hydroxide Oxygen Evolution Electrocatalysts. *ChemSusChem* **2019**, *12* (9), 2015–2021. https://doi.org/10.1002/cssc.201801975.

(35) Stevens, M. B.; Trang, C. D. M.; Enman, L. J.; Deng, J.; Boettcher, S. W. Reactive Fe-Sites in Ni/Fe (Oxy)Hydroxide Are Responsible for Exceptional Oxygen Electrocatalysis Activity. *Journal of the American Chemical Society* **2017**, *139* (33), 11361–11364. https://doi.org/10.1021/jacs.7b07117.

(36) Goldsmith, Z. K.; Harshan, A. K.; Gerken, J. B.; Vörös, M.; Galli, G.; Stahl, S. S.; Hammes-Schiffer, S. Characterization of NiFe Oxyhydroxide Electrocatalysts by Integrated Electronic Structure Calculations and Spectroelectrochemistry. *PNAS* **2017**, *114* (12), 3050–3055. https://doi.org/10.1073/pnas.1702081114.

(37) Trotochaud, L.; Young, S. L.; Ranney, J. K.; Boettcher, S. W. Nickel–Iron Oxyhydroxide Oxygen-Evolution Electrocatalysts: The Role of Intentional and Incidental Iron Incorporation. *Journal of the American Chemical Society* **2014**, *136* (18), 6744–6753. https://doi.org/10.1021/ja502379c.

(38) Gamsjäger, H.; Bugajski, J.; Gajda, T.; Lemire, R.; Preis, W. *Chemical Thermodynamics of Nickel*; Mompean, F., Illemassène, M., Perrone, J., Eds.; Elsevier Science, 2005.

(39) Hall, D. S.; Lockwood, D. J.; Bock, C.; MacDougall, B. R. Nickel Hydroxides and Related Materials: A Review of Their Structures, Synthesis and Properties. *Proceedings of the Royal Society A: Mathematical, Physical and Engineering Sciences* **2015**, *471* (2174), 20140792. https://doi.org/10.1098/rspa.2014.0792.

(40) Gamsjäger, H.; Wallner, H.; Preis, W. Solid-Solute Phase Equilibria in Aqueous Solutions XVII [1]. Solubility and Thermodynamic Data of Nickel(II) Hydroxide. *Monatshefte für Chemie* **2002**, *133*, 225–229.

(41) Baldan, A. Review Progress in Ostwald Ripening Theories and Their Applications to Nickel-Base Superalloys. *J. Mat. Sci.* **2002**, *37*, 2171–2202.

(42) Park, S.; Song, Y. J.; Han, J.-H.; Boo, H.; Chung, T. D. Structural and Electrochemical Features of 3D Nanoporous Platinum Electrodes. *Electrochimica Acta* **2010**, *55* (6), 2029–2035. https://doi.org/10.1016/j.electacta.2009.11.026.

(43) Qu, D. Fundamental Principals of Battery Design: Porous Electrodes; Freiberg, Germany, 2014; pp 14–25. https://doi.org/10.1063/1.4878477.

(44) Liu, Z.; Yuan, X.; Zhang, S.; Wang, J.; Huang, Q.; Yu, N.; Zhu, Y.; Fu, L.; Wang, F.; Chen, Y.; Wu, Y. Three-Dimensional Ordered Porous Electrode Materials for Electrochemical Energy Storage. *NPG Asia Materials* **2019**, *11* (1), 1–21. https://doi.org/10.1038/s41427-019-0112-3.

(45) Klaus, S.; Cai, Y.; Louie, M. W.; Trotochaud, L.; Bell, A. T. Effects of Fe Electrolyte Impurities on Ni(OH) $_2$ /NiOOH Structure and Oxygen Evolution Activity. *The Journal of Physical Chemistry C* **2015**, *119* (13), 7243–7254. https://doi.org/10.1021/acs.jpcc.5b00105.

(46) Lifshitz, I. M.; Slyozov, V. V. The Kinetics of Precipitation from Supersaturated Solid Solutions. *Journal of Physics and Chemistry of Solids* **1961**, *19* (1), 35–50. https://doi.org/10.1016/0022-3697(61)90054-3.

(47) Bruce, P. G.; Scrosati, B.; Tarascon, J.-M. Nanomaterials for Rechargeable Lithium Batteries. *Angewandte Chemie International Edition* **2008**, *47* (16), 2930–2946. https://doi.org/10.1002/anie.200702505.

(48) Fominykh, K.; Feckl, J. M.; Sicklinger, J.; Döblinger, M.; Böcklein, S.; Ziegler, J.; Peter, L.; Rathousky, J.; Scheidt, E.-W.; Bein, T.; Fattakhova-Rohlfing, D. Ultrasmall Dispersible Crystalline Nickel Oxide Nanoparticles as High-Performance Catalysts for Electrochemical Water Splitting. *Advanced Functional Materials* **2014**, *24* (21), 3123–3129. https://doi.org/10.1002/adfm.201303600.

(49) Gong, M.; Li, Y.; Wang, H.; Liang, Y.; Wu, J. Z.; Zhou, J.; Wang, J.; Regier, T.; Wei, F.; Dai, H. An Advanced Ni–Fe Layered Double Hydroxide Electrocatalyst for Water Oxidation. *J. Am. Chem. Soc.* **2013**, *135* (23), 8452–8455. https://doi.org/10.1021/ja4027715.

(50) Lu, Z.; Qian, L.; Tian, Y.; Li, Y.; Sun, X.; Duan, X. Ternary NiFeMn Layered Double Hydroxides as Highly-Efficient Oxygen Evolution Catalysts. *Chem. Commun.* **2016**, *52* (5), 908–911. https://doi.org/10.1039/C5CC08845C.

(51) Liu, Z.; Li, N.; Zhao, H.; Zhang, Y.; Huang, Y.; Yin, Z.; Du, Y. Regulating the Active Species of Ni(OH)2 Using CeO2: 3D CeO2/Ni(OH)2/Carbon Foam as an Efficient Electrode for the Oxygen Evolution Reaction. *Chem. Sci.* **2017**, *8* (4), 3211–3217. https://doi.org/10.1039/C6SC05408K.

(52) Tian, P.; Yu, Y.; Yin, X.; Wang, X. A Wafer-Scale 1 Nm Ni(OH)2 Nanosheet with Superior Electrocatalytic Activity for the Oxygen Evolution Reaction. *Nanoscale* **2018**, *10* (11), 5054–5059. https://doi.org/10.1039/C7NR09042K.

(53) Fominykh, K.; Tok, G. C.; Zeller, P.; Hajiyani, H.; Miller, T.; Döblinger, M.; Pentcheva, R.; Bein, T.; Fattakhova-Rohlfing, D. Rock Salt Ni/Co Oxides with Unusual Nanoscale-Stabilized Composition as Water Splitting Electrocatalysts. *Advanced Functional Materials* **2017**, *27* (8), 1605121. https://doi.org/10.1002/adfm.201605121.

(54) Malara, F.; Carallo, S.; Rotunno, E.; Lazzarini, L.; Piperopoulos, E.; Milone, C.; Naldoni, A. A Flexible Electrode Based on Al-Doped Nickel Hydroxide Wrapped around a Carbon Nanotube Forest for Efficient Oxygen Evolution. *ACS Catal.* **2017**, *7* (7), 4786–4795. https://doi.org/10.1021/acscatal.7b01188.

(55) Ng, J. W. D.; García-Melchor, M.; Bajdich, M.; Chakthranont, P.; Kirk, C.; Vojvodic, A.; Jaramillo, T. F. Gold-Supported Cerium-Doped NiO x Catalysts for Water Oxidation. *Nature Energy* **2016**, *1* (5), 1–8. https://doi.org/10.1038/nenergy.2016.53.

(56) Friebel, D.; Louie, M. W.; Bajdich, M.; Sanwald, K. E.; Cai, Y.; Wise, A. M.; Cheng, M.-J.; Sokaras, D.; Weng, T.-C.; Alonso-Mori, R.; Davis, R. C.; Bargar, J. R.; Nørskov, J. K.; Nilsson, A.; Bell, A. T. Identification of Highly Active Fe Sites in (Ni,Fe)OOH for Electrocatalytic Water Splitting. *J. Am. Chem. Soc.* **2015**, *137* (3), 1305–1313. https://doi.org/10.1021/ja511559d.

(57) Li, N.; Bediako, D. K.; Hadt, R. G.; Hayes, D.; Kempa, T. J.; Cube, F. von; Bell, D. C.; Chen, L. X.; Nocera, D. G. Influence of Iron Doping on Tetravalent Nickel Content in Catalytic Oxygen Evolving Films. *PNAS* **2017**, *114* (7), 1486–1491. https://doi.org/10.1073/pnas.1620787114.

(58) Görlin, M.; Chernev, P.; Ferreira de Araújo, J.; Reier, T.; Dresp, S.; Paul, B.; Krähnert, R.; Dau, H.; Strasser, P. Oxygen Evolution Reaction Dynamics, Faradaic Charge Efficiency, and the Active Metal Redox States of Ni–Fe Oxide Water Splitting Electrocatalysts. *J. Am. Chem. Soc.* **2016**, *138* (17), 5603–5614. https://doi.org/10.1021/jacs.6b00332.

(59) Görlin, M.; Ferreira de Araújo, J.; Schmies, H.; Bernsmeier, D.; Dresp, S.; Gliech, M.; Jusys, Z.; Chernev, P.; Kraehnert, R.; Dau, H.; Strasser, P. Tracking Catalyst Redox States and Reaction Dynamics in Ni–Fe Oxyhydroxide Oxygen Evolution Reaction Electrocatalysts: The Role of Catalyst Support and Electrolyte PH. *J. Am. Chem. Soc.* **2017**, *139* (5), 2070–2082. https://doi.org/10.1021/jacs.6b12250.

(60) Chen, J. Y. C.; Dang, L.; Liang, H.; Bi, W.; Gerken, J. B.; Jin, S.; Alp, E. E.; Stahl, S. S. Operando Analysis of NiFe and Fe Oxyhydroxide Electrocatalysts for Water Oxidation: Detection of Fe4+ by Mössbauer Spectroscopy. *J. Am. Chem. Soc.* **2015**, *137* (48), 15090–15093. https://doi.org/10.1021/jacs.5b10699.

(61) Hunter, B. M.; Thompson, N. B.; Müller, A. M.; Rossman, G. R.; Hill, M. G.; Winkler, J. R.; Gray, H. B. Trapping an Iron(VI) Water-Splitting Intermediate in Nonaqueous Media. *Joule* **2018**, *2* (4), 747–763. https://doi.org/10.1016/j.joule.2018.01.008.

(62) Enman, L. J.; Stevens, M. B.; Dahan, M. H.; Nellist, M. R.; Toroker, M. C.; Boettcher, S. W. Operando X-Ray Absorption Spectroscopy Shows Iron Oxidation Is Concurrent with Oxygen Evolution in Cobalt–Iron (Oxy)Hydroxide Electrocatalysts. *Angewandte Chemie International Edition* **2018**, *57* (39), 12840–12844. https://doi.org/10.1002/anie.201808818.

(63) Farhat, R.; Dhainy, J.; Halaoui, L. I. OER Catalysis at Activated and Codeposited NiFe-Oxo/Hydroxide Thin Films Is Due to Postdeposition Surface-Fe and Is Not Sustainable without Fe in Solution. *ACS Catal.* **2020**, *10* (1), 20–35. https://doi.org/10.1021/acscatal.9b02580.

(64) Frydendal, R.; Paoli, E. A.; Knudsen, B. P.; Wickman, B.; Malacrida, P.; Stephens, I. E. L.; Chorkendorff, I. Benchmarking the Stability of Oxygen Evolution Reaction Catalysts: The Importance of Monitoring Mass Losses. *ChemElectroChem* **2014**, *1* (12), 2075–2081. https://doi.org/10.1002/celc.201402262.

(65) Barwick, V. J.; Ellison, S. L. R.; Fairman, B. Estimation of Uncertainties in ICP-MS Analysis: A Practical Methodology. *Analytica Chimica Acta* **1999**, *394* (2–3), 281–291. https://doi.org/10.1016/S0003-2670(99)00302-5.

(66) Tanase, I. Gh.; Popa, D. E.; Udriştioiu, G. E.; Bunaciu, A. A.; Aboul-Enein, H. Y. Estimation of the Uncertainty of the Measurement Results of Some Trace Levels Elements in Document Paper Samples Using ICP-MS. *RSC Adv.* **2015**, *5* (15), 11445–11457. https://doi.org/10.1039/C4RA12645A.

(67) Deng, J.; Nellist, M. R.; Stevens, M. B.; Dette, C.; Wang, Y.; Boettcher, S. W. Morphology Dynamics of Single-Layered Ni(OH) $_2$ /NiOOH Nanosheets and Subsequent Fe Incorporation Studied by *in Situ* Electrochemical Atomic Force Microscopy. *Nano Letters* **2017**, *17* (11), 6922–6926. https://doi.org/10.1021/acs.nanolett.7b03313.

(68) Louie, M. W.; Bell, A. T. An Investigation of Thin-Film Ni–Fe Oxide Catalysts for the Electrochemical Evolution of Oxygen. *Journal of the American Chemical Society* **2013**, *135* (33), 12329–12337. https://doi.org/10.1021/ja405351s.

(69) Mittemeijer, E. J. *Fundamentals of Materials Science: The Microstructure–Property Relationship Using Metals as Model Systems*; Springer Science & Business Media, 2010.

(70) Corrigan, D. A.; Knight, S. L. Electrochemical and Spectroscopic Evidence on the Participation of Quadrivalent Nickel in the Nickel Hydroxide Redox Reaction. *J. Electrochem. Soc.* **1989**, *136* (3), 613–619. https://doi.org/10.1149/1.2096697.

(71) Stevens, M. B.; Enman, L. J.; Batchellor, A. S.; Cosby, M. R.; Vise, A. E.; Trang, C. D. M.; Boettcher, S. W. Measurement Techniques for the Study of Thin Film Heterogeneous Water Oxidation Electrocatalysts. *Chem. Mater.* **2017**, *29* (1), 120–140. https://doi.org/10.1021/acs.chemmater.6b02796.

(72) Plyasunova, N. V.; Zhang, Y.; Muhammed, M. Critical Evaluation of Thermodynamics of Complex Formation of Metal Ions in Aqueous Solutions. IV. Hydrolysis and Hydroxo-Complexes of Ni2+ at 298.15 K. *Hydrometallurgy* **1998**, *48* (1), 43–63. https://doi.org/10.1016/S0304-386X(97)00070-4.

(73) Martirez, J. M. P.; Carter, E. A. Effects of the Aqueous Environment on the Stability and Chemistry of β-NiOOH Surfaces. *Chem. Mater.* **2018**, *30* (15), 5205–5219. https://doi.org/10.1021/acs.chemmater.8b01866.

(74) Serpone, N.; Pelizzetti, E. *Photocatalysis: Fundamentals and Applications*; Wiley: New York, 1989.

(75) Osterloh, F. E. Inorganic Materials as Catalysts for Photochemical Splitting of Water. *Chem. Mater.* **2008**, *20* (1), 35–54. https://doi.org/10.1021/cm7024203.

(76) Mao, S. S.; Shen, S. Hydrogen Production: Catalysing Artificial Photosynthesis. *Nature Photonics* **2013**, *7* (12), 944–946. https://doi.org/10.1038/nphoton.2013.326.

(77) Sun, K.; Shen, S.; Liang, Y.; Burrows, P. E.; Mao, S. S.; Wang, D. Enabling Silicon for Solar-Fuel Production. *Chem. Rev.* **2014**, *114* (17), 8662–8719. https://doi.org/10.1021/cr300459q.

(78) Schweitzer, G. K.; Pesterfield, L. L. *The Aqueous Chemistry of the Elements*; Oxford University Press: New York, 2010.

(79) Hu, S.; Lewis, N. S.; Ager, J. W.; Yang, J.; McKone, J. R.; Strandwitz, N. C. Thin-Film Materials for the Protection of Semiconducting Photoelectrodes in Solar-Fuel Generators https://pubs.acs.org/doi/full/10.1021/acs.jpcc.5b05976 (accessed Aug 10, 2018). https://doi.org/10.1021/acs.jpcc.5b05976.

(80) Bae, D.; Seger, B.; Vesborg, P. C. K.; Hansen, O.; Chorkendorff, I. Strategies for Stable Water Splitting via Protected Photoelectrodes. *Chem. Soc. Rev.* **2017**, *46* (7), 1933–1954. https://doi.org/10.1039/C6CS00918B.

(81) Hu, S.; Shaner, M. R.; Beardslee, J. A.; Lichterman, M.; Brunschwig, B. S.; Lewis, N. S. Amorphous TiO2 Coatings Stabilize Si, GaAs, and GaP Photoanodes for Efficient Water Oxidation. *Science* **2014**, *344* (6187), 1005–1009. https://doi.org/10.1126/science.1251428.

(82) Scheuermann, A. G.; Lawrence, J. P.; Kemp, K. W.; Ito, T.; Walsh, A.; Chidsey, C. E. D.; Hurley, P. K.; McIntyre, P. C. Design Principles for Maximizing Photovoltage in Metal-Oxide-Protected Water-Splitting Photoanodes. *Nature Materials* **2016**, *15* (1), 99–105. https://doi.org/10.1038/nmat4451.

(83) Hezel, R. Recent Progress in MIS Solar Cells. *Progress in Photovoltaics: Research and Applications* **1997**, *5* (2), 109–120. https://doi.org/10.1002/(SICI)1099-159X(199703/04)5:2<109::AID-PIP160>3.0.CO;2-8.

(84) Hoex, B.; Heil, S. B. S.; Langereis, E.; van de Sanden, M. C. M.; Kessels, W. M. M. Ultralow Surface Recombination of C-Si Substrates Passivated by Plasma-Assisted Atomic Layer Deposited Al2O3. *Appl. Phys. Lett.* **2006**, *89* (4), 042112. https://doi.org/10.1063/1.2240736.

(85) Agostinelli, G.; Delabie, A.; Vitanov, P.; Alexieva, Z.; Dekkers, H. F. W.; De Wolf, S.; Beaucarne, G. Very Low Surface Recombination Velocities on P-Type Silicon Wafers Passivated with a Dielectric with Fixed Negative Charge. *Solar Energy Materials and Solar Cells* **2006**, *90* (18), 3438–3443. https://doi.org/10.1016/j.solmat.2006.04.014.

(86) Hoex, B.; Schmidt, J.; Pohl, P.; van de Sanden, M. C. M.; Kessels, W. M. M. Silicon Surface Passivation by Atomic Layer Deposited Al2O3. *Journal of Applied Physics* **2008**, *104* (4), 044903. https://doi.org/10.1063/1.2963707.

(87) Groner, M. D.; Fabreguette, F. H.; Elam, J. W.; George, S. M. Low-Temperature Al2O3 Atomic Layer Deposition. *Chem. Mater.* **2004**, *16* (4), 639–645. https://doi.org/10.1021/cm0304546.

(88) Mack, C. *Fundamental Principles of Optical Lithography: The Science of Microfabrication*; John Wiley & Sons, Incorporated: Newy York, UNITED KINGDOM, 2007.

(89) Sze, S. M. *Semiconductor Devices: Physics and Technology*, Second.; John Wiley & Sons, Inc.: Danvers, MA, 2002.

(90) Pampillón Arce, M. Á. Fabrication Techniques. In *Growth of High Permittivity Dielectrics by High Pressure Sputtering from Metallic Targets*; Pampillón Arce, M. Á., Ed.; Springer Theses; Springer International Publishing: Cham, 2017; pp 21–39. https://doi.org/10.1007/978-3-319-66607-5_2.

(91) Kohl, P. A.; Frank, S. N.; Bard, A. J. Semiconductor Electrodes XI . Behavior of N- and P-Type Single Crystal Semconductors Covered with Thin Films. *J. Electrochem. Soc.* **1977**, *124* (2), 225–229. https://doi.org/10.1149/1.2133270.

(92) Scheuermann, A. G.; McIntyre, P. C. Atomic Layer Deposited Corrosion Protection: A Path to Stable and Efficient Photoelectrochemical Cells. *J. Phys. Chem. Lett.* **2016**, *7* (14), 2867–2878. https://doi.org/10.1021/acs.jpclett.6b00631.

(93) Hu, S.; Richter, M. H.; Lichterman, M. F.; Beardslee, J.; Mayer, T.; Brunschwig, B. S.; Lewis, N. S. Electrical, Photoelectrochemical, and Photoelectron Spectroscopic Investigation of the Interfacial Transport and Energetics of Amorphous TiO2/Si Heterojunctions. *J. Phys. Chem. C* **2016**, *120* (6), 3117–3129. https://doi.org/10.1021/acs.jpcc.5b09121.

(94) Daubert, J. S.; Hill, G. T.; Gotsch, H. N.; Gremaud, A. P.; Ovental, J. S.; Williams, P. S.; Oldham, C. J.; Parsons, G. N. Corrosion Protection of Copper Using Al_2O_3, TiO_2, ZnO, HfO_2, and ZrO_2 Atomic Layer Deposition. *ACS Applied Materials & Interfaces* **2017**, *9* (4), 4192–4201. https://doi.org/10.1021/acsami.6b13571.

(95) Xing, Z.; Ren, F.; Wu, H.; Wu, L.; Wang, X.; Wang, J.; Wan, D.; Zhang, G.; Jiang, C. Enhanced PEC Performance of Nanoporous Si Photoelectrodes by Covering HfO_2 and TiO_2 Passivation Layers. *Scientific Reports* **2017**, *7*, 43901. https://doi.org/10.1038/srep43901.

(96) Cui, J.; Wan, Y.; Cui, Y.; Chen, Y.; Verlinden, P.; Cuevas, A. Highly Effective Electronic Passivation of Silicon Surfaces by Atomic Layer Deposited Hafnium Oxide. *Applied Physics Letters* **2017**, *110* (2), 021602. https://doi.org/10.1063/1.4973988.

(97) Al-Kuhaili, M. F. Optical Properties of Hafnium Oxide Thin Films and Their Application in Energy-Efficient Windows. *Optical Materials* **2004**, *27* (3), 383–387. https://doi.org/10.1016/j.optmat.2004.04.014.

(98) Oh, J.; Myoung, J.; Bae, J. S.; Lim, S. Etch Behavior of ALD Al2O3 on HfSiO and HfSiON Stacks in Acidic and Basic Etchants. *J. Electrochem. Soc.* **2011**, *158* (4), D217–D222. https://doi.org/10.1149/1.3554729.

(99) Niinistö, L. Atomic Layer Epitaxy. *Current Opinion in Solid State and Materials Science* **1998**, *3* (2), 147–152. https://doi.org/10.1016/S1359-0286(98)80080-6.

(100) Ritala, M.; Leskelä, M. Atomic Layer Epitaxy - a Valuable Tool for Nanotechnology? *Nanotechnology* **1999**, *10* (1), 19–24. https://doi.org/10.1088/0957-4484/10/1/005.

(101) Lowalekar, V.; Raghavan, S. Etching of Zirconium Oxide, Hafnium Oxide, and Hafnium Silicates in Dilute Hydrofluoric Acid Solutions. *Journal of Materials Research* **2004**, *19* (04), 1149–1156. https://doi.org/10.1557/JMR.2004.0149.

(102) Liu, T.; Yang, K.; Zhang, Z.; Yan, L.; Huang, B.; Li, H.; Zhang, C.; Jiang, X.; Yan, H. Hydrofluoric Acid–Based Etching Effect on Surface Pit, Crack, and Scratch and Laser Damage Site of Fused Silica Optics. *Opt. Express, OE* **2019**, *27* (8), 10705–10728. https://doi.org/10.1364/OE.27.010705.

(103) Laskowski, F. A. L.; Nellist, M. R.; Qiu, J.; Boettcher, S. W. Metal Oxide/(Oxy)Hydroxide Overlayers as Hole Collectors and Oxygen-Evolution Catalysts on Water-Splitting Photoanodes. *J. Am. Chem. Soc.* **2019**, *141* (4), 1394–1405. https://doi.org/10.1021/jacs.8b09449.

(104) Laskowski, F. A. L.; Oener, S. Z.; Nellist, M. R.; Gordon, A. M.; Bain, D. C.; Fehrs, J. L.; Boettcher, S. W. Nanoscale Semiconductor/Catalyst Interfaces in Photoelectrochemistry. *Nature Materials* **2020**, *19* (1), 69–76. https://doi.org/10.1038/s41563-019-0488-z.

(105) Tung, R. T. (董梓則). The Physics and Chemistry of the Schottky Barrier Height. *Applied Physics Reviews* **2014**, *1* (1), 011304. https://doi.org/10.1063/1.4858400.

(106) Wilschefski, S. C.; Baxter, M. R. Inductively Coupled Plasma Mass Spectrometry: Introduction to Analytical Aspects. *Clin Biochem Rev* **2019**, *40* (3), 115–133. https://doi.org/10.33176/AACB-19-00024.